Robust Position Sensorless Model Predictive Control for Interior Permanent Magnet Synchronous Motor Drives

ROBUST POSITION SENSORLESS MODEL PREDICTIVE CONTROL FOR INTERIOR PERMANENT MAGNET SYNCHRONOUS MOTOR DRIVES

BY

SHAMSUDDEEN NALAKATH, M.S.

A THESIS

SUBMITTED TO THE DEPARTMENT OF ELECTRICAL & COMPUTER ENGINEERING

AND THE SCHOOL OF GRADUATE STUDIES

OF MCMASTER UNIVERSITY IN PARTIAL FULFILMENT OF THE REQUIREMENTS

FOR THE DEGREE OF

DOCTOR OF PHILOSOPHY

McMaster University

Doctor of Philosophy (2018) McMaster University

(Electrical & Computer Engineering) Hamilton, Ontario, Canada

TITLE:	Robust Position Sensorless Model Predictive Control for Interior Permanent Magnet Synchronous Motor Drives
AUTHOR:	Shamsuddeen Nalakath M.S, (Electrical Engineering) Indian Institute of Technology Madras, Chennai, India
SUPERVISOR:	Dr. Ali Emadi Ph.D. (Texas A&M University) IEEE Fellow Canada Excellence Research Chair in Hybrid Powertrain
NUMBER OF PAGES:	xx, 150

To My Family

Abstract

This thesis focuses on utilizing the persistent voltage vector injections by finite control set model predictive control (FCSMPC) to enable simultaneous estimations of both position and parameters in order to realize robust sensorless interior permanent magnet synchronous machine (IPMSM) drives valid at the entire operating region including no-load standstill without any additional signal injection and switchover.

The system (here, IPMSM) needs to meet certain observability conditions to identify the parameters and position. Moreover, each combination of the parameters and/or position involves different observability requirements which cannot be accomplished at every operating point. In particular, meeting the observability for parameters and position at no-load standstill is more challenging. This is overcome by generating persistent excitation in the system with high-frequency signal injection. The FCSMPC scheme inherently features the persistent excitation with voltage vector injection and hence no additional signal injection is required. Moreover, the persistent excitation always exists for FCSMPC except at the standstill where the control applies the null vectors when the reference currents are zero. However, introducing a small negative d axis current at the standstill would be sufficient to overcome this situation.

The parameter estimations are investigated at first in this thesis. The observability

is analyzed for the combinations of two, three and four parameters and experimentally validated by online identification based on recursive least square (RLS) based adaptive observer. The worst case operating points concerning observability are identified and experimentally proved that the online identification of all the parameter combinations could be accomplished with persistent excitation by FCMPC. Moreover, the effect of estimation error in one parameter on the other known as parameter coupling is reduced with the proposed decoupling technique.

The persistent voltage vector injections by FCSMPC help to meet the observability conditions for estimating the position, especially at low speeds. However, the arbitrary nature of the switching ripples and absence of PWM modulator void the possibility of applying the standard demodulation based techniques for FCSMPC. Consequently, a nonlinear optimization based observer is proposed to estimate both the position and speed, and experimentally validated from standstill to maximum speed. Furthermore, a compensator is also proposed that prevents converging to saddle and symmetrical (π ambiguity) solutions.

The robustness analysis of the proposed nonlinear optimization based observer shows that estimating the position without co-estimating the speed is more robust and the main influencing parameters on the accuracy of the position estimation are d and q inductances. Subsequently, the proposed nonlinear optimization based observer is extended to simultaneously estimate the position, d and q inductances. The experimental results show the substantial improvements in response time, and reduction in both steady and transient state position errors.

In summary, this thesis presents the significance of persistent voltage vector injections in estimating both parameter and position, and also shows that nonlinear optimization based technique is an ideal candidate for robust sensorless FCSMPC.

Acknowledgements

First and foremost, I would like to express my sincerest gratitude to my supervisor, Dr. Ali Emadi, for offering me an opportunity to be a part of world's leading academic research programs in transportation electrification, and for providing me tremendous insights, guidance, motivation, and support. His most exceptional dedication, enthusiasm, and vision inspired me throughout my Ph.D. study and will inspire me for the rest of my life.

I would also like to thank Dr. Matthias Preindl for his co-supervision in conceptualizing my Ph.D. thesis and also helping me in tackling the technical challenges. His engineering judgments and mathematical proficiency set a benchmark for me to accomplish in my research career.

I would also like to thank my supervisory committee members Dr. Nigel Schoffield and Dr. Babak Nahidmobarakeh for their insightful comments and stimulating discussions throughout the program. I was fortunate to attend Dr. Schoffield's course on electrical machines that helped me in gaining strong fundamentals. My gratitude to Dr. Nahidmobarkeh for his guidance and inputs in two of the publications related to my Ph.D. thesis.

This research was undertaken, in part, thanks to funding from the Canada Excellence Research Chairs Program.

I would like to thank my Master's supervisors Dr. Krishna Vasudevan and Dr. V. Jayashankar for introducing me to research and encouraging me to pursue research as a career.

I would also like to extend my gratitude to VP advanced engineering group, Dr. Samraj Jabez Dhinagar, for providing me an opportunity to be the part of many cutting edge projects in traction machines that helped me in many ways at the course of my Ph.D.. I would also like to thank my former manager at TVS Motor Company Dr. Sreeju S Nair for being a friend and a mentor.

I am also grateful to my lab colleagues, Yingguang Sun, Yu Miao, Le Sun, Hao Ge, Alan Callegaro, Deqian Wang, Ben Danen, and Michael Kasprazak for their help and support. Special thanks to Ben Danen for proofreading two of the publications related to this thesis, and also to Teresa Janes, Theresa Mitchell and Dan Manolescu, in organizing and coordinating the research needs.

Words cannot express my gratitude and love to my parents for their endless support, sacrifice, and generous love. I also extend my thanks to my siblings and friends who are always there for me whenever I am in need.

I want to thank my wife Zahiya for her love, encouragement, and managing the family on my busy days, and also to my children Afraaz and Aroosh from whom I stole the time they most deserved to work on my Ph.D. thesis.

Above all, I thank the Almighty for the guidance, strength, and protection bestowed throughout my life.

Notation

Symbols

abc	stationary three phase reference frame
$\alpha\beta$	stationary two axis reference frame
dq	rotating two axis reference frame
$\delta\gamma$	estimated two axis rotating reference frame
v_a, v_b, v_c	three phase voltages
$\mathbf{v}_{abc}$	three phase voltage vector
i_a, i_b, i_c	three phase currents
$\mathbf{i}_{abc}$	three phase current vector
v_d, v_q	voltages in dq frame
$\mathbf{v}_{dq}$	voltage vector in dq frame
i_d, i_q	currents in dq frame
$\mathbf{i}_{dq}$	current vector in dq frame
v_δ, v_γ	voltages in $\delta\gamma$ frame
$\mathbf{v}_{\delta\gamma}$	voltage vector in $\delta\gamma$ frame
i_δ, i_γ	currents in $\delta\gamma$ frame
$\mathbf{i}_{\delta\gamma}$	current vector in $\delta\gamma$ frame

θ	measured (or actual) rotor position
$\hat{\theta}$	estimated rotor position
$\hat{\vartheta}$	estimated angle difference between dq and $\delta\gamma$ frames
ω	measured (or actual) rotor speed
$\hat{\omega}$	estimated rotor speed
$\hat{\vartheta}_o$	optimal solution of ϑ
L_d	d-axis inductance
L_q	q-axis inductance
R	phase winding resistance
ψ_m	PM flux linkage
$\hat{}$	indicates estimated variable

Abbreviations

AC	alternating current
DC	dc current
FCS	finite control set
FCSMPC	FCS model predictive control
IM	induction machine
IPMSM	interior permanent magnet synchronous machine
MPC	model predictive control
PM	permanent magnet
PE	persistent excitation
SPMSM	surface permanent magnet synchronous machine

Contents

List of Tables

List of Figures

Chapter 1

Introduction

1.1 Background

The electric motor-driven systems have been the workforce for any modern industry, and they account for about 54% of the total electricity consumption in the United States (DOE/GO-102014-4356, 2014). The traditional industrial motor drive systems are AC machines supplied with fixed frequency utility power and operate at constant speed. The variable speed drives have been evolved to utilize electric energy efficiently and to meet the dynamic load demands, however, restricted to DC machine drives at the beginning (around 1930s (Bose, 2009)). As the DC machines are expensive and less reliable as compared to AC machines, extensive research has been carried out in development of variable AC drives in last three decades. Moreover, the invention of power electronic converters greatly expedited the development of variable AC drive systems.

The v/f control is the most straightforward and widely used variable speed drive technique for industrial AC machines. However, it has a slow dynamic response, and

low steady state accuracy as the torque and flux are not independently controlled. The field-oriented control (FOC) which surpasses v/f control by independently controlling torque and flux became popular after the commercialization of digital signal processors in early 1980s (Gabriel *et al.*, 1980). Since then FOC has been the best control strategy for the high-performance variable speed AC machine drive systems. The dynamic performance of the FOC is mainly dependent on tuning the cascaded current and speed PI (proportional-integral) controllers. On other hand, the fast torque response is achieved in direct torque control (DTC) strategy which directly applies voltage vectors without any PI controller. However, DTC produces significant torque ripples as it utilizes finite voltage vectors.

The model predictive control (MPC) which was initially developed for process industries in the late 1970s is gaining more attention in power electronics and motor drive applications with the support of fast modern processors (Geyer, 2009; Lee, 2011; Camacho and Carlos, 2007). Unlike the cascaded control systems, many system variables are controlled within a single control loop, and the constraints are easily incorporated in MPC. The MPC with finite control set (FCSMPC) is often preferred over the continuous MPC as the latter requires more computational resources to solve the nonlinear optimization problem (Preindl *et al.*, 2013; Preindl and Bolognani, 2013a). In one of the popular implementation of FCSMPC, the currents are controlled in the rotational reference frame (dq) to perform field oriented control, in which the voltage vectors producing the minimum error between the reference and predicted currents are applied to electric machines (Wang *et al.*, 2017).

The machine parameters are assumed to be constants in modeling and development of the standard control schemes. However, these parameters vary significantly

especially for the high performance applications like automotive traction (Emadi, 2015). In the advanced control schemes, e.g. position sensorless and optimal controls, the actual parameters considering the variations are either updated from a lookup table or by estimation. To accomplish the estimation, the voltage input to the machines should achieve persistent excitation or in other words, meet the observability conditions. As the electric machines with parameter variations is inherently a nonlinear system, the classical linear observability theory cannot be applied (Li, 2005; Xu, 2004). The machine model is linearized in a particular state subspace to apply the linear observability theorem in (Basic *et al.*, 2010; Laroche *et al.*, 2008) however this approach is very localized and lacks the sense of observability in the entirety of the state trajectories. The analysis of global observability of the nonlinear dynamic system is complicated in practice (Guerra *et al.*, 2015). The local observability is a powerful concept, and the theory proposed by Hermann and Krener with the help of Lie-theoretic characterization is a widely accepted approach for nonlinear system observability (Hermann and Krener, 1977).

The nonlinear observability analysis for identification of the electric machine parameters in literature is also mainly based on the concept proposed by Hermann Krener (Zaltni D.a Abdelkrim *et al.*, 2009; Vaclavek *et al.*, 2013; Boileau *et al.*, 2011). The determination of observability conditions for identifying a single parameter is straightforward. At least an element in the column of Jacobian of the Lie-derivative vector corresponding to that individual parameter should be nonzero. On the other hand, the corresponding columns should be linearly independent for simultaneously identifying two or more parameters. Consequently, there are parameters which are identifiable individually cannot be identified simultaneously in a combination. It is

shown that the estimation of stator resistance and inductance for a surface permanent magnet synchronous machine (SPMSM) are always identifiable as long as speed and q-axis current are non zero in (Boileau *et al.*, 2011). The observability conditions for estimating speed, position and resistance for induction machine (IM) and interior permanent magnet synchronous machine (IPMSM) are presented in (Vaclavek *et al.*, 2013) and that for estimating position for SPMSM and IPMSM are analyzed in (Zaltni D.a Abdelkrim *et al.*, 2009). The available literature examines the observability of only a few parameter combinations and a detailed analysis covering all the possible combinations is still unexplored.

The steady state is the most challenging (worst case) operating condition regarding the machine parameter identification (Boileau *et al.*, 2011; Liu, 2015). Most of the parameter combinations fail to be identifiable at this scenario. It is overcome by injecting high frequency-signals to establish the persistent excitation. The full parameter estimation by injecting both sinusoidal and square wave signals at d axis are compared in (Liu, 2015) and shown that the sinusoidal injection results in faster convergence. The robustness of the estimation of all the parameters with signal injection is improved by decoupling the slow and fast parameters with two differently sampled recursive least square (RLS) estimators in (Underwood, 2010). The coupling between resistance and permanent magnet flux linkage is also briefly mentioned in (Underwood, 2010) without any direction for compensation. The slow parameters from a high-frequency model and the fast parameters by RLS are estimated in (Xu, 2014). A complete decoupling is achieved in this case by the fact that the two estimators are based on different models (high frequency and fundamental). In (Dang, 2016), two affine projection estimators are used for slow and fast parameters. The

full parameter estimation techniques are fairly established in literature. However, the details on high discretization error for slow parameter estimation at the low sampling rate and the parameter coupling are not well addressed.

The standstill and low-speed operation are the most challenging situation for estimation of position. The position is not observable in this condition unless there is a persistent excitation into the system (Vaclavek *et al.*, 2013). The persistent excitation is established by injecting high-frequency signals such as sinusoidal, square, arbitrary and pulse vector into the system. The responses of these injected signals are utilized in extracting the position information in the standard position estimation techniques. For instance, the demodulation based techniques are applied to periodic continuous injection like sinusoidal and square waves, and the current derivative model-based methods are employed for pulse vector injection (Gong and Zhu, 2012; Corley and Lorenz, 1998; Leidhold, 2011; Foo and Xinan, 2015). The techniques mentioned above cannot be directly applied for the sensorless FCSMPC as it does not have any modulator to superimpose the injected signal with the fundamental excitation. There is an attempt to estimate the position from the high-frequency reactive power with demodulation technique in (Nalakath *et al.*, 2016); however, the wide varying nature of the arbitrary injection frequency associated with FCSMPC causes difficulty in locking the filter and phase locked loop (PLL) parameters. The cost function of the FCSMPC is modified to superimpose the high-frequency sinusoidal signal along with the control vectors in (Muzikova *et al.*, 2015). However, differentiating the responses between the superimposed signal and the inherent high-frequency vector is challenging as this method relies on the standard demodulation.

The model-based methods are found to be discussed more in literature for the

position sensorless FCSMPC especially at standstill and low-speeds. A model based second order observer consisting of a PLL and a feed-forward loop is presented in (Preindl and Schaltz, 2011) and showed that the position could be estimated for a wide speed range except at speeds close to the standstill as there are oscillations in the estimation. The results of specially simplified model equations introduced to estimate the position for FCSMPC drives in (Rovere *et al.*, 2016) are promising except 12 electrical degree oscillations in the position estimation at nominal load. The reduced order extended Kalman filter presented in (Fuentes and Kennel, 2011) estimates the position at low and high speeds; however, the maximum position error is 22 electrical degree even at steady state. The extended mean admittance based sensorless scheme is presented in (Landsmann and Kennel, 2012) and this method shows about 10 electrical degree oscillations in position estimation at the standstill. Nonlinear optimization based method to estimate position and speed is presented in (Nalakath *et al.*, 2017). This technique has the error of 12 electrical degree at the rated load. The parameter dependency on position estimation is not compensated in these models based methods for FCSMPC, and perhaps that could be the source of the significant errors in position estimation.

The online parameter identification methods to improve the position estimation is mainly focused on the robust sensorless vector control for medium and high-speed operations. The affine projection algorithms are employed for online identification of stator resistance, and the observer based on electromotive force (emf) is corrected for the parameter to estimate the position of IPMSM drives in (Rafaq *et al.*, 2017). These two estimation algorithms are realized in fast and slow time intervals. There

are considerable improvements in steady-state performance of the position estimation, however, the transient position error is 0.2 rad that attributes to the relatively slow convergence of the parameter estimation. The identification of stator resistance and inductances based on recursive least square (RLS) is found in (Ichikawa *et al.*, 2006) and the estimated parameters are supplied to emf based position observer. The convergence of parameters with this method is slow due to the low pass filters, and the position error with load change is within 6 electrical degree. In (Morimoto *et al.*, 2006), the similar technique is applied to estimate the voltage error and q axis inductance to improve the emf based position observer and showed that the position error is within 6 electrical degree.

1.2 Motivation

The model predictive control with finite control set (FCSMPC) is an emerging control strategy for electric motor drives and power electronic converters due to its simple implementation, fast response, and capability to handle MIMO systems and constraints. This control scheme generates significant switching ripples as it applies finite voltage vectors to an electric machine. This thesis focuses on utilizing this switching ripples to overcome the observability issues in parameter, position and speed estimations. The observability has a direct relationship with persistent excitation (PE), and this thesis explores PE requirements to meet the observability. Moreover, not all the combinations of the parameters, position, and speed are simultaneously observable, and unfortunately, there is no detailed analysis found in the literature on this account. This thesis analyzes all the possible combinations and identifies non-observable combinations and experimentally shows that the FCSMPC can overcome these limitations

by its inherent voltage vector injection (PE).

The standard signal injection based position estimation techniques employed for low-speed sensorless operation cannot be applied to FCMPC as it does not have any modulator to superimpose the injected signal with fundamental excitation. For standard back emf (electromotive force) based high-speed sensorless techniques, the low pass filters are required to eliminate the switching ripples components associated with FCSMPC. However, it is challenging to tune the filter coefficients as the frequency of the switching ripples widely varies with the operating speed. There have been model based methods for FCSMPC reported in literature that estimate the position and speed from standstill to maximum speed of the machine. However, the performances are not up to the level to implement for high-performance sensorless applications. This thesis proposes a nonlinear optimization based method that realizes the fast and accurate position and speed estimations without any switchover and additional signal injection.

The online parameter identification techniques to improve the position estimation accuracy in the literature are focused on medium to high speed robust sensorless vector control. These model-based methods essentially switch to inherently parameter independent standard demodulation techniques at low speeds. If the model-based methods are employed at low speeds, the parameter variations significantly influence the accuracy of the position estimation similar to medium and high-speed operations. Moreover, the estimation at low speed is more sensitive to the inductance variations as the position information comes from the current derivative terms in the model. It raises severe concern in the case of robust position estimation for FCSMPC which has high current derivative terms due to the strong switching ripples. This thesis is

the first attempt for low-speed robust model-based position estimation and also for its application to FCSMPC. A single observer for parameter and position estimation based on nonlinear optimization is also a novel approach proposed in this thesis.

1.3 Contributions

The author has contributed a number of original developments in the areas of observability analysis and simultaneous estimation of position, speed and parameters to realize the robust position sensorless IPMSM drives with FCSMPC in this thesis, which are listed as follows:

1. The detailed nonlinear observability analysis for simultaneously identifying the different combinations of the machine parameters, position, and speed.

2. Experimental validations to prove that the voltage vector injection by FCSMPC can accomplish persistent excitation to overcome the non-observability issues.

3. Nonlinear optimization based position estimation method is proposed and experimentally validated at different dynamic and steady-state operating conditions to prove that it is an ideal candidate for FCSMPC which has the arbitrary signal injection.

4. The detailed convergence analysis for the proposed nonlinear optimization based position estimation method is presented.

5. A compensator which eliminates the convergences of the nonlinear optimization method to saddle and symmetrical solutions (π-ambiguity) at the standstill is proposed and experimentally validated.

6. The robustness analysis of the nonlinear optimization based position estimation method with respect to parameter variations is conducted and identified the most

influencing parameters.

7. The proposed nonlinear optimization based position estimation method is extended to co-estimate the parameters to realize the robust sensorless FCSMPC.

8. The proposed robust sensorless FCSMPC is validated experimentally at the different dynamic and steady state operating conditions.

1.4 Thesis Outline

This thesis focuses on investigating the significance of persistent voltage vector excitations towards the simultaneous estimation of machine parameters, position and speed for IPMSM drives, and also shows that nonlinear optimization based technique is an ideal candidate for robust sensorless FCSMPC.

Chapter 2 starts by introducing different components in a typical interior permanent magnet synchronous motor (IPMSM) drive system and follows with a brief review of the criteria for generating the references for the advanced control. The derivation of mathematical models of IPMSM in different rotating reference frames is presented. Finally, the parameter variations with respect to different operating conditions are discussed.

Chapter 3 introduce general model predictive control (MPC) scheme and describes the relevant constrained finite-horizon optimal control problem. The variants of MPC classified based on the different approaches to solve the optimal control problem are discussed. The literature review on the application of these variants on electric motor drive applications is also presented with the emphasize on their computational effectiveness.

In chapter 4, the notion of persistent excitation and its relationship with observability are discussed. The concept of local observability is explained in detail, and it is employed in this thesis as the standard observability techniques cannot be applied to IPMSM which is nonlinear. The persistent excitation requirements to enable the observability of the position, speed and the parameters for IPMSM are laid out. The response of the voltage vector injections associated with FCSMPC is analyzed in the context of persistent excitation requirements to achieve observability.

The proposed online estimation scheme to estimate the electrical machine parameters is prsented in chapter 5. The estimation is realized with the help of recursive least square (RLS) adaptation algorithm. The RLS formulations for different parameter combinations are presented. The parameter combinations which are not identifiable at steady state without persistent excitation are only considered for the experimentation. The experimental results show that all these parameter combinations are identifiable by online estimation as the voltage vector injection by FCSMPC establishes the persistent excitation. Moreover, the parameter coupling in estimation that results in wrong convergence is analyzed and proposed a decoupling technique.

Chapter 6 presents the online estimation of position and speed for the reference IPMSM with FCSMPC. The proposed online estimation scheme is based on nonlinear optimization as the standard position estimation techniques are not suitable for FCSMPC. A strong, persistent excitation is always present with FCSMPC and therefore the proposed method can estimate the position and speed over a full speed range starting from standstill to the rated speed without a changeover and additional signal injection. This paper also presents detailed convergence analysis and proposes a

compensator for standstill operation that prevents converging to saddle and symmetrical solutions. The performance of the proposed estimation scheme is experimentally verified for a wide range of operating conditions.

In chapter 7, a single nonlinear optimization based observer which simultaneously estimates both position, and d and q inductances at every sampling interval to realize the robust sensorless FCSMPC for the reference IPMSM is proposed. The voltage vector injections by FCSMPC establish persistent excitation and enables simultaneous identification at wide operating region however it limits employing the standard techniques for the position estimation. The proposed method is suitable for any signal injection and hence an ideal candidate for FCSMPC. This chapter also presents detailed robustness and convergence analyzes. Finally, the performance of the proposed robust sensorless control scheme is verified experimentally at different operating conditions.

The conclusion of this thesis is provided in Chapter 8 with suggested future work.

Chapter 2

Interior Permanent Magnet Synchronous Motor (IPMSM) Drives and Model

2.1 Introduction

This chapter starts by introducing different components in a typical interior permanent magnet synchronous motor (IPMSM) drive system and follows with a brief review of the criteria for generating the references for the advanced control. The derivation of mathematical models of IPMSM in different rotating reference frames is presented. Finally, the parameter variations with respect to different operating conditions are discussed.

2.2 IPMSM Drive System

An electric drive system converts electrical energy into mechanical or vice-versa. A typical modern interior permanent magnet (IPMSM) drive system consists of IPMSM, power converter, control system, and sensors as shown in Fig. 2.1. The sensors are installed to measure current, DC-link voltage and position. The DC voltage measurement is optional as it is assumed as constant in many control and estimation schemes (Bose, 2002). The position or current sensors are also eliminated in sensorless control schemes (Chang and Yeh, 1996; Ohnishi *et al.*, 1994). The control system determines the control input required to supply to the machine. The power converter transforms the control input to useful electrical power through different switching and modulation schemes.

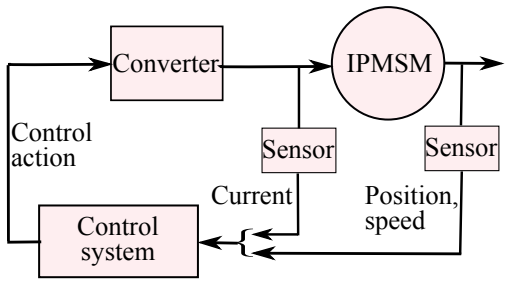

Figure 2.1: A typical IPMSM drive system.

An electric machine produces the torque required to supply to the load by the interaction of the stator and the rotor magnetic fields. For an IPMSM, the three-phase winding with three-phase excitation generates the stator field and permanent magnet supplies the rotor field. The distributed winding has been the norm for permanent magnet machines until recently the concentrated winding concept came into the picture (Bianchi *et al.*, 2006; EL-Refaie, 2010). The concentrated winding is easy to manufacture and has high slot fill factor with shorted end connections as it is

wound around each tooth. It has demonstrated considerable benefits for surface PM machines in terms of high power density, less cogging torque, fault tolerance, and field weakening capabilities (El-Refaie *et al.*, 2006), and it also has been combined with IPMSM to enhance the performance (Dutta *et al.*, 2013). The conceptual diagram of a distributed and concentrated winding is shown in Fig. 2.2. In the distributed winding the coils are distributed and generally spanned over a pole pitch (τ) however there are short pitch versions exist to mitigate specific harmonic contents in the magnetomotive force (mmf) (Srinivasan *et al.*, 2016). The concentrated winding is essentially the fractional slot (coil span is less than a pole pitch, $x\tau$) and the fraction x is mainly depended on the pole-slot combinations (Goss *et al.*, 2013).

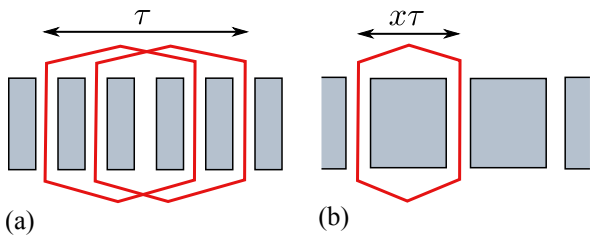

Figure 2.2: The conceptual diagram showing (a) distributed and (b) concentrated winding schemes for coils belong to a phase (τ-pole pitch).

The rotor topology of IPMSM is chosen to leverage flux concentration and saliency. There are three basic configurations viz., inset, spoke and barrier, which are combined to create different morphed configurations (Soong *et al.*, 2007). The spoke type topology generally has a high flux concentration factor and saliency and is hence suitable for applications where high permanent magnet induction is required or for low cost application where weaker magnets may be chosen, for example ferrite over sintered neodymium-iron-boron. The inset type topology features with moderate permanent magnet induction and saliency. The moderate permanent magnet induction

and saliency are obtained with barrier type topology however the saliency can be improved by adding more layers of permanent magnet barriers.

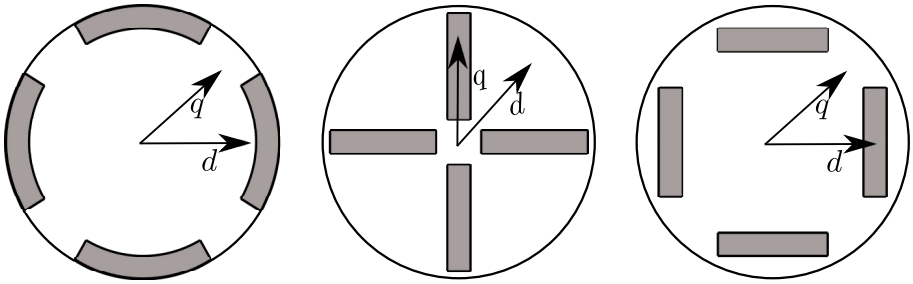

Figure 2.3: Three basic rotor configurations for IPMSM (a) inset, (b) spoke, and (c) barrier.

A power converter transforms DC power into AC or vice-versa depending on motoring or generating operations of an electric machine. The power conversion is performed by actuating power electronic switches, e.g. MOSFETs, and IGBTs, which are configured in different topologies. Some of the topologies are two-level voltage source inverter (VSI), multilevel VSI, and modular multilevel inverters (Nordvall, 2011). The nonlinear effects of the power electronic switches such as dead time and parasitic capacitance effects, unsymmetrical turn-on/off delays, and on-state voltage drops deteriorate the output power. The effects of these nonlinearities are compensated to improve the performance, especially for many estimation schemes (Salt *et al.*, 2011). The actuation signals generated by the control system are applied to the switches either directly or indirectly. The sinusoidal and space vector pulse width modulation schemes (SPWM and SVPWM) come under indirect method, employ a carrier-based modulation scheme. The SVPWM utilizes 15% more available DC link voltage than SPWM (De Doncker, 2002). The continuous voltage trajectory of SPWM and SVPWM along with finite six step modulation scheme is shown in Fig. 2.4 (a). In the direct method, the voltage vectors are applied directly based on

the predefined switching tables e.g., in a direct torque control scheme as shown in Fig. 2.4 (b).

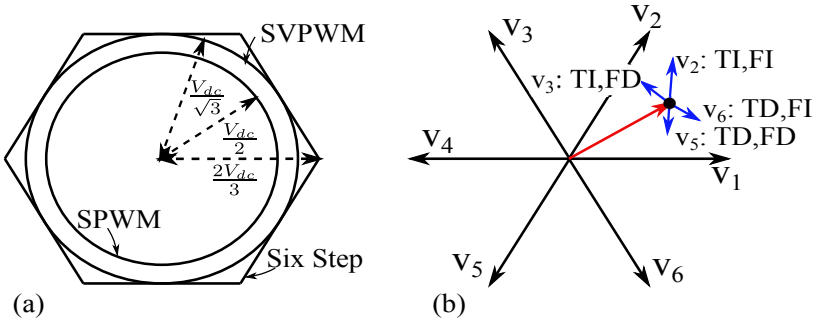

Figure 2.4: (a) Voltage trajectory of six step, SPWM, SVPWM modulation schemes (b) Voltage vector injection scheme of DTC (v_{dc}- dc link voltage, ψ_s stator flux vector, V_1,..,V_6- voltage vectors, FD: flux decrease, FI: flux increase, TI: torque increase, and TD: torque decrease).

Different control schemes generate the actuation signals. The most common schemes are vector and direct torque control. In the vector control, the rotating quadrature components of the current vector (d and q) are defined based on the rotor position in such a way that d component aligns with rotor flux. The d and q current components are controlled independently by linear controllers which generate the required voltage signals. In the vector control, the voltage signals are modulated employing SPWM or SVPWM to apply to an electric machine via a power converter. In the direct torque control (DTC), the torque and flux are controlled separately. The error between the reference and estimated torque and also flux are applied to hysteresis controllers. The voltage vectors are selected from a predefined lookup table (LuT) based on the output of the hysteresis controller and sector information. The control is usually performed in the stationary reference frame and therefore the rotor position information is not required as compared to the vector control. The block diagram of vector control and DTC are shown in Fig. 2.5 (a) and (b) respectively. The

DTC has simple control structure, involve no tuning and faster dynamic responses as compared to vector control however torque ripple is the downside.

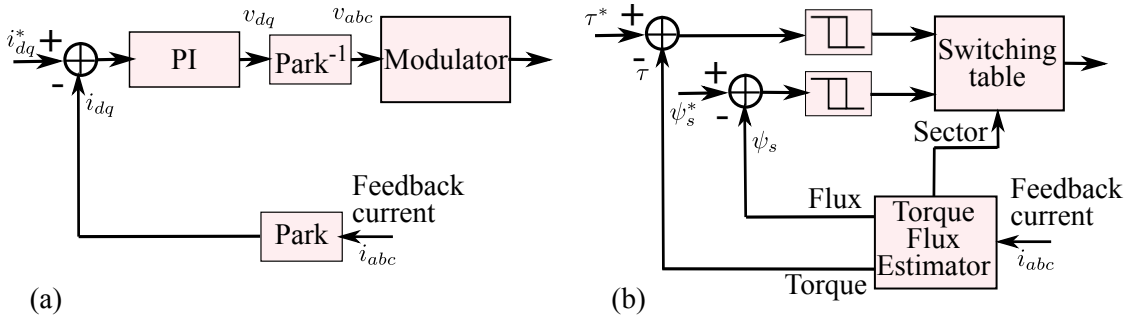

Figure 2.5: The block diagram of (a) vector control and (b) direct torque control.

The reference control values for vector control and DTC are basically derived from the torque or speed demands. An outer loop is added to Fig. 2.5 (a) and (b) to control the speed. In the traditional IPMSM control methods, i^*_d is kept as zero for the vector control and ψ^*_s is kept as a constant for DTC. Since IPMSM has salient rotor ($L_d \neq L_q$), it can also produce considerable reluctance torque apart from the magnetic torque by applying the appropriate i^*_d and ψ^*_s respectively for the vector control and DTC. This concept is applied in maximum torque per ampere (MTPA) control in which the minimum value of the components $((i^*_d, i^*_q),\ (\psi^*_s, i^*_\tau))$ are found for a given torque. The variable i^*_τ is the torque component of the current associated with DTC (Shinohara *et al.*, 2016). MTPA essentially minimizes the copper loss. Typical torque trajectories and MTPA curves in $d-q$ and $\psi^*_s - i^*_\tau$ planes employed in vector control and DTC are shown in Fig. 2.6 (a) and (b) respectively (Inoue *et al.*, 2016). The optimal reference values for MTPA is either applied from a LuT based on precomputed MTPA curve or found online by optimization or by search algorithms (Ge *et al.*, 2017; Kim *et al.*, 2013; Sun *et al.*, 2016). The other criteria considered

to generate reference (i_d^*, i_q^*) and (ψ_s^*, i_τ^*) are maximum torque per voltage, enhanced field weakening, and total loss minimization (Jahns *et al.*, 1986; Pan and Sue, 2005). In the total loss minimization approach, both iron and copper losses are minimized to achieve the optimal efficiency (Morimoto *et al.*, 1994).

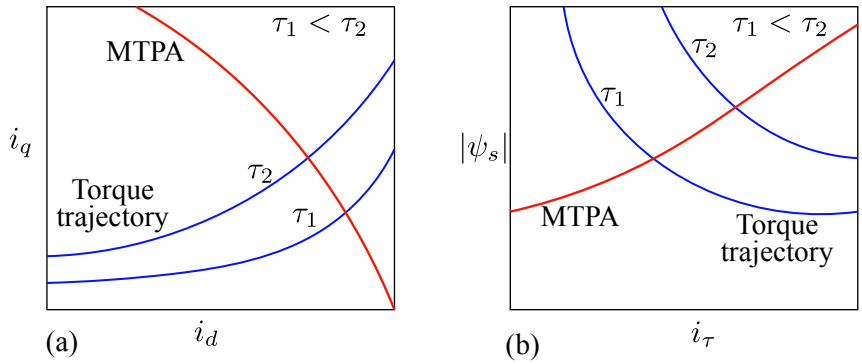

Figure 2.6: Typical MTPA curve and torque trajectories in (a) $d-q$ (b) $\psi_s^* - i_\tau^*$ planes.

2.3 IPMSM Model

The IPMSM model and the concept of transformation into different reference planes are explained with the help of a two pole machine as shown in Fig. 2.7. The two pole machine consists of three-phase armature winding in the stator and a bar magnet in the rotor. The phase coils are 120^o electrical apart to form a balanced three-phase winding.

The voltage equation by applying Kirchoff's law on the stator *abc* coils is

$$\mathbf{v}_{abc} = R\mathbf{i}_{abc} + \dot{\boldsymbol{\lambda}}_{abc} + \mathbf{i}v_n \tag{2.1}$$

where R is the phase resistance which is assumed to be equal for all the phases,

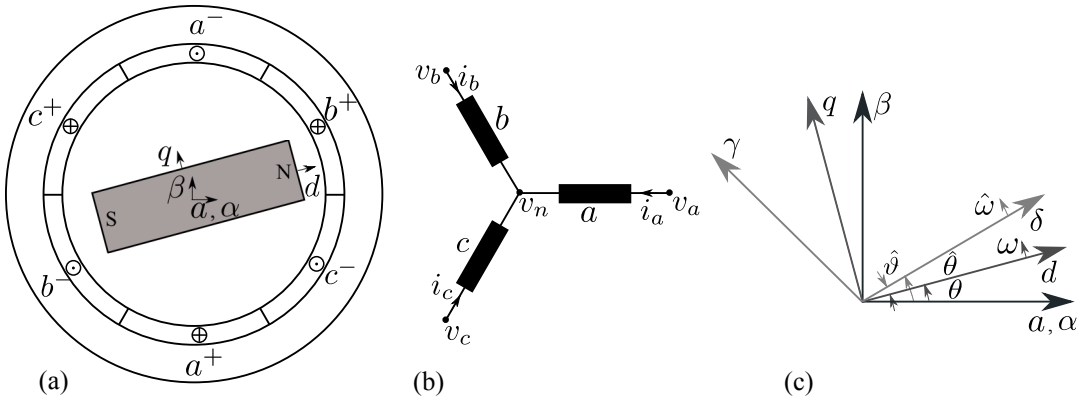

Figure 2.7: (a) 2 pole motor structure, (b) *abc* coils, and (c) reference frames.

$\mathbf{v}_{abc} = [v_a, v_b, v_c]' \in \mathbb{R}^3$ is the three phase sinusoidal voltage vector applied to the stator windings, $\mathbf{i}_{abc} = [i_a, i_b, i_c]' \in \mathbb{R}^3$ is the three phase sinusoidal phase current vector, $\boldsymbol{\lambda}_{abc} = [\lambda_a, \lambda_b, \lambda_c]' \in \mathbb{R}^3$ is the three phase flux linkage vector, $\mathbf{i} = [1, 1, 1]'$ and v_n is the neutral voltage. A balanced three phase system is assumed for analyzing and modeling of an electrical machine and hence $v_n = 0$. The three phase flux linkage $\boldsymbol{\lambda}_{abc}$ in (2.1) is expressed as

$$\boldsymbol{\lambda}_{abc} = \mathbf{L}_{abc}\mathbf{i}_{abc} + \boldsymbol{\psi}_{abc} \tag{2.2}$$

where $\mathbf{L}_{abc}$ is the inductance matrix of *abc* phases defined as (Paul C. Krause, 2002),

$$\mathbf{L}_{abc} = l_l\mathbf{I} + \mathbf{L}_a + \mathbf{L}_s, \tag{2.3}$$

l_l is the leakage inductance which is assumed to be same for all the phases, $\mathbf{I} \in \mathbb{R}^{3\times3}$ is the identity matrix, and $\mathbf{L}_a \in \mathbb{R}^{3\times3}$ and $\mathbf{L}_s \in \mathbb{R}^{3\times3}$ are the matrices consist of the average and the salient components of the three phase inductances respectively,

$$\mathbf{L}_a = l_a \begin{bmatrix} 1 & -\frac{1}{2} & -\frac{1}{2} \\ -\frac{1}{2} & 1 & -\frac{1}{2} \\ -\frac{1}{2} & -\frac{1}{2} & 1 \end{bmatrix}, \quad \mathbf{L}_s = l_s \begin{bmatrix} \cos 2(\theta) & \cos 2(\theta - \frac{\pi}{3}) & \cos 2(\theta + \frac{\pi}{3}) \\ \cos 2(\theta - \frac{\pi}{3}) & \cos 2(\theta - \frac{2\pi}{3}) & \cos 2(\theta + \pi) \\ \cos 2(\theta + \frac{\pi}{3}) & \cos 2(\theta + \pi) & \cos 2(\theta + \frac{2\pi}{3}) \end{bmatrix},$$

l_a is the average inductance and l_s is the peak of the salient inductance. The diagonal and off-diagonal elements in $\mathbf{L}_a$ and $\mathbf{L}_s$ represent self and mutual inductances respectively. The salient component of the inductance varies with respect to the rotor electrical position $\theta = \omega t$, where ω is the radial electrical speed and t is the time. The permanent magnet flux linkage in (2.2) also varies with respect to θ as

$$\boldsymbol{\psi}_{abc} = \psi_m \begin{bmatrix} \cos(\theta) \\ \cos(\theta - 2\frac{\pi}{3}) \\ \cos(\theta + 2\frac{\pi}{3}) \end{bmatrix} \tag{2.4}$$

where ψ_m is peak permanent magnet flux linkage. By substituting (2.3) in (2.2) and then into (2.1), it becomes,

$$\mathbf{v}_{abc} = R\mathbf{i}_{abc} + \mathbf{L}_{abc}\dot{\mathbf{i}}_{abc} + \omega\mathbf{L}_{abc_\theta}\mathbf{i}_{abc} + \omega\boldsymbol{\psi}_{abc_\theta} \tag{2.5}$$

where $L_{abc_\theta} = \frac{d}{d\theta}(\mathbf{L}_{abc})$ and $\boldsymbol{\psi}_{abc_\theta} = \frac{d}{d\theta}(\boldsymbol{\psi}_{abc})$.

For simplicity in analysis and control (e.g., for direct torque control), the three-phase model is often transformed into two-axis stationary reference frame ($\alpha\beta$). This transformation also generates zero sequence term which is generally ignored in analysis and design of control systems. The transformed (2.5) in ($\alpha\beta$) frame is

$$\mathbf{v}_{\alpha\beta} = R\mathbf{i}_{\alpha\beta} + \mathbf{L}_{\alpha\beta}\dot{\mathbf{i}}_{\alpha\beta} + \omega\mathbf{L}_{\alpha\beta_\theta}\mathbf{i}_{\alpha\beta} + \omega\boldsymbol{\psi}_{\alpha\beta} \tag{2.6}$$

where $\mathbf{v}_{\alpha\beta} = \mathbf{T}_{\alpha\beta}\mathbf{v}_{abc} \in \mathbb{R}^2$, $\mathbf{i}_{\alpha\beta} = \mathbf{T}_{\alpha\beta}\mathbf{i}_{abc} \in \mathbb{R}^2$, $\mathbf{L}_{\alpha\beta} = \mathbf{T}_{\alpha\beta}\mathbf{L}_{abc}\mathbf{T}_{\alpha\beta}^{-1} \in \mathbb{R}^{2\times2}$, $\mathbf{L}_{\alpha\beta_\theta} = \frac{d}{d\theta}(\mathbf{L}_{\alpha\beta}) \in \mathbb{R}^{2\times2}$, $\boldsymbol{\psi}_{\alpha\beta} = \mathbf{T}_{\alpha\beta}\boldsymbol{\psi}_{abc_\theta} \in \mathbb{R}^2$, and $\mathbf{T}_{\alpha\beta}$ is Clarke's transformation matrix as detailed in Appendix A. The inductance matrix $\mathbf{L}_{\alpha\beta}$ is expanded as

$$\mathbf{L}_{\alpha\beta} = \begin{bmatrix} \frac{3}{2}(l_a - l_s\cos(2\theta)) + l_s & -\frac{3}{2}l_s\sin(2\theta) \\ -\frac{3}{2}l_s\sin(2\theta) & \frac{3}{2}(l_a + l_s\cos(2\theta)) + l_s \end{bmatrix} \tag{2.7}$$

The expression (2.7) is commonly known with its compact form, i.e.,

$$\mathbf{L}_{\alpha\beta} = L_\Sigma\mathbf{I} + L_\Delta\mathbf{P} \tag{2.8}$$

where $L_\Sigma = \frac{3}{2}l_a + l_s$, $L_\Delta = -\frac{3}{2}l_s$, and $\mathbf{P} = [[\cos(2\theta),\ \sin(2\theta)]', [\sin(2\theta), -\cos(2\theta)]']$. By substituting (2.8) in (2.6), its common form is expressed as

$$\mathbf{v}_{\alpha\beta} = R\mathbf{i}_{\alpha\beta} + (L_\Sigma\mathbf{I} + L_\Delta\mathbf{P})\dot{\mathbf{i}}_{\alpha\beta} + 2\omega L_\Delta\mathbf{T}_r\mathbf{P}\mathbf{i}_{\alpha\beta} + \omega\boldsymbol{\psi}_{\alpha\beta} \tag{2.9}$$

where $T_r = [[0, 1]', [-1, 0]']$ is the rotational matrix.

For the field oriented control (vector control), the IPMSM model (2.9) is transformed into the rotor reference frame (dq), i.e.,

$$\mathbf{v}_{dq} = R\mathbf{i}_{dq} + \mathbf{L}_{dq}\dot{\mathbf{i}}_{dq} + \omega\mathbf{T}_r\mathbf{L}_{dq}\mathbf{i}_{dq} + \omega\boldsymbol{\psi}_{dq} \tag{2.10}$$

where $\mathbf{v}_{dq} = \mathbf{T}_{dq}\mathbf{v}_{\alpha\beta} \in \mathbb{R}^2$, $\mathbf{i}_{dq} = \mathbf{T}_{dq}\mathbf{i}_{\alpha\beta} \in \mathbb{R}^2$, $\mathbf{L}_{dq} = \mathbf{T}_{dq}\mathbf{L}_{dq}\mathbf{T}_{dq}^{-1} \in \mathbb{R}^{2\times2}$, $\boldsymbol{\psi}_{dq} = \mathbf{T}_{dq}\boldsymbol{\psi}_{\alpha\beta} \in \mathbb{R}^2$, and $\mathbf{T}_{dq}$ is Parks's transformation matrix as detailed in Appendix A.

The permanent flux linkage term, $\boldsymbol{\psi}_{dq} = \psi_m[1, 0]'$. The inductance matrix,

$$\mathbf{L}_{dq} = \begin{bmatrix} L_\Sigma + L_\Delta & 0 \\ 0 & L_\Sigma - L_\Delta \end{bmatrix}, \tag{2.11}$$

and therefore d and q inductance are defined as

$$L_d = L_\Sigma + L_\Delta \quad \text{and} \quad L_q = L_\Sigma - L_\Delta. \tag{2.12}$$

The machine model is often transformed from dq to estimated rotor reference frame ($\delta\gamma$) in many position sensorless techniques. The $\delta\gamma$ frame rotates with estimated angular velocity $\hat{\omega}$ and displaced from the dq frame with an estimated angular difference $\hat{\vartheta}$ as shown in Fig.2.7 (c). The transformed voltage equation is

$$\mathbf{v}_{\delta\gamma} = R\mathbf{i}_{\delta\gamma} + \mathbf{L}_{\delta\gamma}\dot{\mathbf{i}}_{\delta\gamma} + \mathbf{T}_r\mathbf{L}_{\delta\gamma}\hat{\omega}\mathbf{i}_{\delta\gamma} + \hat{\omega}\boldsymbol{\psi}_{\delta\gamma}. \tag{2.13}$$

where $\mathbf{v}_{\delta\gamma} = \mathbf{T}_{\delta\gamma}\mathbf{v}_{dq} \in \mathbb{R}^2$, $\mathbf{i}_{\delta\gamma} = \mathbf{T}_{\delta\gamma}\mathbf{i}_{dq} \in \mathbb{R}^2$, $\mathbf{L}_{\delta\gamma} = \mathbf{T}_{\delta\gamma}\mathbf{L}_{dq}\mathbf{T}_{\delta\gamma}^{-1} \in \mathbb{R}^{2\times2}$, $\boldsymbol{\psi}_{\delta\gamma} = \mathbf{T}_{\delta\gamma}^{-1}\boldsymbol{\psi}_{\alpha\beta} \in \mathbb{R}^2$, and $\mathbf{T}_{\delta\gamma}$ is Parks's transformation with respect to $\hat{\vartheta}$. The permanent magnet flux linkage $\boldsymbol{\psi}_{\delta\gamma} = \psi_m[-\sin\hat{\vartheta},\ \cos\hat{\vartheta}]'$, and the inductance matrix $\mathbf{L}_{\delta\gamma} = L_\Sigma\mathbf{I} + \tilde{P}L_\Delta$, where $\tilde{\mathbf{P}} = [[\cos(2\hat{\vartheta}), \sin(2\hat{\vartheta})]', [\sin(2\hat{\vartheta}), -\cos(2\hat{\vartheta})]']$.

2.4 Parameter Variation

The machine parameters in (2.10) are generally assumed to be constants in standard control schemes. However, the parameters vary with respect to the operating condition of the machine. The actual parameters considering the variations are either

updated from a lookup table or by estimation in the advanced control techniques e.g. position sensorless and optimal controls.

The phase resistance varies with respect to frequency and temperature. The resistance variation due frequency is attributed to skin and proximity effects and the additional resistive component by these effects collectively know as AC (alternating current) resistance. Apart from the frequency, AC resistance slightly varies with respect to phase current and field weakening angle as magnetic flux deforms by saturation and armature reaction (Nalakath *et al.*, 2015). The variation of AC resistance with respect to frequency, current and field weakening angle for a rectangular conductor winding is taken from (Nalakath *et al.*, 2015) and depicted in Fig. 2.8 (a).

The remanent flux density decreases with rising in temperature for both ceramic and rare-earth permanent magnets. It varies about 15 to 25% by 160^o temperature rise from room temperature (Hamidizadeh, 2016). The rare-earth magnet becomes vulnerable to demagnetization at the higher temperature as the knee point shift more towards the lower coercive force as shown in Fig. 2.8 (b). The irreversible demagnetization occurs if the coercive force crosses the knee point and therefore utmost care should be taken at the design and while operation of the rare-earth magnet machines. On the other hand, for the ceramic magnets, the knee point shift towards higher coercive force with temperature rise and hence less vulnerable to demagnetization.

The stator winding inductance varies with respect to the saturation of the core. The saturation of the core occurs at high excitation currents in accordance with the B-H relationship of the core material. The inductance of the IPMSM machine is generally defined for rotating quadrature axes dq. Apart from the saturation by

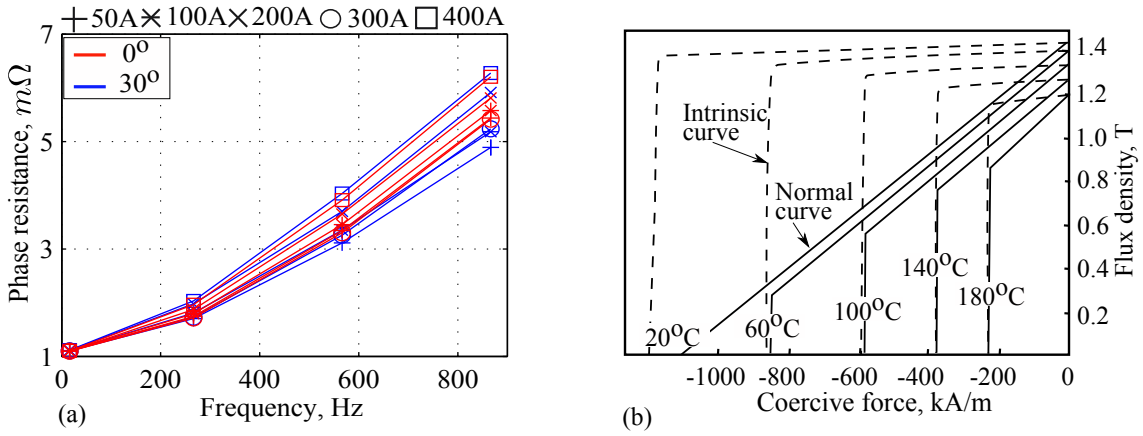

Figure 2.8: (a) Variation of resistance with respect to frequency and peak phase current for field weakening angle 0^o and 30^o (Nalakath *et al.*, 2015), (b) characteristics of TDI Neorec53B iron-based rare-earth magnet Yang *et al.* (2017).

self-excitation of a quadrature coil, there is also a considerable influence from the excitation of other quadrature coil, known as cross-saturation. The cross-saturation is closely related to the armature reaction of a direct current machine under saturation which leads to different variations in the flux densities at tips of a pole resulting in additional flux linkage in the coil . This additional flux linkage can be viewed as the result of the cross-saturation (Vas *et al.*, 1986). The cross saturation also results in mutual inductance between the two quadrature coils. The cross-saturation effect in the inductances is either expressed implicitly or explicitly and correspondingly they are known as apparent and incremental inductances (Gong, 2012). The apparent inductances are defined as

$$\begin{cases} L_d = \frac{\lambda_d}{i_d} \\ L_q = \frac{\lambda_q}{i_q} \end{cases} \tag{2.14}$$

where λ_d and λ_q are the d and q flux linkages respectively, and these are either measured or found from the finite element analysis (FEM) software. In the explicit

form, the inductance matrix in (2.11) is redefined as

$$\mathbf{L}_{dq} = \begin{bmatrix} L_{dd} & L_{dq} \\ L_{qd} & L_{qq} \end{bmatrix}, \tag{2.15}$$

where L_{dd} and L_{qq} are the self incremental d and q inductances respectively, and L_{dq} and L_{qd} are the mutual incremental inductances. The mathematical definition of these inductances are

$$\begin{cases} L_{dd} = \frac{\partial \lambda_d}{\partial i_d} & L_{dq} = \frac{\partial \lambda_d}{\partial i_q} \\ L_{qd} = \frac{\partial \lambda_q}{\partial i_d} & L_{qq} = \frac{\partial \lambda_q}{\partial i_q} \end{cases} \tag{2.16}$$

By the definition of the mutual inductances, $L_{dq} = L_{qd}$. The typical d and q flux linkage profiles and the graphical interpretation of the incremental and the apparent inductances are depicted in Fig. 2.9. The d axis flux linkage saturates with positive i_d, and the flux in the core weakens with negative i_d and hence no saturation. The q axis flux linkage saturates on both directions of i_q and it is symmetrical with respect to $i_q = 0$ axis.

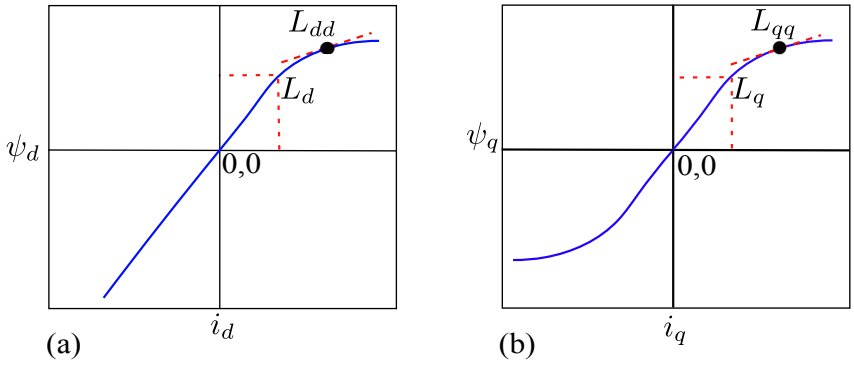

Figure 2.9: Typical flux linkage profile of IPMSM (a) for d-axis, and (b) for q-axis

2.5 Summary

In an electric machine drive system, the control references as per the load demand is processed in a control system against the feedback and applies the control output to an electric machine via a power converter either directly or with a modulator. This chapter briefly introduces a typical IPMSM drives system and describes the different components. The criteria for generating the references for the advanced control of IPMSMs are mentioned. The mathematical models of IPMSM in different reference frames are presented, and the variations of the machine parameters with respect to operating conditions are discussed.

Chapter 3

Model Predictive Control (MPC)

3.1 Introduction

In model predictive control, a quadratic cost function is optimized along with constraints over a finite prediction horizon at each sampling interval and applies the first of the resulting control sequence to the plant. This chapter starts by describing a general model predictive control (MPC) scheme and introduces the relevant constrained finite-horizon optimal control problem. The variants of MPC classified based on the different approaches to solve the optimal control problem are discussed. The literature review on the application of these variants on electric motor drive applications is also presented emphasizing computational effectiveness.

3.2 The Concept of MPC

In model predictive control (MPC), a constrained finite-horizon optimal control problem (CFHOC) is solved at each sampling interval with current state feedback of the

plant as the initial state. The solution of CFHOC yields an optimal open-loop control sequence and the first in the sequence is only applied to the plant according to the receding horizon policy. The process is repeated for the next sampling interval by receding the prediction horizon and updating the state feedback. This approach evolves in a real closed loop feedback control over the sampling intervals (Linder and Kennel, 2005a).

The structure of a typical MPC is depicted in Fig. 3.1. The plant model predicts the future response $\mathbf{x}_{k,i+1}$ with respect to the previous predicted state $\mathbf{x}_{k,i}$ and the optimal control sequence $\mathbf{u}_{k,i}$. Where k is the sampling interval and $i = 1, 2, ..N$ is the index for the divisions of the prediction horizon (N). The initial state $\mathbf{x}_{k,0}$ is the state feedback $\mathbf{x}_k$ at k^{th} sample. The optimizer solves CFHOC problem at each sampling interval. The CFHOC is formulated as a cost function along with the given constraints. The optimal solution of CFHOC is the control sequence $\mathbf{u}_k = [u_{k,0}, u_{k,1}, ...u_{k,N}]$ computed for prediction horizon N. The MPC tracks the response close to the reference value $\mathbf{w}_k$ over the sampling intervals by applying only the first of the control sequence $u_{k,0}$ to the plant as shown in Fig. 3.2.

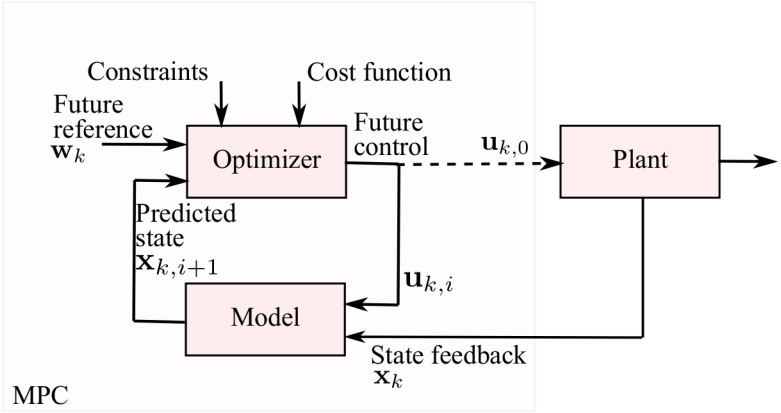

Figure 3.1: The structure of a typical model predictive control scheme.

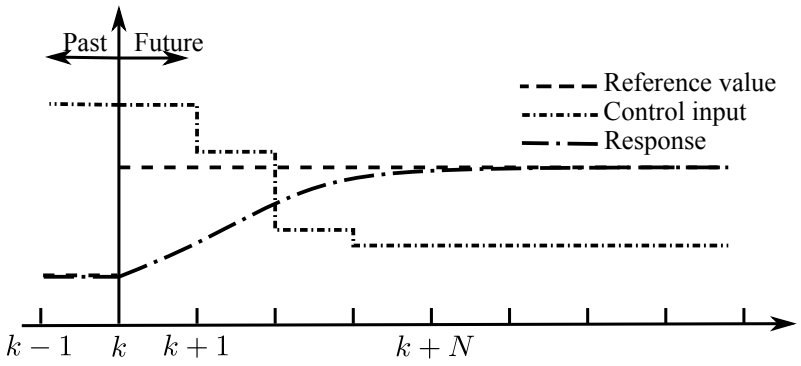

Figure 3.2: The receding horizon scheme of model predictive control.

In order to discuss the mathematical treatment of MPC, a discrete-time state space model is defined at first, i.e.

$$\begin{cases} \mathbf{x}_{k+1} = \mathbf{A}\mathbf{x}_k + \mathbf{B}\mathbf{u}_k \\ \mathbf{y}_k = \mathbf{C}\mathbf{x}_k + \mathbf{D}\mathbf{u}_k \end{cases} \tag{3.1}$$

where the system variables satisfy the constraints $\mathbf{x} \in \boldsymbol{\mathcal{X}} \subset \mathbb{R}^n$, $\mathbf{y} \in \boldsymbol{\mathcal{Y}} \subset \mathbb{R}^p$, $\mathbf{u} \in \boldsymbol{\mathcal{U}} \subset \mathbb{R}^m$. Moreover, a general cost function for MPC is defined as (Lee, 2011)

$$f_N = \mathbf{x}'_{k+N}\mathbf{P}\ \mathbf{x}_{k+N} + \sum_{i=1}^{N} \left(\mathbf{x}'_{k+i-1}\mathbf{Q}\ \mathbf{x}_{k+i-1} + \mathbf{u}'_{k+i-1}\mathbf{R}\mathbf{u}_{k+i-1}\right) \tag{3.2}$$

where $\mathbf{P} \succeq 0$ is the weighting matrix for the final value, $\mathbf{Q} \succeq 0$ weights the state vector, and $\mathbf{R} \succ 0$ penalize the control action. In order to find the optimal control

input, the cost function (3.2) is minimized subject to the constraints

$$\begin{cases} \mathbf{x}_{k+i} \in \boldsymbol{\mathcal{X}} \\ \mathbf{u}_{k+i} \in \boldsymbol{\mathcal{U}} \\ \mathbf{x}_{k+i+1} = \mathbf{A}\mathbf{x}_{k+i} + \mathbf{B}\mathbf{u}_{k+i} \end{cases} \tag{3.3}$$

The state at step i as the superposition of free and driven responses is

$$\mathbf{x}_{k+i} = \mathbf{A}^i \mathbf{x}_k + \sum_{j=1}^{i-1} \mathbf{A}^j \mathbf{B}\mathbf{u}_{k+i-1-j} \tag{3.4}$$

The cost function is expressed as a function of only the initial state and the control input by substituting (3.4) in (3.2) i.e.

$$f_N(\mathbf{x}_k) = \frac{1}{2}\mathbf{x}_k' \mathbf{Y}\ \mathbf{x}_k + \frac{1}{2}\mathbf{U}'\mathbf{H}\mathbf{U} + \mathbf{x}_k'\mathbf{F}\mathbf{U} \tag{3.5}$$

Similarly the constraints can also be expressed as a function of only the initial state and the control input, i.e.

$$\mathbf{G}\mathbf{U} \leq \mathbf{W} + \mathbf{E}\mathbf{x}_k \tag{3.6}$$

where $\mathbf{U} = [\mathbf{u}_k', ..., \mathbf{u}_{k+N-1}']' \in \mathbb{R}^{mN}$ is the input control sequences corresponding to each time steps from k to $k+N-1$. The matrices $\mathbf{H} \succ 0$, $\mathbf{F}$, $\mathbf{Y}$, $\mathbf{G}$, $\mathbf{W}$, and E are found from (3.2) (Linder and Kennel, 2005b).

The transformed cost function (3.5) with the constraints (3.6) is the CFHOC problem to be solved. This is essentially a quadratic programming (QP) problem (Linder and Kennel, 2005b). The analytical solution of the CFHOC is not viable due to the constraints (Maciejowski, 2002). There are numerical solvers for QP available

in literature (Cooper and Steinberg, 1970; Hadley, 1964). These solvers take a long time to solve the CFHOC and therefore the application of MPC was limited to the systems with slow dynamics especially at the beginning era (1960-1970) of MPC development (Lee, 2011).

The faster solvers were later developed for MPC that facilitated its application to moderate dynamic systems. This line of research has been motivated by the development of high performance computing resources (Lee, 2011; Qin and Badgwell, 2003a,b; Frison *et al.*, 2014a). This approach by solving optimization problem online is collectively known as implicit MPC. Apart from online optimization for MPC there has been concurrent research on solving CFHOC offline and this approach is known as explicit MPC (Bemporad *et al.*, 2000, 2002). In explicit MPC, CFHOC problem is decomposed into piecewise affine control laws valid over precomputed affine regions and solved offline. The associated region is identified online based on the current state and the corresponding stored control is applied to the plant, and therefore results in shorter overall execution time.

3.3 Features of MPC

The MPC is a state space model based control and therefore it can handle multiple-input and multiple-output (MIMO) systems. Unlike the cascaded control systems, many system variables can be controlled with a single control loop for MPC as shown in Fig. 3.3 (Camacho and Carlos, 2007). This feature is very important especially for the complex systems with several control variables. The challenges in applying the constraints have been almost limited the application of the conventional states space controllers (Bolognani *et al.*, 2009). On other hand, the system input and

output constraints can be easily incorporated with MPC. Solving the closed-loop control is not required for the case of MPC as it establishes implicitly the feedback control. The constrained open-loop control problem is only required to be solved unlike the traditional state space based controllers (Kouvaritakis and Cannon, 2016). The resulting control law is linear and hence easy to implement.

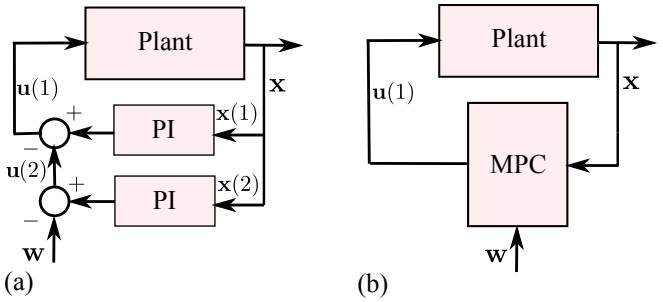

Figure 3.3: (a) A typical cascaded controller (PI-Proportional Integral), and (b) MPC Controller.

The MPC is suitable for versatile applications as it allows modifying the cost function according to the requirements without any change in the control structure (Linder and Kennel, 2005b). Any objective function can be simply added and the weighting factors can be freely varied. These features are very important in multi-objective control e.g. torque and speed tracking with optimal efficiency for the motor drives. The MPC is able to manage the deterministic disturbances. If these disturbances are known before they can be accustomed with the optimizer (Linder and Kennel, 2005b). Accordingly, the corrective measures can be taken in the future control action. The MPC is also has some degree of robustness with the parameter variation as there is a implicit feedback control (Camacho and Carlos, 2007). Moreover, the finite control input can be incorporated as constraints in MPC that allows direct actuation (without a modulator) for electric motor drives (Linder and Kennel, 2005a).

3.4 MPC for Electric Motor Drives

The model predictive control has been applying into electric motor drive applications since mid of the 2000s as the result of emerging fast MPC techniques and powerful computational resources. The straightforward inclusion of the constraints and the elimination of the cascaded control blocks are also the motivational factors influenced the researchers to employ the MPC for electrical drives. The earlier research on the application of MPC for electrical drives was mainly focused on the explicit MPC in which the optimization is solved offline (Linder and Kennel, 2005a; Bolognani *et al.*, 2009; Mariethoz *et al.*, 2012). The implicit MPC has been explored at the later stage by incorporating the standard as well as the customized solvers (Besselmann *et al.*, 2016; Saeidi and Kennel, 2013; Preindl *et al.*, 2013). There are two sub-variants for implicit and explicit MPCs known as direct and indirect MPCs. The indirect MPC applies the control law to the electric machine by means of a modulator whereas the control law is applied without a modulator for the case of the direct MPC. In the direct MPC, the control law is essentially the optimum finite switching state.

3.4.1 Explicit MPC

The explicit MPC is suitable for the system with fast dynamics as it applies the offline optimized control law to the plant. This technique was first published in (Bemporad *et al.*, 2000). In order to mathematically explain the explicit MPC, first an auxiliary variable is defined as

$$\mathbf{z} = \mathbf{U} + \mathbf{H}^{-1}\mathbf{F}'\mathbf{x}_k \qquad \mathbf{z} \in \mathbb{R}^s \tag{3.7}$$

and by completing the squares, QP cost function (3.5) can be transformed into an equivalent form as

$$f_z(\mathbf{x}_k) = \frac{1}{2}\mathbf{z}'\mathbf{H}\mathbf{z} \tag{3.8}$$

with constraints

$$\mathbf{G}\mathbf{z} \leq \mathbf{W} + \mathbf{S}\mathbf{x}_k \tag{3.9}$$

where $\mathbf{S} = \mathbf{E} + \mathbf{G}\mathbf{H}^{-1}\mathbf{F}'$. In the transformed problem, the state $\mathbf{x}_k$ appears only with the constraints. By considering $\mathbf{x}_k$ as a parameter, the original QP problem (3.5) is converted to multi-parametric QP problem (mp-QP). The mp-QP problem is solved offline with the help of parametric nonlinear programming (Bemporad *et al.*, 2000). In order to solve mp-QP problem, the initial value $\mathbf{x}_0$ is found first which is Chebychev center of $\mathscr{X}$ (Bemporad *et al.*, 2002). The solution of mp-QP is piecewise affine i.e. the optimal control law is an affine function of states which is divided into several convex regions or polytopes . In other words, the optimal control law takes the form

$$\mathbf{u}_{k,l} = \mathbf{F}_l\mathbf{x}_k + \mathbf{G}_l \tag{3.10}$$

where l is the index of the active convex region where the state $\mathbf{x}_k$ is at k^{th} sampling time, and $\mathbf{F}_l$ and $\mathbf{G}_l$ are from the mp-QP offline optimization. Therefore, the online task in explicit MPC lies only in identifying the active region with respect to the measured states and applies the predefined linear control law corresponding to the region.

The explicit MPC has been applied to induction as wells as synchronous permanent magnet machine drives to control current, torque and speed. The control law is either applied through a modulator (Continuous Explicit MPC) (Linder and Kennel,

2005b; Bolognani *et al.*, 2009) or by directly applying the finite switching states of a multi-level inverter (Direct Explicit MPC) (Linder and Kennel, 2005a; Geyer, 2011).

Continuous Explicit MPC

In continuous explicit MPC, the control input $\mathbf{u}$ has only upper and lower bound constraints and within these bounds it is continuous. This enables to apply the standard mp-QP solving techniques. The solution of mp-QP results in continuous $\mathbf{u}$ which is essentially the control voltage for the electric drives, belongs to a continuous space $\mathcal{U}$ with infinite possibilities. In order to apply the continuous control voltage to an electric machine a modulator is necessary. Fig. 3.4 shows a typical scheme of a continuous explicit MPC for electric motor drives.

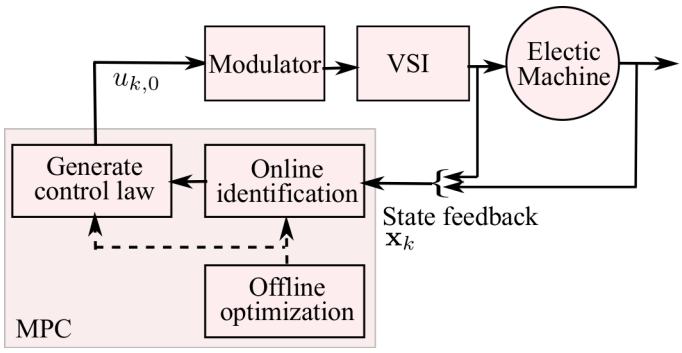

Figure 3.4: A typical continuous explicit MPC scheme for electric motor drives.

The continuous explicit MPC scheme is applied to an induction machine to regulate the current in (Linder and Kennel, 2005b) and for speed and current control in (Mariethoz *et al.*, 2012). The applications of explicit MPC scheme for permanent magnet synchronous machine to control current and speed are found in (Bolognani *et al.*, 2009) and with field weakening feature is presented in (Bolognani *et al.*, 2008).

Direct Explicit MPC

In direct explicit MPC, the control input is essentially the finite switching states of a multilevel inverter. Fig. 3.5 (a) shows eight possible switching states of a two level inverter which is adopted in this thesis. With finite switching variables, the system under consideration is commonly referred as hybrid system as this also contains continuous variables (e.g. currents). The finite switching states is considered as control input constraints to simplify the problem formulation. The solution of CFHOC for hybrid system is performed by using mixed-integer linear (MILP) or mixed integer quadratic programming (MIQP) (Linder and Kennel, 2005a). Fig. 3.5 (b) shows a typical direct explicit MPC scheme for electric motor drives.

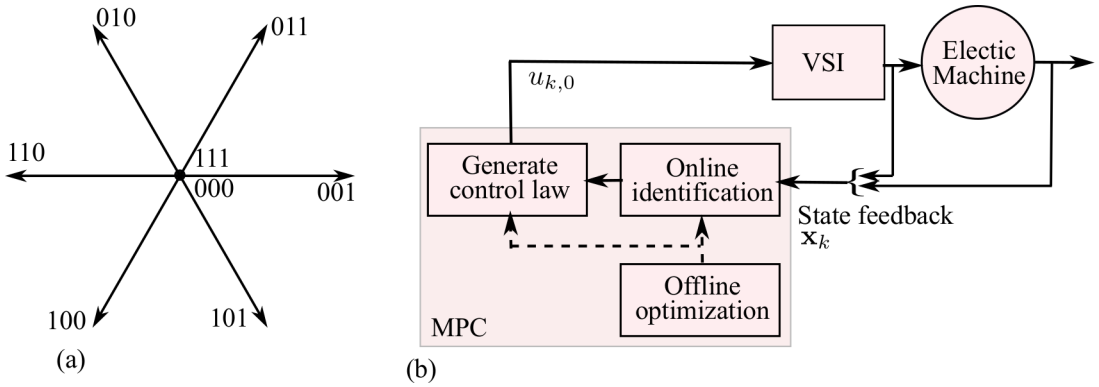

Figure 3.5: (a) Switching states of a two level inverter, and (b) a typical direct explicit MPC scheme for electric motor drives.

A direct explicit MPC is implemented for current regulation of an induction machine with a two-level inverter in (Linder and Kennel, 2005a). In (Geyer, 2011), the torque of an induction machine with a three level neutral point clamped inverter is controlled along with reducing the switching loss and frequency.

3.4.2 Implicit MPC

In implicit MPC, the CFHOC problem is solved online. As the analytical solutions to CFHOC are not viable due to the constraints, the numerical solutions by optimization are preferred. Moreover, the CFHOC problem is a QP problem with inequality constraints, and therefore active set (AS) and interior point (IP) based optimization techniques are generally employed (Frison *et al.*, 2014a,c). These are the second order solvers. The first order solver e.g. gradient method is also applied in some of the MPC applications (Frison *et al.*, 2014a). There are several variants of these solvers to improve the computational performance related to application of MPC (Wang and Boyd, 2010; Frison *et al.*, 2014b; A. Domahidi and Jones, 2012; Frison *et al.*, 2014c). The warm start initialization and early termination are also found to be the effective techniques to reduce the computational time (Wang and Boyd, 2010). With the help of fast optimization solvers and advanced computational resources, the implicit MPC technique is also started applying to electric motor drives. Similar to explicit MPC, both continuous and direct variants exist also for implicit MPC applied to motor drives.

Continuous Implicit MPC

In continuous implicit MPC, the control input which is the excitation voltage for the case of electric motor drives, is continuous and bounded in the subspace vector $\mathscr{U}$. The CFHOC problem is solved online by applying the fast QP solvers, results in control input which has infinite possibilities. Apart from employing fast MPC, the length of prediction horizon is also chosen in such a way that the accurate control and fast optimization are accomplished. A modulator is implemented to apply continuous

control input $\mathbf{u}_k$ to the electric machine as shown in Fig. 3.6.

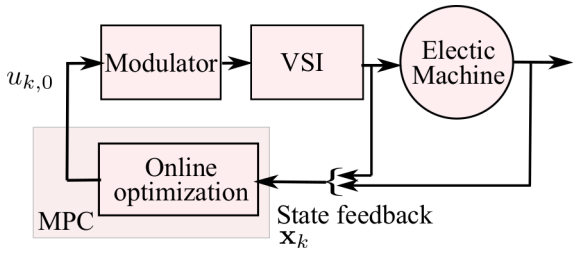

Figure 3.6: A typical direct implicit MPC scheme for electric motor drives.

A parametric active-set algorithm for quadratic programming is employed to control the current and speed of a MW range synchronous machine in (Besselmann *et al.*, 2016). In (Cimini *et al.*, 2015), an efficient QP solver is implement to realize the torque control of permanent magnet synchronous machine. The torque control of permanent magnet synchronous machine by optimizing CFHOC problem by fast gradient method is presented in (Preindl *et al.*, 2013).

Direct Implicit MPC

The finite nature of the switching states simplifies the optimization problem for the direct implicit MPC and hence widely employed for electric motor drive applications. The optimization of CFHOC problem consists of finding the control sequence corresponding to the minimum cost among the costs for predefined control sequences. The control sequences are defined based on the possible switching transitions of a multilelvel inverter. The possible switching transitions of a two-level inverter is shown in Fig. 3.7 (a). A typical scheme of direct implicit MPC is shown in Fig. 3.7 (b).

The direct implicit MPC is implemented to control the torque and flux of an induction machine with a three level inverter in (Geyer *et al.*, 2009). The same work is continued in (Geyer, 2009) with extended horizon focusing on reducing the switching

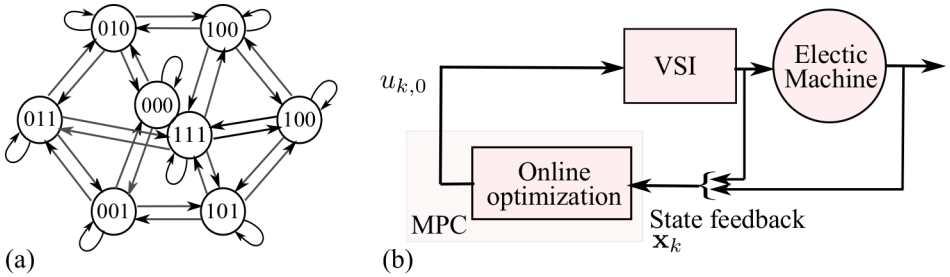

Figure 3.7: (a) Possible switching transitions for a two-level inverter, and (b) a typical direct implicit MPC scheme for electric drives.

losses and total harmonic distortion. The direct implicit MPC for torque control with long prediction horizon is generally known as model predictive direct torque control (MPDTC). The execution time of MPDTC is improved by discarding the suboptimal switching sequences while keeping the long prediction horizon in (Geyer, 2011). The MPDTC technique is applied to permanent magnet synchronous machine in (Geyer *et al.*, 2010). The direct implicit MPC is also referred as finite control set model predictive control (FCSMPC), especially for the application where the prediction horizon is too short. The FCMPC technique is applied to permanent magnet synchronous machine with a two level inverter to control the torque along with maximum torque per ampere tracking with a single sample prediction horizon ($N = 1$) in (Preindl and Bolognani, 2013c). The similar technique is also applied to control the speed of a permanent magnet synchronous machine in (Preindl and Bolognani, 2013b). An detailed overview of FCSMPC for electric drive applications is found in (Wang *et al.*, 2017).

3.5 Summary

The model predictive control (MPC) has been recently applied to electric motor drive applications in order to effectively manage the constraints and to avoid cascaded control loops. The main challenge in employing the model predictive control (MPC) in any fast dynamic systems comes from solving the constrained finite horizon open-loop control problem (CFHOC) online. Fortunately, the CFHOC problem is piece-wise affine in a convex region and therefore the control law can be solved offline and applied to the plant upon determining the active convex region online (Explicit MPC). As the storage and handling is problematic for explicit MPC especially for the systems with many variables, the researchers has started solving the CFHOC problem online (Implicit MPC) with the help of emerging computational technologies and solvers. In finite control set MPC, a variant of implicit MPC, the computation effort is greatly reduced due to the finite nature of the cost function and hence widely employed to electric motor drive applications.

Chapter 4

Persistent Excitation by Finite Control Set (FCS) MPC Enabling Identification of Position, Speed and Parameters

4.1 Introduction

This chapter starts by introducing the notion of persistent excitation and its relationship with observability. The concept of local observability is employed in this thesis and discussed in detail as the standard observability techniques cannot be applied to IPMSM which is nonlinear. The persistent excitation requirements to enable the observability of the position, speed and the parameters for IPMSM are laid out. The response of the voltage vector injections associated with FCSMPC is analyzed on the context of persistent excitation requirements to achieve observability.

4.2 Notion of Persistent Excitation and Observability

An input that persistently excites all the modes of the system enabling the identification of the system parameters is a persistent excitation (PE) (Pelckmans, 2010). If a discrete time input signal $\mathbf{u}_k \in \mathbb{R}^n$ is a PE where k is the sampling index, then the following exists for all τ (Jung, 1971)

$$\begin{cases} r_\tau = \lim\limits_{N\to\infty} \sum_{k=0}^{N} (\mathbf{u}_k - \bar{\mathbf{u}})'(\mathbf{u}_{k+\tau} - \bar{\mathbf{u}}) \\ \bar{\mathbf{u}} = \lim\limits_{N\to\infty} \sum_{k=0}^{N} \mathbf{u}_k \\ \mathbf{R}_N = \mathrm{cov}(r_\tau) \succ 0 \end{cases} \tag{4.1}$$

where $\mathbf{R}_N$ is the covariance matrix of r_τ, and it needs to be positive definite for $\mathbf{u}_k$ to be a PE input (Jung, 1971).

The observability has close relation with PE as the system becomes observable to the parameters if it is persistently excited (Rusnak *et al.*, 1993). Therefore, PE requirements to identify the parameters, is a problem of finding the observability conditions. In this thesis, since IPMSM with parameter variations is a nonlinear system, the observability is analyzed with the help of nonlinear observability technique and arrived at PE conditions identifying the parameters.

4.2.1 Nonlinear Observability Concept

Analyzing the global observability for nonlinear dynamic systems is challenging in practice (Guerra *et al.*, 2015). One of the approach to overcome this challenge is by

linearizing the system in a certain state subspace in order to apply the linear observability theorem (Laroche *et al.*, 2008; Basic *et al.*, 2010). This approach is very localized and lacks the sense of observability in the entirety of the state trajectories. Moreover, the construction of a global observer which converges every trajectory is impossible as the nonlinear system attempts many singular cases on the go. The local observability is a powerful concept which can be applied to any nonlinear systems (Guerra *et al.*, 2015). The concept distinguishes states only from their neighbors. The theory proposed by Hermann and Krener with the help of Lie-theoretic characterization is one of the most widely used methods for nonlinear local observability (Hermann and Krener, 1977) which is employed in this thesis. The theory shows that the rank criteria is sufficient to verify the local observability of a nonlinear system.

Local Nonlinear Observability

The local observability concept proposed by Hermann and Krener for nonlinear dynamic systems is briefly discussed (Hermann and Krener, 1977). If a system Σ is locally observable at initial state x_0, then in every open neighborhood U of x_0 is distinguishable,

$$I_U(x_0) = \{x_0\} \tag{4.2}$$

and therefore Σ is locally observable if $I_U(x) = \{x\}$ for all $x \in M$ (M is an universal set). The function $I(x_0)$ represents the set of all the points which are indistinguishable from x_0 for any admissible input. By $I(x_0) = \{x_0\}$, it means x_0 is distinguishable from all other points in x. By definition of $I_U(x) = \{x\}$, the observability of x in U is guaranteed and therefore local observability is a stronger property than the observability. On the other hand, a weaker version of the concept of observability is

defined such that for any neighborhood W of x_0

$$I(x_0) \cap W = \{x_0\} \tag{4.3}$$

and therefore Σ is weakly observable at x_0 and so for every $x \in M$. Sometimes, it is necessary to travel far in U to obtain $I(x_0) \cap W = \{x_0\}$, and consequently the concept of weakly locally observability is introduced. For any neighborhood W of x_0, there exist a neighborhood contained in W where x_0 is distinguishable i.e.

$$I_V(x_0) = \{x_0\} \quad V \subset W \tag{4.4}$$

or in other words, weakly locally observable at x_0 and therefore for every $x \in M$. The graphical interpretation of the global, local, weak and weakly locally observability concepts are provided in Fig. 4.1.

The benefit of weakly locally observability is that it can be verified by a simple algebraic test. The test is based on the rank of $\mathcal{O}$, Jacobian of the Lie derivative vectors.

$$\mathcal{O} = \frac{\partial}{\partial \mathbf{x}} \begin{pmatrix} L_f^0 \mathbf{h} \\ L_f^1 \mathbf{h} \\ .. \\ L_f^{(n-1)} \mathbf{h} \end{pmatrix} \tag{4.5}$$

where $L_f^{(n-1)}\mathbf{h}$ is the Lie derivative of the output vector $\mathbf{h}$ with respect to the system function f, and n is the dimension of state vector $\mathbf{x}$. The size of $\mathcal{O}$ is $n \times n$. If the rank of $\mathcal{O}$ is n, then the system is fully observable (locally weakly). It is laborious to analyze the rank of a large matrix like $\mathcal{O}$ at different condition of the states, and the

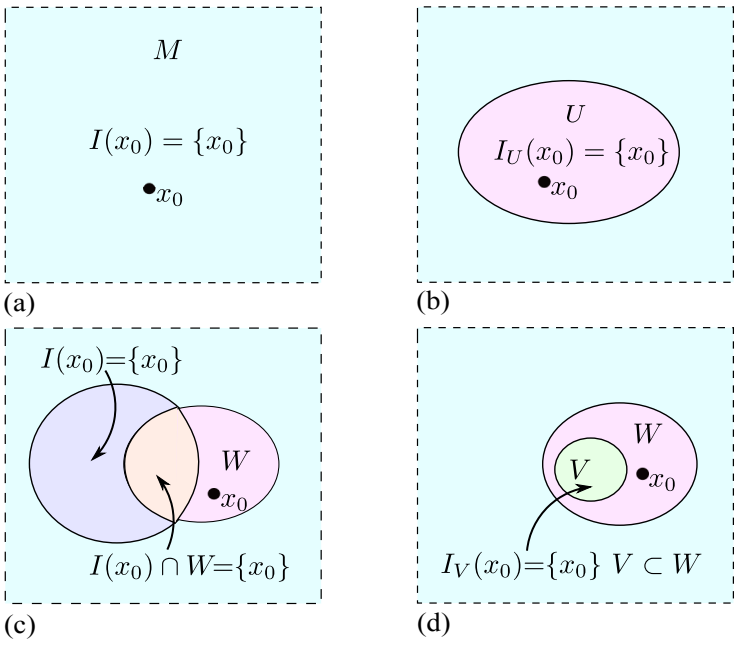

Figure 4.1: (a) Global observability, (b) local observability, (c) weak observability, and (d) weakly locally observability.

general practice is to choose a proper sub matrix.

4.3 IPMSM Nonlinear Observability

The parameters vary in different degrees in an electric machine. However, a slow variation is assumed for all the parameters in this thesis for the sake of simplicity in the mathematical formulation (Boileau *et al.*, 2011). It should be noted that, if a slow variation is observable, then it is most likely observable for the fast variation. The electrical parameters of IMPSM consists of L_d, L_q, R, and ψ_m as defined in section 2.3. The IPMSM model in dq frame does not contain position information, and therefore, in order to analyze the observability of the position, the model has to be in either $\alpha\beta$ or $\delta\gamma$ frames. The $\delta\gamma$ is chosen in this thesis however it is worthwhile note that

both the treatments are equivalent and results in similar observability conditions. In $\delta\gamma$ frame, the estimated speed $\hat{\omega}$ and angular difference $\hat{\vartheta}$ between dq and $\delta\gamma$ are the corresponding mechanical states. However, these states are considered as the parameters with slow variations as similar to the machine parameters. The system of equations of an IPMSM considering slowly varying parameters in $\delta\gamma$ frame is expressed as

$$\begin{cases} \dot{\mathbf{i}}_{\delta\gamma} = \mathbf{L}_{\delta\gamma}^{-1}\left(\mathbf{v}_{\delta\gamma} - R\hat{\mathbf{i}}_{\delta\gamma} - \hat{\omega}\mathbf{T}_r\mathbf{L}_{\delta\gamma}\hat{\mathbf{i}}_{\delta\gamma} - \hat{\omega}\psi_{\delta\gamma}\right) \\ \frac{dL_d}{dt} \cong 0 \\ \frac{dL_q}{dt} \cong 0 \\ \frac{dR}{dt} \cong 0 \\ \frac{d\psi_m}{dt} \cong 0 \\ \frac{d\hat{\vartheta}}{dt} \cong 0 \\ \frac{d\hat{\omega}}{dt} \cong 0 \end{cases} \tag{4.6}$$

In order to analyze the observability of the above nonlinear system, the local observability concept as mentioned in section 4.2.1 is applied. The state including parameters and output vectors are defined for the observability analysis (Vaclavek *et al.*, 2013) as

$$\begin{cases} \mathbf{x} = [i_\delta, i_\gamma, L_d, L_q, R, \psi_m, \hat{\vartheta}, \hat{\omega}]' \\ \mathbf{h} = [i_\delta, i_\gamma]' \end{cases} \tag{4.7}$$

The first step in observability analysis is to find the Jacobian matrix $\mathcal{O}$ given in (4.5). A detailed formulation of the Lie derivatives and Jacobian matrix for estimation

of electric machine parameters is given in (Zaltni D.a Abdelkrim *et al.*, 2009; Vaclavek *et al.*, 2013). The resulting $\mathcal{O}$ for (4.6) is a 8×8 matrix as the state vector has eight elements. The rows from top to bottom correspond to the time derivatives of the output vector from zero to third orders $(i_\delta, i_\gamma, \dot{i}_\delta, \dot{i}_\gamma, \ddot{i}_\delta, \ddot{i}_\gamma, \dddot{i}_\delta, \dddot{i}_\gamma)$ respectively and the columns from left to right represent the differentials of the output vector and its derivatives with respect to state vector $\mathbf{x}$. More precisely,

$$\mathcal{O} = \begin{bmatrix} \frac{di_\delta}{di_\delta} & \frac{di_\delta}{di_\gamma} & \frac{di_\delta}{dL_d} & \frac{di_\delta}{dL_q} & \frac{di_\delta}{dR} & \frac{di_\delta}{d\psi_m} & \frac{di_\delta}{d\hat{\vartheta}} & \frac{di_\delta}{d\hat{\omega}} \\ \frac{di_\gamma}{di_\delta} & \frac{di_\gamma}{di_\gamma} & \frac{di_\gamma}{dL_d} & \frac{di_\gamma}{dL_q} & \frac{di_\gamma}{dR} & \frac{di_\gamma}{d\psi_m} & \frac{di_\gamma}{d\hat{\vartheta}} & \frac{di_\gamma}{d\hat{\omega}} \\ \frac{d\dot{i}_\delta}{di_\delta} & \frac{d\dot{i}_\delta}{di_\gamma} & \frac{d\dot{i}_\delta}{dL_d} & \frac{d\dot{i}_\delta}{dL_q} & \frac{d\dot{i}_\delta}{dR} & \frac{d\dot{i}_\delta}{d\psi_m} & \frac{d\dot{i}_\delta}{d\hat{\vartheta}} & \frac{d\dot{i}_\delta}{d\hat{\omega}} \\ \frac{d\dot{i}_\gamma}{di_\delta} & \frac{d\dot{i}_\gamma}{di_\gamma} & \frac{d\dot{i}\gamma}{dL_d} & \frac{d\dot{i}_\gamma}{dL_q} & \frac{d\dot{i}_\gamma}{dR} & \frac{d\dot{i}_\gamma}{d\psi_m} & \frac{d\dot{i}_\gamma}{d\hat{\vartheta}} & \frac{d\dot{i}_\gamma}{d\hat{\omega}} \\ \frac{d\ddot{i}_\delta}{di_\delta} & \frac{d\ddot{i}_\delta}{di_\gamma} & \frac{d\ddot{i}_\delta}{dL_d} & \frac{d\ddot{i}_\delta}{dL_q} & \frac{d\ddot{i}_\delta}{dR} & \frac{d\ddot{i}_\delta}{d\psi_m} & \frac{d\ddot{i}_\delta}{d\hat{\vartheta}} & \frac{d\ddot{i}_\delta}{d\hat{\omega}} \\ \frac{d\ddot{i}_\gamma}{di_\delta} & \frac{d\ddot{i}_\gamma}{di_\gamma} & \frac{d\ddot{i}\gamma}{dL_d} & \frac{d\ddot{i}_\gamma}{dL_q} & \frac{d\ddot{i}_\gamma}{dR} & \frac{d\ddot{i}_\gamma}{d\psi_m} & \frac{d\ddot{i}_\gamma}{d\hat{\vartheta}} & \frac{d\ddot{i}_\gamma}{d\hat{\omega}} \\ \frac{d\dddot{i}_\delta}{di_\delta} & \frac{d\dddot{i}_\delta}{di_\gamma} & \frac{d\dddot{i}_\delta}{dL_d} & \frac{d\dddot{i}_\delta}{dL_q} & \frac{d\dddot{i}_\delta}{dR} & \frac{d\dddot{i}_\delta}{d\psi_m} & \frac{d\dddot{i}_\delta}{d\hat{\vartheta}} & \frac{d\dddot{i}_\delta}{d\hat{\omega}} \\ \frac{d\dddot{i}_\gamma}{di_\delta} & \frac{d\dddot{i}_\gamma}{di_\gamma} & \frac{d\dddot{i}\gamma}{dL_d} & \frac{d\dddot{i}_\gamma}{dL_q} & \frac{d\dddot{i}_\gamma}{dR} & \frac{d\dddot{i}_\gamma}{d\psi_m} & \frac{d\dddot{i}_\gamma}{d\hat{\vartheta}} & \frac{d\dddot{i}_\gamma}{d\hat{\omega}} \end{bmatrix} \tag{4.8}$$

The rank requirement for $\mathcal{O}$ is eight for the system to be fully observable. However, as i_δ and i_γ are measurements and always observable, the first and second columns corresponding i_δ and i_γ differentials can be ignored in $\mathcal{O}$ to conduct the parameter observability analysis. Hence the rank requirement for the system to observe all the parameters $[L_d, L_q, R, \psi_m, \hat{\vartheta}, \hat{\omega}]'$ reduces to six (the number of estimating parameters). The proper sub-matrix having rank six corresponding to $[L_d, L_q, R, \psi_m, \hat{\vartheta}, \hat{\omega}]'$ located at the bottom corner of $\mathcal{O}$, and it is expressed after rigorous mathematical deductions

as

$$\mathscr{O}_1 = \begin{bmatrix} -\dot{i}_\delta, & \hat{\omega} i_\gamma, & -i_\delta, & 0, & L_\Delta(-2\dot{i}_\gamma + \hat{\omega} i_\delta) + \psi_m \hat{\omega}, & L_q i_\gamma \\ -\hat{\omega} i_\delta, & -\dot{i}_\gamma, & -i_\gamma, & -\hat{\omega}, & -L_\Delta(2\dot{i}_\delta + \hat{\omega} i_\gamma), & -L_d i_\delta - \psi_m \\ -\ddot{i}_\delta + \xi_{1,1}, & \hat{\omega}\dot{i}_\gamma + \xi_{1,2}, & -\dot{i}_\delta + \xi_{1,3}, & \xi_{1,4}, & L_\Delta(-2\ddot{i}_\gamma + \hat{\omega}\dot{i}_\delta) + \xi_{1,5}, & L_q \dot{i}_\gamma + \xi_{1,6} \\ -\hat{\omega}\dot{i}_\delta + \xi_{2,1}, & -\ddot{i}_\gamma + \xi_{2,2}, & -\dot{i}_\gamma + \xi_{2,3} & \xi_{2,4}, & L_\Delta(-2\ddot{i}_\delta + \hat{\omega}\dot{i}_\gamma) + \xi_{2,5}, & -L_d \dot{i}_\delta + \xi_{2,6} \\ -\dddot{i}_\delta + \xi_{3,1}, & \hat{\omega}\ddot{i}_\gamma + \xi_{3,2}, & -\ddot{i}_\delta + \xi_{3,3}, & \xi_{3,4}, & L_\Delta(-2\dddot{i}_\gamma + \hat{\omega}\ddot{i}_\delta) + \xi_{3,5}, & L_q \ddot{i}_\gamma + \xi_{3,6} \\ -\hat{\omega}\ddot{i}_\delta + \xi_{4,1}, & -\dddot{i}_\gamma + \xi_{4,2}, & -\ddot{i}_\gamma + \xi_{4,3}, & \xi_{4,4}, & L_\Delta(-2\dddot{i}_\delta + \hat{\omega}\ddot{i}_\gamma) + \xi_{4,5}, & -L_d \ddot{i}_\delta + \xi_{4,6} \end{bmatrix} \tag{4.9}$$

where

$$\begin{cases} \xi_{i,j} = -R\mathscr{o}_{i,j} + L_q \hat{\omega} \mathscr{o}_{i+1,1} & \text{for } i = \{1,3\}, \text{ and } j = \{1,2,3,4,5,6\} \\ \xi_{i,j} = -R\mathscr{o}_{i,j} - L_d \hat{\omega} \mathscr{o}_{i-1,1} & \text{for } i = \{2,4\}, \text{ and } j = \{1,2,3,4,5,6\} \end{cases}$$

and $\mathscr{o}_{i,j}$ is an element in $\mathscr{O}$ corresponding to i^{th} row and j^{th} column. In $\mathscr{O}_1$, it is set that $\hat{\vartheta} \approx 0$. If $\hat{\vartheta} >> 0$, sine and cosine terms appear in $\mathscr{O}_1$ and the equation becomes too large to express. If the system is observable at $\hat{\vartheta} \approx 0$, then it is observable for $\hat{\vartheta} >> 0$ as well. The sub-matrix $\mathscr{O}_1$ provides the necessary observability conditions and persistent excitation requirements for identifying each parameter and their combinations.

4.3.1 Single Parameter Identification

The observability condition for a single parameter identification is very straightforward and well known. A parameter is observable (or identifiable) if at least a non zero element in the corresponding column of $\mathscr{O}_1$ exists. The first column corresponds to L_d,

and the subsequent columns belong to L_q, R, ψ_m, $\hat{\vartheta}$, and $\hat{\omega}$ in the order. For identifying L_d, either $|\dot{i}_\delta|+|\ddot{i}_\delta|+|\dddot{i}_\delta|\neq 0$ or $i_\delta\hat{\omega}\neq 0$, and similarly either $|\dot{i}_\gamma|+|\ddot{i}_\gamma|+|\dddot{i}_\gamma|\neq 0$ or $i_\gamma\hat{\omega}\neq 0$ for identifying L_q. Either of the current (i_δ or i_γ) or any of their derivatives must be nonzero for identifying R. Only a single condition exists for identifying ψ_m i.e. $\hat{\omega}\neq 0$. For identifying $\hat{\vartheta}$ at $\hat{\omega}=0$, the machine must be salient ($L_\Delta\neq 0$) and also at least the first order derivatives of either i_δ or i_γ must be nonzero according to column five in $\mathcal{O}_1$. To identify $\hat{\omega}$, either i_δ or i_γ or any of their derivative must be non zero if $\psi_m=0$ (i.e. non permanent magnet machines). The summary of the observability conditions for a single parameter identification is provided in Table 4.1. The identifiable single parameters at different operating states is provided in Table 4.2.

Table 4.1: Summary of Observability Conditions for Single Parameter Identification

Parameters	Conditions
L_d	$\|\dot{i}_\delta\|+\|\ddot{i}_\delta\|+\|\dddot{i}_\delta\|\neq 0$ or $i_\delta\hat{\omega}\neq 0$
L_q	$\|\dot{i}_\gamma\|+\|\ddot{i}_\gamma\|+\|\dddot{i}_\gamma\|\neq 0$ or $i_\gamma\hat{\omega}\neq 0$
R	$\|\mathbf{i}_{\delta\gamma}\|+\|\dot{\mathbf{i}}_{\delta\gamma}\|+\|\ddot{\mathbf{i}}_{\delta\gamma}\|+\|\dddot{\mathbf{i}}_{\delta\gamma}\|\neq 0$
ψ_m	$\hat{\omega}\neq 0$
$\hat{\vartheta}$	$L_\Delta\neq 0$, and $\|\mathbf{i}_{\delta\gamma}\|+\|\dot{\mathbf{i}}_{\delta\gamma}\|+\|\ddot{\mathbf{i}}_{\delta\gamma}\|+\|\dddot{\mathbf{i}}_{\delta\gamma}\|\neq 0$ if $\hat{\omega}=0$, or $\hat{\omega}\neq 0$
$\hat{\omega}$	$\|\mathbf{i}_{\delta\gamma}\|+\|\dot{\mathbf{i}}_{\delta\gamma}\|+\|\ddot{\mathbf{i}}_{\delta\gamma}\|+\|\dddot{\mathbf{i}}_{\delta\gamma}\|\neq 0$ if $\psi_m=0$, or $\psi_m\neq 0$

The persistent excitation (PE) for an electric machine is the input voltage producing the required current excitation which enables the identification of the different parameters. The constant current excitation is sufficient to identify the parameters at $\hat{\omega}\neq 0$. For $\hat{\omega}=0$ and/or $\psi_m=0$, at least the first order derivatives of the currents must be nonzero. This is true at the transient operation of the machine, however, at steady state, a high frequency signal (persistent excitation) is generally injected to

Table 4.2: Identifiable single parameters at different operating states

Operating conditions	Possible parameters
SS, & $\hat{w} \neq 0$	$\not{p} = \{\{L_d\}, \{L_q\}, \{R\}, \{\psi_m\}, \{\hat{\vartheta}\}, \{\hat{\omega}\}\}$
SS, $\hat{w} \neq 0$, & $i_\delta = 0$	$\not{p} - \{L_d\}$
SS, $\hat{w} = 0$, &/ $i_\delta = 0$	$\{R\}, \{\hat{\omega}\}$
FTS, & $\hat{w} \neq 0$,	$\not{p}$
FTS, $\hat{w} \neq 0$, & $i_\delta = 0$	$\not{p}$
FTS, $\hat{w} = 0$, &/ $i_\delta = 0$	$\not{p} - \{\psi_m\}$
STS, & $\hat{w} \neq 0$,	$\not{p}$
STS, $\hat{w} \neq 0$, & $i_\delta = 0$	$\not{p}$
STS, $\hat{w} = 0$, &/ $i_\delta = 0$	$\not{p} - \{\psi_m\}$

SS- steady state ($|\dot{\mathbf{i}}_{\delta\gamma}|+|\ddot{\mathbf{i}}_{\delta\gamma}|+|\dddot{\mathbf{i}}_{\delta\gamma}|= 0$), FTS-first order transient state ($|\dot{i}_\delta|+|\dot{i}_\gamma|\neq 0$)
STS-second order transient state ($|\dot{i}_\delta|+|\dot{i}_\gamma|+|\ddot{i}_\delta + \ddot{i}_\gamma|\neq 0$), $\not{p} = \{\{L_d\}, \{L_q\}, \{R\}, \{\psi_m\}, \{\hat{\vartheta}\}, \{\hat{\omega}\}\}$

create a quasi transient state.

4.3.2 Multi-Parameter Identification

In multi-parameter identification, the different parameters are identified simultaneously. The observability of a combination of the parameters is tested against the rank of the corresponding proper sub-matrix in $\mathcal{O}_1$. The rank of the proper sub-matrix must be equal to the number of parameters in a combination in order to identify these parameters simultaneously. For example, a proper sub-matrix should be selected from first and second columns of $\mathcal{O}_1$ and the rank must be two in order to simultaneously identify L_d and L_q. Or in other words, the first and two columns must be linearly independent.

The worst operating condition with respect to parameter identification is the steady state (SS) defined as $|\dot{\mathbf{i}}_{\delta\gamma}|+|\ddot{\mathbf{i}}_{\delta\gamma}|+|\dddot{\mathbf{i}}_{\delta\gamma}|= 0$. At SS and $\hat{\omega} \neq 0$, the combinations of two and three parameter sets are identifiable except $\{L_d, \psi_m\}$ and $\{R, \hat{\vartheta}, \hat{\omega}\}$. The

columns belong to these unidentifiable sets are linearly independent. The combinations of more than three parameters are not possible as the rank of $\mathcal{O}_1$ is three at this operating state. At SS and $i_\delta = 0$, the combination with sets $\{L_d\}$, $\{R, \psi_m\}$, and $\{R, \hat{\vartheta}, \hat{\omega}\}$ are not identifiable. Moreover, the maximum number of parameters simultaneously identifiable are three. The only simultaneously identifiable parameter set at SS and $\hat{\omega} = 0$ is $\{R, \hat{\omega}\}$.

The first order transient state (FTS) is defined as $[|\dot{i}_\delta|, |\dot{i}_\gamma|]' \neq \mathbf{0}$ where $\mathbf{0}$ is a zero vector with appropriate dimension. The identifiability of the parameters significantly improves at this operating state. At FTS, $\hat{\omega} \neq 0$ and/or $i_\delta = 0$, all the combinations of two to five parameters are identifiable except $\{L_d, R, \psi_m, \hat{\vartheta}, \hat{\omega}\}$. The six parameter combination is identifiable only when there is a second order transient state (STS $\triangleq [|\dot{i}_\delta|, |\dot{i}_\gamma|, |\ddot{i}_\delta|, |\ddot{i}_\gamma|]' \neq \mathbf{0}$) in the system. At $\hat{\omega} = 0$ and/or $i_\delta = 0$, all the two to five parameter combinations except the sets with $\{\psi_m\}$ are identifiable for both FTS and STS operating states. The identifiable combinations for two to six parameter sets are summarized in Tables 4.3, 4.4, 4.5, 4.6, and 4.7 respectively.

The PE requirements for the simultaneous multi-parameter identification vary with respect to operating states as presented in this section. The voltage input (a PE) producing constant currents (case of SS) is not sufficient to identify the combination sets with more than three parameters. The worst case scenario is when $\hat{\omega} = 0$ where only parameter set $\{R, \hat{\omega}\}$ is identifiable. The PE should produce currents with at least nonzero first order derivatives in order to identify higher number of parameters. For identifying all the six parameters, either of the second order current derivatives ($\ddot{i}_\delta$ or $\ddot{i}_\gamma$) should be nonzero. The values of current derivatives should be sufficient enough to enable good identification of the parameters. A typical PE input is high frequency

Table 4.3: Identifiable two parameter combinations at different operating states

Operating condition	Possible parameter sets
SS, & $\hat{w} \neq 0$	${}^{6}_{2}C(\boldsymbol{\rho}) - \{L_d, \psi_m\}$
SS, $\hat{w} \neq 0$, & $i_\delta = 0$	${}^{6}_{2}C(\boldsymbol{\rho} - \{L_d\}) - \{R, \psi_m\}$
SS, $\hat{w} = 0$, &/ $i_\delta = 0$	$\{R, \hat{\omega}\}$
FTS, & $\hat{w} \neq 0$	${}^{6}_{2}C(\boldsymbol{\rho})$
FTS, $\hat{w} \neq 0$,& $i_\delta = 0$	${}^{6}_{2}C(\boldsymbol{\rho})$
FTS, $\hat{w} = 0$, &/ $i_\delta = 0$	${}^{6}_{2}C(\boldsymbol{\rho} - \{\psi_m\})$
STS, & $\hat{w} \neq 0$	${}^{6}_{2}C(\boldsymbol{\rho})$
STS, $\hat{w} \neq 0$, & $i_\delta = 0$	${}^{6}_{2}C(\boldsymbol{\rho})$
STS, $\hat{w} = 0$, &/ $i_\delta = 0$	${}^{6}_{2}C(\boldsymbol{\rho} - \{\psi_m\})$

SS- steady state ($|\dot{\mathbf{i}}_{\delta\gamma}|+|\ddot{\mathbf{i}}_{\delta\gamma}|+|\ddot{\mathbf{i}}_{\delta\gamma}|= 0$), FTS-first order transient state ($[|\dot{i}_\delta|, |\dot{i}_\gamma|]' \neq \mathbf{0}$)
STS-second order transient state ($[|\dot{i}_\delta|, |\dot{i}_\gamma|, |\ddot{i}_\delta, \ddot{i}_\gamma|]' \neq \mathbf{0}$),$\boldsymbol{\rho} = \{\{L_d\}, \{L_q\}, \{R\}, \{\psi_m\}, \{\hat{\vartheta}\}, \{\hat{\omega}\}\}$

Table 4.4: Identifiable three parameter combinations at different operating states

Operating condition	Possible parameter sets
SS, & $\hat{w} \neq 0$	${}^{6}_{3}C(\boldsymbol{\rho}) - {}^{6}_{2}C(\{\{L_d, \psi_m\}, L_q, R, \hat{\vartheta}, \hat{\omega}\}) - \{R, \hat{\vartheta}, \hat{\omega}\}$
SS, $\hat{w} \neq 0$, & $i_\delta = 0$	${}^{6}_{3}C(\boldsymbol{\rho} - \{L_d\}) - {}^{6}_{2}C(\{\{R, \psi_m\}, L_q, \hat{\vartheta}, \hat{\omega}\}) - \{R, \hat{\vartheta}, \hat{\omega}\}$
SS, $\hat{w} = 0$, &/ $i_\delta = 0$	Nil
FTS, & $\hat{w} \neq 0$	${}^{6}_{3}C(\boldsymbol{\rho})$
FTS, $\hat{w} \neq 0$,& $i_\delta = 0$	${}^{6}_{3}C(\boldsymbol{\rho})$
FTS, $\hat{w} = 0$, &/ $i_\delta = 0$	${}^{6}_{3}C(\boldsymbol{\rho} - \{\psi_m\})$
STS, & $\hat{w} \neq 0$	${}^{6}_{3}C(\boldsymbol{\rho})$
STS, $\hat{w} \neq 0$, & $i_\delta = 0$	${}^{6}_{3}C(\boldsymbol{\rho})$
STS, $\hat{w} = 0$, &/ $i_\delta = 0$	${}^{6}_{3}C(\boldsymbol{\rho} - \{\psi_m\})$

SS- steady state ($|\dot{\mathbf{i}}_{\delta\gamma}|+|\ddot{\mathbf{i}}_{\delta\gamma}|+|\ddot{\mathbf{i}}_{\delta\gamma}|= 0$), FTS-first order transient state ($[|\dot{i}_\delta|, |\dot{i}_\gamma|]' \neq \mathbf{0}$)
STS-second order transient state ($[|\dot{i}_\delta|, |\dot{i}_\gamma|, |\ddot{i}_\delta, \ddot{i}_\gamma|]' \neq \mathbf{0}$),$\boldsymbol{\rho} = \{\{L_d\}, \{L_q\}, \{R\}, \{\psi_m\}, \{\hat{\vartheta}\}, \{\hat{\omega}\}\}$

sinusoidal injection and its response is continuously differentiable at any order and the magnitude multiplies with the order of the differentiation ($\frac{d^n \sin(\omega_h t)}{dt^n} = \omega_h^n \sin(\omega_h t)$, where ω_h is frequency of injection). The non-sinusoidal injections like square, pulse or vector would also realize PE however the second derivative of the response current

Table 4.5: Identifiable four parameter combinations at different operating states

Operating condition	Possible parameter sets
SS, & $\hat{w} \neq 0$	Nil
SS, $\hat{w} \neq 0$, & $i_\delta = 0$	Nil
SS, $\hat{w} = 0$, &/ $i_\delta = 0$	Nil
FTS, & $\hat{w} \neq 0$	${}^6_4C(\boldsymbol{\rho})$
FTS, $\hat{w} \neq 0$,& $i_\delta = 0$	${}^6_4C(\boldsymbol{\rho})$
FTS, $\hat{w} = 0$, &/ $i_\delta = 0$	${}^6_4C(\boldsymbol{\rho} - \{\psi_m\})$
STS, & $\hat{w} \neq 0$	${}^6_4C(\boldsymbol{\rho})$
STS, $\hat{w} \neq 0$, & $i_\delta = 0$	${}^6_4C(\boldsymbol{\rho})$
STS, $\hat{w} = 0$, &/ $i_\delta = 0$	${}^6_4C(\boldsymbol{\rho} - \{\psi_m\})$

SS- steady state ($|\dot{\mathbf{i}}_{\delta\gamma}|+|\ddot{\mathbf{i}}_{\delta\gamma}|+|\dddot{\mathbf{i}}_{\delta\gamma}| = 0$), FTS-first order transient state ($[|\dot{i}_\delta|, |i_\gamma|]' \neq \mathbf{0}$)
STS-second order transient state ($[|\dot{i}_\delta|, |\dot{i}_\gamma|, |\ddot{i}_\delta, \ddot{i}_\gamma|]' \neq \mathbf{0}$),$\boldsymbol{\rho} = \{\{L_d\}, \{L_q\}, \{R\}, \{\psi_m\}, \{\hat{\vartheta}\}, \{\hat{\omega}\}\}$

Table 4.6: Identifiable five parameter combinations at different operating states

Operating condition	Possible parameter sets
SS, & $\hat{w} \neq 0$	Nil
SS, $\hat{w} \neq 0$, & $i_\delta = 0$	Nil
SS, $\hat{w} = 0$, &/ $i_\delta = 0$	Nil
FTS, & $\hat{w} \neq 0$	${}^6_5C(\boldsymbol{\rho}) - \{L_d, R, \psi_m, \hat{\vartheta}, \hat{\omega}\}$
FTS, $\hat{w} \neq 0$,& $i_\delta = 0$	${}^6_5C(\boldsymbol{\rho}) - \{L_d, R, \psi_m, \hat{\vartheta}, \hat{\omega}\}$
FTS, $\hat{w} = 0$, &/ $i_\delta = 0$	${}^6_5C(\boldsymbol{\rho} - \{\psi_m\})$
STS, & $\hat{w} \neq 0$	${}^6_5C(\boldsymbol{\rho})$
STS, $\hat{w} \neq 0$, & $i_\delta = 0$	${}^6_5C(\boldsymbol{\rho})$
STS, $\hat{w} = 0$, &/ $i_\delta = 0$	${}^6_5C(\boldsymbol{\rho} - \{\psi_m\})$

SS- steady state ($|\dot{\mathbf{i}}_{\delta\gamma}|+|\ddot{\mathbf{i}}_{\delta\gamma}|+|\dddot{\mathbf{i}}_{\delta\gamma}| = 0$), FTS-first order transient state ($[|\dot{i}_\delta|, |i_\gamma|]' \neq \mathbf{0}$)
STS-second order transient state ($[|\dot{i}_\delta|, |\dot{i}_\gamma|, |\ddot{i}_\delta, \ddot{i}_\gamma|]' \neq \mathbf{0}$),$\boldsymbol{\rho} = \{\{L_d\}, \{L_q\}, \{R\}, \{\psi_m\}, \{\hat{\vartheta}\}, \{\hat{\omega}\}\}$

should have sufficient magnitude if intended to identify all the six parameters. The next section of this chapter discuss more about the PE by FCSMPC enabling all the six parameter identification.

Table 4.7: Identifiable Six parameter combinations at different operating states

Operating condition	Possible parameter sets
SS, & $\hat{w} \neq 0$	Nil
SS, $\hat{w} \neq 0$, & $i_\delta = 0$	Nil
SS, $\hat{w} = 0$, &/ $i_\delta = 0$	Nil
FTS, & $\hat{w} \neq 0$	Nil
FTS, $\hat{w} \neq 0$,& $i_\delta = 0$	Nil
STS, & $\hat{w} \neq 0$	$\{L_d, L_q, R, \psi_m, \hat{\vartheta}, \hat{\omega}\}$
STS, $\hat{w} \neq 0$, & $i_\delta = 0$	$\{L_d, L_q, R, \psi_m, \hat{\vartheta}, \hat{\omega}\}$
STS, $\hat{w} = 0$, &/ $i_\delta = 0$	Nil

SS- steady state ($|\dot{\mathbf{i}}_{\delta\gamma}|+|\ddot{\mathbf{i}}_{\delta\gamma}|+|\dddot{\mathbf{i}}_{\delta\gamma}|= 0$), FTS-first order transient state ($[|\dot{i}_\delta|, |\dot{i}_\gamma|]' \neq \mathbf{0}$)
STS-second order transient state ($[|\dot{i}_\delta|, |\dot{i}_\gamma|, |\ddot{i}_\delta, \ddot{i}_\gamma|]' \neq \mathbf{0}$),$\rho = \{\{L_d\}, \{L_q\}, \{R\}, \{\psi_m\}, \{\hat{\vartheta}\}, \{\hat{\omega}\}\}$

4.4 Proposed FCSMPC

The proposed finite control set model predictive control (FCSMPC) is implemented in the estimated rotor reference frame ($\delta\gamma$) in this thesis. The position information to perform the field orientation is obtained from the estimation in this case. However, the IPMSM model in $\delta\gamma$ frame transforms to dq frame when the actual measured position is used (position error $\hat{\vartheta} = 0$). Therefore, the FCSMPC realization presented in this section in $\delta\gamma$ frame should be treated in dq frame for the case of estimating only the machine parameters with the measured position by setting $\hat{\vartheta} = 0$.

The proposed cost function to reduce the error between the reference and predicted currents is defined as,

$$f_N = \sum_{i=1}^{N} \tilde{\mathbf{i}}'_{\delta\gamma,k+i-1} \mathbf{Q}\, \tilde{\mathbf{i}}_{\delta\gamma,k+i-1} \tag{4.10}$$

where $\tilde{\mathbf{i}}_{\delta\gamma,k+i-1}$ is the error between the reference $\mathbf{i}^*_{\delta\gamma,k+i-1}$ and predicted $\hat{\mathbf{i}}_{\delta\gamma,k+i-1}$ currents

$$\tilde{\mathbf{i}}_{\delta\gamma,k+i-1} = \mathbf{i}^*_{\delta\gamma,k} - \hat{\mathbf{i}}_{\delta\gamma,k+i-1}, \tag{4.11}$$

and $\mathbf{Q} = [[1,0]', [0,1]']$. The cost function is kept simple in this thesis by not penalizing the control action and also by keeping $N = 1$ as the main focus of this thesis is estimation of parameters and position and not on the performance of the FCSMPC. The cost (4.10) is optimized with respect $\mathbf{v}_{\delta\gamma}$ subject to the following constraints

$$\begin{cases} \hat{\mathbf{i}}_{\delta\gamma,k} \in \mathbf{I}_{\delta\gamma} \subset \mathbb{R}^2 \\ \hat{\mathbf{i}}_{\delta\gamma,k+1} = \mathbf{L}_{\delta\gamma}^{-1}\left(\mathbf{v}_{\delta\gamma} - R\hat{\mathbf{i}}_{\delta\gamma,k} - \omega\mathbf{T}_r\mathbf{L}_{\delta\gamma}\hat{\mathbf{i}}_{\delta\gamma,k} - \omega\psi_{\delta\gamma}\right) \quad \text{from (2.13)} \\ \mathbf{v}_{\delta\gamma} = \mathbf{T}_{\delta\gamma}\mathbf{T}_{dq}\mathbf{T}_{\alpha\beta}\mathbf{v}_{abc},\ \mathbf{v}_{abc} \in \mathbf{V}_{abc} \end{cases} \tag{4.12}$$

where $\mathbf{V}_{abc}$ is a finite set consisting of the voltage vectors $(\mathbf{v}_0, \mathbf{v}_1, ...\mathbf{v}_7)$ corresponding to eight switching states $\mathbf{s} \in \mathcal{S} = \{0,1\}^3$ of a two level inverter

$$\begin{cases} s_0 = [0,0,0] & s_4 = [0,1,1] \\ s_1 = [1,0,0] & s_5 = [0,0,1] \\ s_2 = [1,1,0] & s_6 = [1,0,1] \\ s_3 = [0,1,0] & s_7 = [1,1,1] \end{cases} \tag{4.13}$$

The first and last switching states (s_0 and s_7) produce the null (or zero) vectors and other six states produce the active vectors. A null vector is applied when there is no control action is required or when the control feedback meets the requirements. By applying the active switching states to a two level inverter the different voltage vectors are produced. For example, by applying state s_1, the upper switch of a-phase and bottom switches of b and c phases are closed as shown in Fig. 4.2 (a). The corresponding voltage phasors are shown in Fig. 4.2 (b). The voltage vector $\mathbf{v}_1$ is found by adding each phasors $(v_a + v_b + v_c)$, and $|\mathbf{v}_1| = v_{dc}$ (v_{dc} is the dc-link voltage) and the angle is 0 rad. By applying subsequent switching states, the voltage vectors

rotates in a discrete angle step $\frac{\pi}{3}$ rad with the constant magnitude v_{dc}. Therefore, the three phase voltage vector is expressed as

$$\mathbf{v}_{abc} = v_{dc} s_n; \quad n = 0, 1, 2...7 \tag{4.14}$$

where n is the index of a switching state s as given in (4.13). The corresponding voltage in $\delta\gamma$ frame is found as

$$\mathbf{v}_{\delta\gamma} = \mathbf{T}_{\delta\gamma}\mathbf{T}_{dq}\mathbf{T}_{\alpha\beta}\mathbf{v}_{abc} \tag{4.15}$$

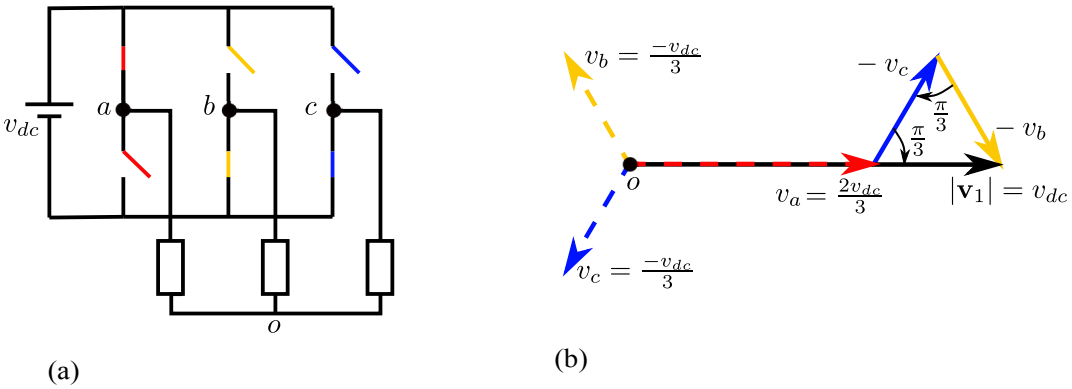

Figure 4.2: (a) Inverter switching state s_1 and (b) the production of the corresponding voltage vector $\mathbf{v}_1$.

Since the optimization variable (here voltage $\mathbf{v}_{\delta\gamma}$) belongs to a finite set and also as $N = 1$, the process of optimization of the cost function consists of only finding the minimum cost from the costs corresponding to eight switching states.

$$min(\mathbf{f}_N) = f_N^m \quad \text{where } \mathbf{f}_N = \{f_N^0, f_N^1, ...f_N^7\} \tag{4.16}$$

where $m \in \{0, 1, ..7\}$ is the index of the voltage vector producing the minimum cost, and $\mathbf{f}_N$ is the set of the costs corresponding to eight switching states. As $N = 1$, the cost function in (4.10) can also be expressed as

$$f_N = \tilde{\mathbf{i}}'_{\delta\gamma,k} \mathbf{Q} \, \tilde{\mathbf{i}}_{\delta\gamma,k} \tag{4.17}$$

and also the error between the reference and the predicted current becomes

$$\tilde{\mathbf{i}}_{\delta\gamma,k} = \mathbf{i}^*_{\delta\gamma,k} - \hat{\mathbf{i}}_{\delta\gamma,k} \tag{4.18}$$

As mentioned in the beginning of this section $\hat{\mathbf{i}}_{\delta\gamma,k}$ is the predicted current. More precisely it is the current predicted at k^{th} sample to establish at $k + 1^{th}$ sample. Therefore, (4.18) is more precisely expressed as

$$\tilde{\mathbf{i}}_{\delta\gamma,k} = \mathbf{i}^*_{\delta\gamma,k} - \hat{\mathbf{i}}_{\delta\gamma,k+1} \tag{4.19}$$

The predicted current $\hat{\mathbf{i}}_{\delta\gamma,k+1}$ is found for the voltage vectors corresponding to all the switching states $\mathbf{s}$ in order to obtain the set of the cost function $\mathbf{f}_N$.

$$\hat{\mathbf{i}}_{\delta\gamma,k+1} = \mathbf{L}^{-1}_{\delta\gamma} \left(\mathbf{v}_{\delta\gamma} - R\hat{\mathbf{i}}_{\delta\gamma,k} - \omega \mathbf{T}_r \mathbf{L}_{\delta\gamma} \hat{\mathbf{i}}_{\delta\gamma,k} - \omega \psi_{\delta\gamma} \right) \tag{4.20}$$

In (4.20), $\hat{\mathbf{i}}_{\delta\gamma,k}$ is found from the unit delay compensation to account for the time difference between the measurement and the application of the control action (Rovere *et al.*, 2016).

$$\hat{\mathbf{i}}_{\delta\gamma,k} = \mathbf{L}^{-1}_{\delta\gamma} \left(\mathbf{v}_{\delta\gamma,k} - R\mathbf{i}_{\delta\gamma,k} - \omega \mathbf{T}_r \mathbf{L}_{\delta\gamma} \mathbf{i}_{\delta\gamma,k} - \omega \psi_{\delta\gamma} \right) \quad \text{from (2.13)} \tag{4.21}$$

In (4.20), $\mathbf{v}_{\delta\gamma}$ is a variable, and in (4.21), $\mathbf{v}_{\delta\gamma,k}$ is the optimal voltage computed at $k-1^{th}$ sample and applied at k^{th} sample. The current $\mathbf{i}_{\delta\gamma,k}$ is the measurement at k^{th} sample. The timing diagram of the proposed FCSMPC is provided in Fig. 4.3 and the block diagram is depicted in Fig. 4.4.

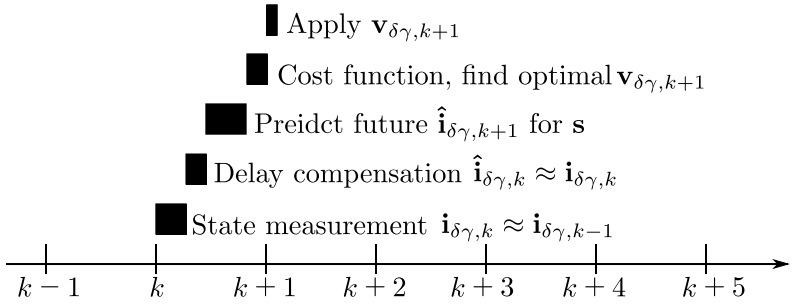

Figure 4.3: The timing diagram of the proposed FCSMPC.

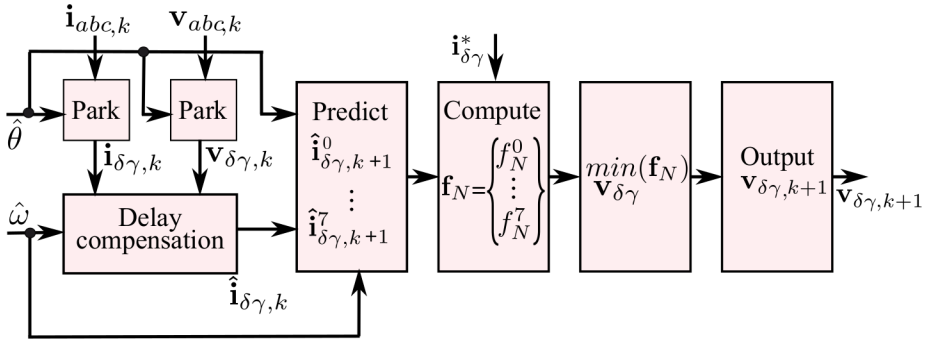

Figure 4.4: The block diagram of the proposed FCSMPC scheme.

4.5 Persistent Excitation by FCSMPC

The proposed FCSMPC applies a voltage vector corresponding to the minimum cost at a sampling interval as explained in section 4.4. The modulation schemes (e.g. SPWM, SVPWM) are not required for FCSMPC as the applied voltage vectors are

chosen from the finite set corresponding to eight switching states of a two level voltage source inverter. A voltage vector essentially applies the constant voltages as shown in Fig. 4.2 (b) to the three phase armature coils at a particular sampling interval. The level of the constant voltage remains the same for each phases until there is a requirement for changing the switching states according to the cost minimization. If there is a change in the switching state, the FCSMPC applies the corresponding voltage vector. The subsequent applications of different voltage vectors create substantial switching ripples in the current. If the first and higher order derivatives of these switching ripples are nonzero then it is true that the machine is persistently excited by the voltage vectors (according to section 4.3.2).

The rate of switching state transitions defines the switching frequency and it varies according to the operating conditions of the machine. The switching frequency at steady state is mainly dependent on the speed of the machine. It increases proportional to the speed and therefore the switching transitions do not occur at zero speed if the reference currents $\mathbf{i}^*_{\delta\gamma} = 0$. In other words FCSMPC applies null vectors. Moreover, the subsequent application of only null vectors results in no switching ripples and hence no PE. This situation is overcome by setting a small negative δ current reference at standstill in thesis. If $\mathbf{i}_{\delta\gamma} \neq 0$ at zero speed, the FCMPSC applies active vectors to maintain the reference values of the currents and results in switching ripples. The magnitude and frequency of this switching ripples are essentially dependent on the electrical time constant of the machine and hence varies from machine to machine. Therefore, it is required to verify the current responses of the machine, especially at zero speed and $\mathbf{i}_{\delta\gamma} \neq 0$ that the applied voltage vectors establish PE.

The measured current response at standstill when $\mathbf{i}_{\delta\gamma} = 0$ and $i^*_\delta = -1$ A (the

worst case) are shown in Fig. 4.5 (a) and (b) respectively. There is no switching ripples with zero reference currents and only small current measurement noise exists. Significant switching ripples are found in i_δ and i_γ when $i^*_\delta = -1$ A. The first and second order time derivatives of i_δ and i_γ are depicted in Fig. 4.6. The maximum values of the first order derivatives for i_δ and i_γ are 18 kA/s and 9kA/s respectively and for the second order derivatives are 36 kA/s^2 and 18 kA/s^2 respectively. The zoomed views of these graphs show that an average of $\pm$0.2 kA/s $\pm$0.2 kA/s^2 always exist for the first and second order derivatives except at zero crossings. Momentary non-observable situation would occur with zero crossings and potentially create ripples in online estimation of the parameters. However, these singularity issues are managed by implementing regulatory terms in the cost function as discussed in the upcoming chapters.

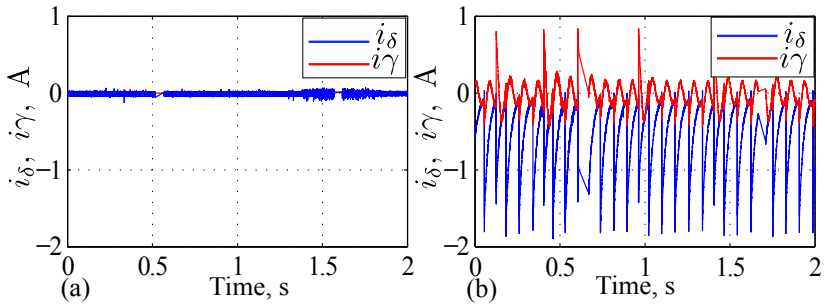

Figure 4.5: The measured $\delta\gamma$ currents at standstill: (a) $i^*_\delta = 0$ A and $i^*_\gamma = 0$ A, and (b) $i^*_\delta = -1$ A and $i^*_\gamma = 0$ A.

The zero reference current (no load) with nonzero speed is another worst case operating scenario. However, as the voltage vectors needs to be rotated according to the rotation of the machine, the switching states changes and thus generates the persistent switching ripples. The measured i_δ and i_γ at no load and 50 rpm in Fig. 4.7

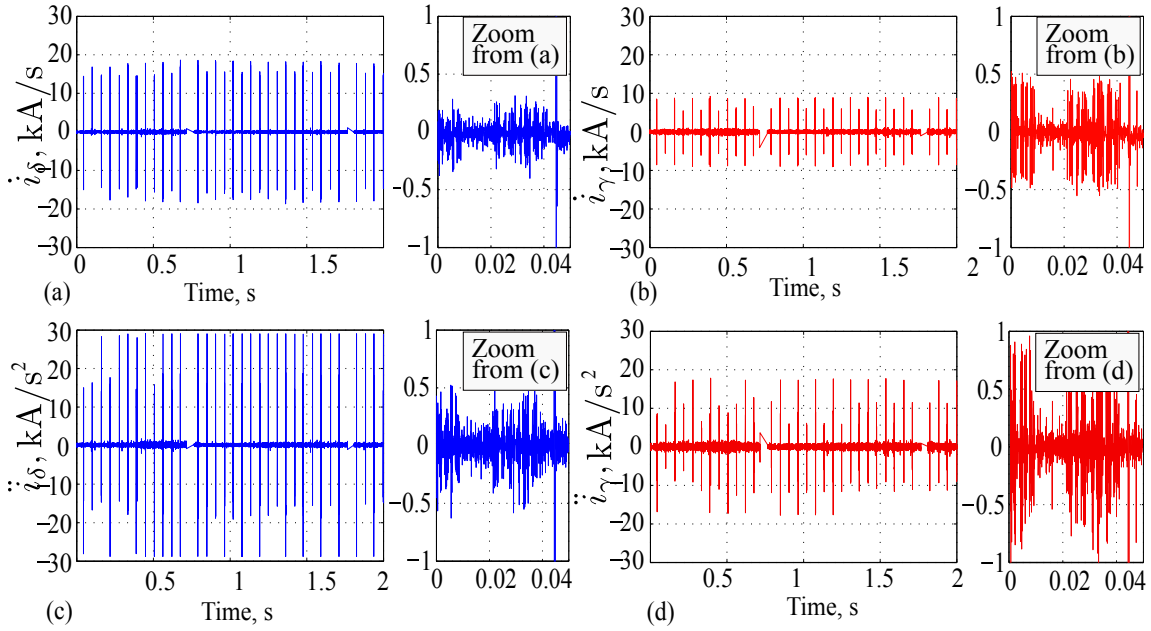

Figure 4.6: The first and second order derivatives of the measured currents at standstill, $i^*_\delta = -1$ A and $i^*_\gamma = 0$ A (a) $\dot{i}_\delta$ (b) $\dot{i}_\gamma$, (c) $\ddot{i}_\delta$, and (d) $\ddot{i}_\gamma$.

shows the persistent switching ripples. The average values for the first order derivatives of i_δ and i_γ for this case are ± 0.8 kA/s and ± 0.6 kA/s, and the corresponding values for the second order derivatives are 0.2 kA/s^2 and 0.05 kA/s^2 respectively.

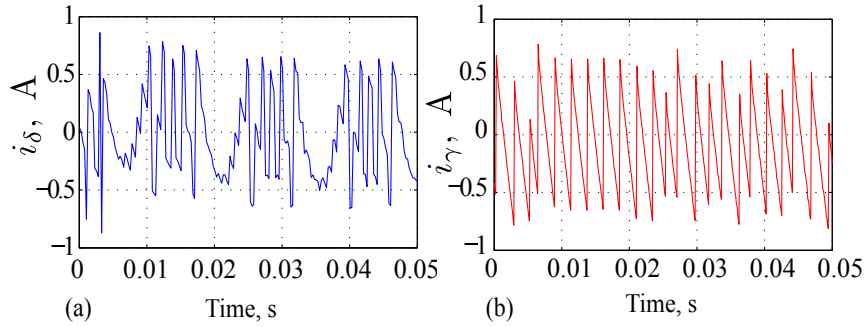

Figure 4.7: The measured currents at 50 rpm and $\mathbf{i}^*_{\delta\gamma} = 0$: (a) $i\delta$ and (b) $i\gamma$.

The transient state followed by sudden change in the torque or speed is another worst case scenario as there is a possibility of flat or linear current responses. Fig. 4.8

(a) shows the measured current response for a speed reversal at 50 rpm. The current i_δ flattens out near the zero speed and results in the average $\dot{i}_\delta$ as low as 10 A/s and $\ddot{i}_\delta = 5$ A/s^2 in this period (0.04 s - 0.055 s). For i_γ, the values of the first and second order current derivatives are better than i_δ and the corresponding average values are 50 A/s and 10 A/s^2 respectively. For the current reversal (in a sense the torque reversal) of i_γ from -10 A to 10 A (the rated current of the reference IPSMS, see Appendix B for details), the response is close to linear resulting in low average second order derivative as 5 A/s in the period 0.012 s-0.014 s . The average value of the first order derivative is 10 kA/s in this period.

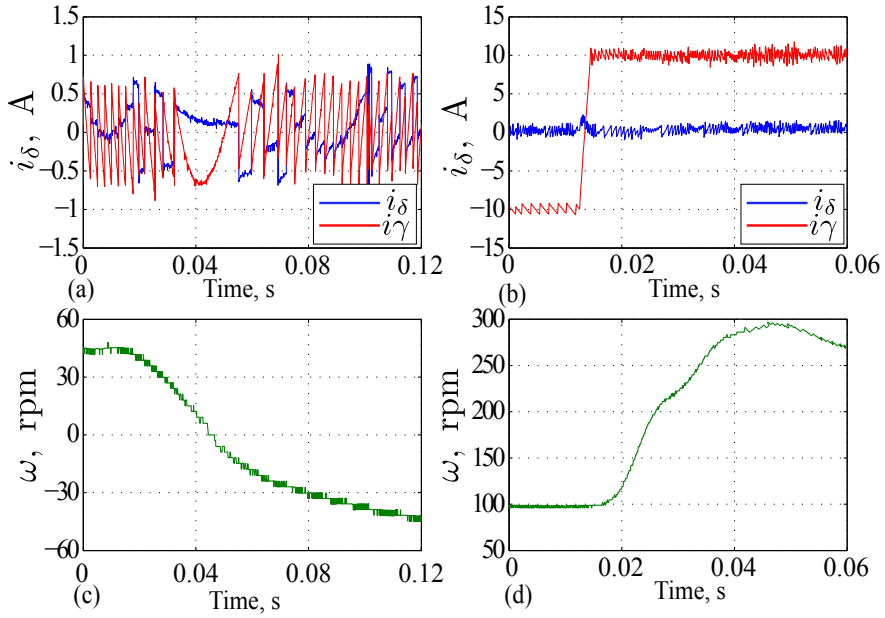

Figure 4.8: The measured currents at (a) speed reversal at 50 rpm, and (b) rated current (10 A) reversal.

The voltage vector injection by FCSMPC falls under the category of arbitrary signal injection as the response currents do not fit into that of any standard modulation based periodic signal injection (e.g. sinusoidal and square). The frequency of

Table 4.8: Summary of the voltage vector response[1] at different operating conditions

Operating conditions	$\dot{\mathbf{i}}_{\delta\gamma}$ (A/s)	$\ddot{\mathbf{i}}_{\delta\gamma}$ (A/s^2)
Standstill, $\mathbf{i}^*_{\delta\gamma} = [0\text{A}, 0\text{A}]'$	$[0, 0]'$	$[0, 0]'$
Standstill, $\mathbf{i}^*_{\delta\gamma} = [0\text{A}, 0\text{A}]'$	$[0.2\text{k}, 0.2\text{k}]'$	$[0.2\text{k}, 0.2\text{k}]'$
50 rpm, $\mathbf{i}^*_{\delta\gamma} = [0\text{A}, 0\text{A}]'$	$[0.8\text{k}, 0.6\text{k}]'$	$[0.2\text{k}, 0.05\text{k}]'$
Speed reversal[2], $\mathbf{i}^*_{\delta\gamma} = [0\text{A}, 0\text{A}]'$	$[10, 50]'$	$[5, 10]'$
Current reversal[3], $\mathbf{i}^*_{\delta\gamma} = [0\text{A}, \pm 10\text{A}]'$	$[-, 10\text{k}]'$	$[-, 5]'$

1-the average values at a particular time period, 2- at 50 rpm, 3-at 100rpm, and k = 10^3

sinusoidal injection is limited by the switching frequency as it has to apply through the pulse width modulation (Liu and Zhu, 2014). On the other hand, the injection frequency is same as the switching frequency for the vector injection and thus high frequency injection is possible except at zero speed and $\mathbf{i}^*_{\delta\gamma} = 0$. Therefore, the vector injection is also a good PE as it generates strong switching ripples with high values of first and second order derivatives excluding the short periods of speed and torque transients. There is no requirement for additional signal injection for FCSMPC (unlike the vector control) to simultaneously identify the parameters as it inherently applies the voltage vectors to perform the control action and produces strong switching ripples.

4.6 Summary

This chapter introduces the concept of persistent excitation and nonlinear observability and presents the relationship between them. The persistent excitation requirements to meet the observability of the machine parameters, position and speed for IPMSM are analyzed. It is found that the first and second order derivatives of the current should be nonzero to simultaneously estimate all the parameters. Moreover,

it is proved based on the experimental results that voltage vector injection by FC-SMPC fulfills the requirements of a PE input enabling the identifiability of all the parameters, position and speed.

Chapter 5

Online Estimation of Parameters

5.1 Introduction

This chapter presents the proposed online estimation scheme to estimate the electrical machine parameters. The estimation is realized with the help of recursive least square (RLS) adaptation algorithm. The RLS formulations for different parameter combinations are presented. The parameter combinations which are not identifiable at steady state without persistent excitation are only considered for the experimentation. The experimental results show that all these parameter combinations are identifiable by online estimation as the voltage vector injection by FCSMPC establishes the persistent excitation. Moreover, the parameter coupling in estimation that results in wrong convergence is analyzed and a decoupling technique is proposed.

5.2 Online Parameter Estimation Scheme

The proposed online estimation scheme for estimating the electrical parameters of the reference IPMSM (see Appendix B for details) which is controlled by FCSMPC is based on recursive least square (RLS) adaptation algorithm. All the four electrical parameters $\hat{L}_d$, $\hat{L}_q$, $\hat{\psi}_m$, and $\hat{R}$ are considered for estimation. The parameter notation with accent $\hat{}$ indicates the estimation and without $\hat{}$ corresponds to the actual value. The RLS estimates the parameters at every sampling interval by minimizing the weighted linear least square cost function with respect to filter coefficients (parameters) (Bhotto and Antoniou, 2013). The block diagram of the proposed scheme is depicted in Fig. 5.1. The position and speed information are obtained from the encoder attached with the IPMSMS and therefore FCSMPC and RLS are realized on dq frame. The measured three phase currents and the reference voltage vectors are transformed to dq frame and fed to RLS estimator and FCSMPC. The details of the FCSMPC is provided in section 4.4, however, it should be noted that the corresponding cost function should be transformed from $\delta\gamma$ to dq frame by setting $\hat{\vartheta} = 0$.

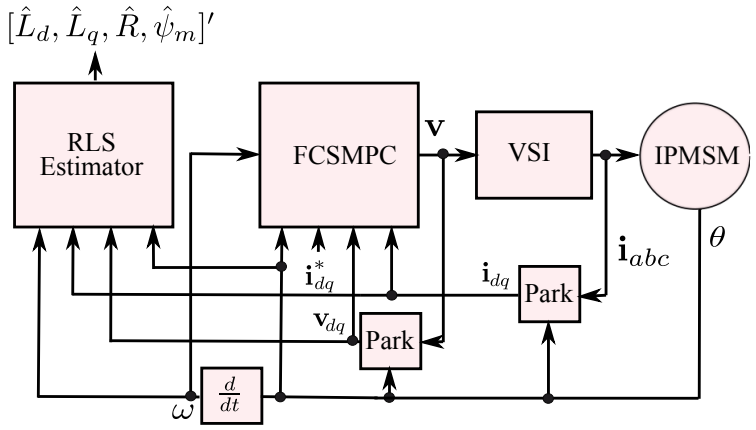

Figure 5.1: The block diagram of the proposed online parameter estimation scheme.

5.2.1 Recursive Least Square (RLS)

The RLS adaptation algorithm is derived by analytically solving the minimization problem with respect to filter parameters ($\wp \in \mathbb{R}^n$) over the iteration $i = 0 \rightarrow k$ where k is the sampling instant (Bhotto and Antoniou, 2013). The associated cost function is the weighted squared error between the desired output ($\mathbf{y}_k \in \mathbb{R}^m$) and the estimated output ($\hat{\mathbf{y}}_k \in \mathbb{R}^m$).

$$\underset{\wp_k}{\text{minimize}} \sum_{i=1}^{k} \lambda^{k-i} \|[\mathbf{y}_i - \mathbf{u}_i' \wp_k]\|^2 \tag{5.1}$$

where λ is the forgetting factor with power of $k-i$, $\mathbf{u}_i \wp_k = \hat{\mathbf{y}}_k$, and $\mathbf{u}_i \in \mathbb{R}^{m \times n}$ is a matrix if $m > 1$ or else a row vector $\in \mathbb{R}^{1 \times n}$ consisting inputs.

The solution of (5.1) is obtained by setting its partial derivatives with respect to $\wp_k$, equal to zero, and expressing it in the matrix form as

$$\wp_k = \mathbf{R}_k^{-1} \mathbf{r}_k \tag{5.2}$$

where, $\mathbf{R}_k$ and $\mathbf{r}_k$ are the weighted sample covariance of $\mathbf{u}_k$ and the cross-covariance between $\mathbf{y}_k$ and $\mathbf{u}_k$ respectively, and expressed as

$$\begin{cases} \mathbf{R}_k = \lambda \mathbf{R}_{k-1} + \mathbf{u}_k \mathbf{u}_k' \\ \mathbf{r}_k = \lambda \mathbf{r}_{k-1} + \mathbf{u}_k' \mathbf{y}_k \end{cases} \tag{5.3}$$

By letting $\mathbf{P}_k = \mathbf{R}_k^{-1}$ and with the help of Woodbury matrix identity (Hayes, 1996), it can expressed in a compact form as

$$\mathbf{P}_k = \lambda^{-1}(\mathbf{P}_{k-1} - \mathbf{g}_k \mathbf{u}_k' \mathbf{P}_{k-1}) \tag{5.4}$$

where $\mathbf{g}_k$ is the gain matrix

$$\mathbf{g}_k = \mathbf{P}_{k-1}\mathbf{u}_k(\lambda + \mathbf{u}_k'\mathbf{P}_{k-1}\mathbf{u}_k)^{-1} \tag{5.5}$$

By substitution second equation of 5.3 and letting $\mathbf{P}_k = \mathbf{R}_k^{-1}$ in 5.2, it becomes

$$\boldsymbol{\rho}_k = \mathbf{P}_k(\lambda\mathbf{r}_{k-1} + \mathbf{u}_k'\mathbf{y}_k) \tag{5.6}$$

By applying the recursive definitions of $\mathbf{r}_k$, $\mathbf{P}_k$, and $\boldsymbol{\rho}_k$, 5.6 can be simplified and expressed in the form of a final solution as

$$\boldsymbol{\rho}_k = \boldsymbol{\rho}_{k-1} + \mathbf{g}_k(\mathbf{y}_k - \mathbf{u}_k'\boldsymbol{\rho}_{k-1}) \tag{5.7}$$

According to 5.7, the RLS updates the error between the actual ($\mathbf{y}_k$) and the estimated outputs ($\mathbf{u}_k'\boldsymbol{\rho}_{k-1}$) to the next estimated parameters ($\boldsymbol{\rho}_k$) by the factor of gain $\mathbf{g}_k$. The size of $\mathbf{g}_k$ and $\mathbf{P}_k$ are $n \times m$ and $n \times n$ which are essentially depended on the size of $\mathbf{u}_k$, $\mathbf{y}_k$, and $\boldsymbol{\rho}_k$. The solution 5.7 is found at every sampling interval by updating $\mathbf{g}_k$ and $\mathbf{P}_k$, and the RLS algorithm is summarized as

$$\begin{cases} \text{Set} & : \lambda \\ \text{Initialize} & : \boldsymbol{\rho}_{k-1}, \& \ \mathbf{P}_{k-1} \\ \text{Read} & : \mathbf{u}_k, \& \ \mathbf{y}_k \\ \text{Compute} & : \mathbf{g}_k = \mathbf{P}_{k-1}\mathbf{u}_k(\lambda + \mathbf{u}_k'\mathbf{P}_{k-1}\mathbf{u}_k)^{-1} \\ & : \mathbf{P}_k = \lambda^{-1}(\mathbf{P}_{k-1} - \mathbf{g}_k\mathbf{u}_k'\mathbf{P}_{k-1}) \\ & : \boldsymbol{\rho}_k = \boldsymbol{\rho}_{k-1} + \mathbf{g}_k(\mathbf{y}_k - \mathbf{u}_k'\boldsymbol{\rho}_{k-1}) \end{cases} \tag{5.8}$$

The convergence accuracy and time of the parameter estimation are sensitive to the values of λ. The small value of λ results in less contribution of the previous samples to the covariance matrix, which means more fluctuations in the estimation but achieves faster convergence. In practice, λ is usually chosen between 0.98 and 1 (Hayes, 1996). Optimal value of λ is chosen in this thesis for estimating the different machine parameter combinations to achieve faster convergence without compromising on the accuracy.

5.2.2 RLS Formulations for Different Parameter Combinations

The RLS formulation varies for different parameter combinations. The mathematical model of IPMSM (2.10) is rearranged in such a way that it becomes compatible with RLS formulation

$$\mathbf{y}_k = \mathbf{u}'_k \wp_k \tag{5.9}$$

In order to realize this, the terms which are not the coefficients of the estimating parameters in (2.10) are moved to LHS and the remaining terms modified into the form of $\mathbf{u}_k \wp_k$ where $\wp_k$ is the estimating parameter vector.

Only the parameter combinations which are not identifiable without persistent excitation (PE) are estimated in this thesis in order to show that these observability issues can be overcome by FCSMPC with vector injection. Moreover, the combinations are grouped into two, three and four parameter sets. The RLS formulations for different parameter sets are provided in Table 5.1.

Table 5.1: RLS formulations for different parameter combinations

$\mathcal{p}_k$	$\mathbf{u}'_k$	$\mathbf{y}_k$
$[\hat{L}_d, \hat{L}_q]'$	$\begin{bmatrix} \dot{i}_{d,k}, & \omega_k i_{q,k} \\ -\omega_k i_{d,k} & \dot{i}_{q,k} \end{bmatrix}$	$\begin{bmatrix} v_{d,k} - i_{d,k}R \\ v_{q,k} - i_{q,k}R - \omega\psi_m \end{bmatrix}$
$[L_d, \psi_m]'$	$\begin{bmatrix} \dot{i}_{d,k}, & 0 \\ -\omega_k i_{d,k} & \omega_k \end{bmatrix}$	$\begin{bmatrix} v_{d,k} - i_{d,k}R - \omega_k L_q i_{q,k} \\ v_{q,k} - i_{q,k}R - \dot{i}_{q,k}L_q \end{bmatrix}$
$[R, \psi_m]'$	$\begin{bmatrix} i_{d,k}, & 0 \\ i_{q,k} & \omega_k \end{bmatrix}$	$\begin{bmatrix} v_{d,k} - \omega_k L_d \dot{i}_{d,k} - \omega_k L_q i_{q,k} \\ v_{q,k} - \dot{i}_{q,k}L_q + \omega L_d i_{d,k} \end{bmatrix}$
$[Ld, L_q, \psi_m]'$	$\begin{bmatrix} \dot{i}_{d,k}, & \omega_k i_{d,k} & 0 \\ -\omega_k i_{d,k} & \dot{i}_{q,k} & \omega_k \end{bmatrix}$	$\begin{bmatrix} v_{d,k} - i_{d,k}R \\ v_{q,k} - i_{q,k}R \end{bmatrix}$
$[Ld, L_q, R]'$	$\begin{bmatrix} \dot{i}_{d,k}, & \omega_k i_{d,k} & i_{d,k} \\ -\omega_k i_{d,k} & \dot{i}_{q,k} & i_{q,k} \end{bmatrix}$	$\begin{bmatrix} v_{d,k} \\ v_{q,k} - \omega_k \psi_m \end{bmatrix}$
$[Ld, R, \psi_m]'$	$\begin{bmatrix} \dot{i}_{d,k}, & i_{d,k} & 0 \\ -\omega_k i_{d,k} & i_{q,k} & \omega_k \end{bmatrix}$	$\begin{bmatrix} v_{d,k} - \omega_k i_{q,k} L_q \\ v_{q,k} - \dot{i}_{q,k}L_q \end{bmatrix}$
$[Lq, R, \psi_m]'$	$\begin{bmatrix} \omega_k i_{d,k}, & i_{d,k} & 0 \\ \dot{i}_{d,k} & i_{q,k} & \omega_k \end{bmatrix}$	$\begin{bmatrix} v_{d,k} - \dot{i}_{d,k}L_d \\ v_{q,k} + \omega i_{q,k} L_q \end{bmatrix}$
$[Ld, L_q, R, \psi_m]'$	$\begin{bmatrix} \dot{i}_{d,k}, & \omega_k i_{d,k} & i_{d,k} & 0 \\ -\omega_k i_{d,k} & \dot{i}_{q,k} & i_{q,k} & \omega_k \end{bmatrix}$	$\begin{bmatrix} v_{d,k} \\ v_{q,k} - \omega_k \psi_m \end{bmatrix}$

$\dot{i}_{d,k} = (i_{d,k} - i_{d,k-1})/T_s$, $\dot{i}_{q,k} = (i_{q,k} - i_{q,k-1})/T_s$ where T_s is sampling time.

5.3 Experimental Results

The online estimations for the combinations with two, three and four parameter sets are conducted experimentally for the reference IPMSM. The tests are carried out with the help of the experimental setup presented in Appendix B. The estimation is carried within the sampling cycle corresponding to 10 kHz switching frequency. The parameter combinations which are not identifiable at steady state without PE

are considered for the estimation in this thesis to show that the vector injection by FCSMPC is able to overcome the observability issues.

5.3.1 Estimation of Two Parameter Combinations

The combination with parameter set $\{\hat{L}_d, \hat{L}_q\}$ is considered first for online estimation. The parameters in this combination are not simultaneously identifiable at steady state when $[i_d, i_q]' = [0, 0]'$ as given in Table 4.3. However, these parameters can be identified with FCSMPC control even when the average values of the currents are zero as shown in Fig. 5.2 (a). The vector injection by FCSMPC creates small current ripples with $[\dot{i}_d, \dot{i}_q]' \neq [0, 0]'$ enables the simultaneous identification of these parameters. The estimated values closely correlate with the actual values from offline measurement provided in Appendix B. The nominal values (see Appendix B) are assumed for R and ψ_m in this case. The d and q axis current ripples are shown in Fig. 5.2 (c) and (d) respectively.

The combination $\{\hat{L}_d, \hat{\psi}_m\}$ is not observable at steady state without PE as given in Table 4.3. The experimental results in Fig. 5.2 (b) shows that the switching ripples (PE) associated with FCSMPC helps to overcome this limitation and provide accurate estimation. The test is conducted at 100 rpm with average value of $i_d = 0$. The estimated parameters closely match with the actual parameters.

The estimation of the combination $\{\hat{R}, \hat{\psi}_m\}$ is not identifiable at steady state when $i_d = 0$ without PE. The experimental results with FCSMPC in Fig. 5.3 (a) shows that these parameters are identifiable for this case as there is PE due to the switching ripples. However, the parameters converge to wrong values with large oscillations especially for $\hat{R}$. The current measurement noise, delays, and inverter nonlinearities

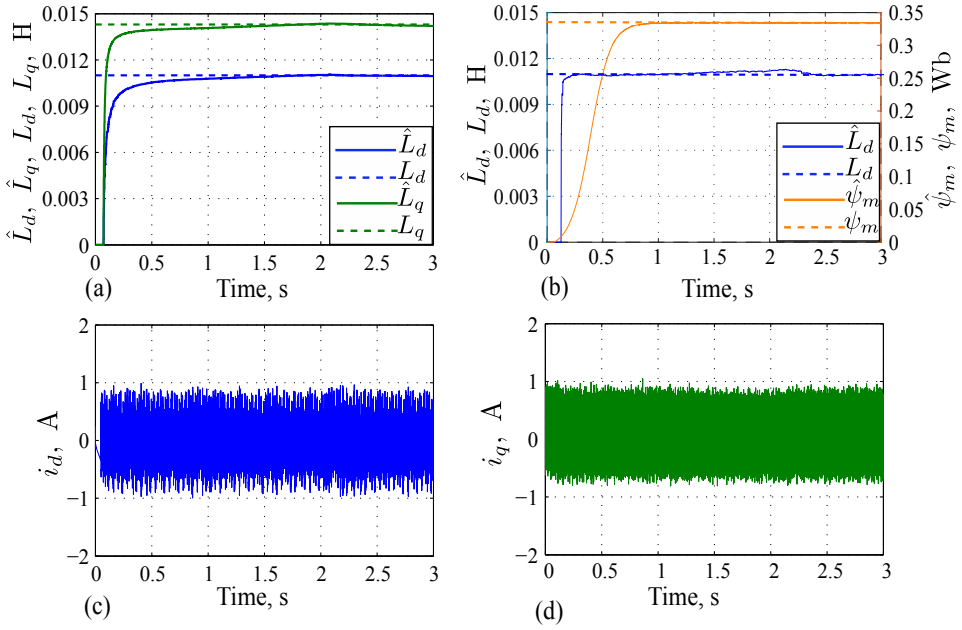

Figure 5.2: Experimental online estimation results at 100 rpm: (a) for $\{\hat{L}_d, \hat{L}_q\}$, (b) for $\{\hat{L}_d, \hat{\psi}_m\}$, and (c) and (d) the measured i_d and i_q showing the zero average.

associated with the experiments are attributed to this behavior. A small error in the estimation of $\hat{\psi}_m$ results in large error in $\hat{R}$ as they are coupled with each other in IPMSM model corresponding to q axis. This phenomenon would not appear if the value of $\hat{\psi}_m$ is much lower than $\hat{R}$.

The coupling can be broken by keeping either $i_q = 0$ or $\omega = 0$. Fig. 5.3 (b) shows the experimental results of estimating $\hat{R}$ and $\hat{\psi}_m$ with a very low speed (ω =25 rpm). The estimation is more accurate compared to Fig. 5.3 (a), however, there are still oscillations. This is due to the fact that, the complete decoupling is not achieved as ω is not exactly zero, which is not possible as ω should be greater than zero to estimate $\hat{\psi}_m$. The complete decoupling can be achieved by keeping $i_q = 0$. The experimental results for the case with $i_q = 0$ is shown Fig. 5.3 (c). The parameters are converged to the actual values. The decoupling by keeping $i_q = 0$ or $\omega = 0$ is not

practically possible in the case of motor operation. Therefore, a decoupling technique is proposed in this thesis.

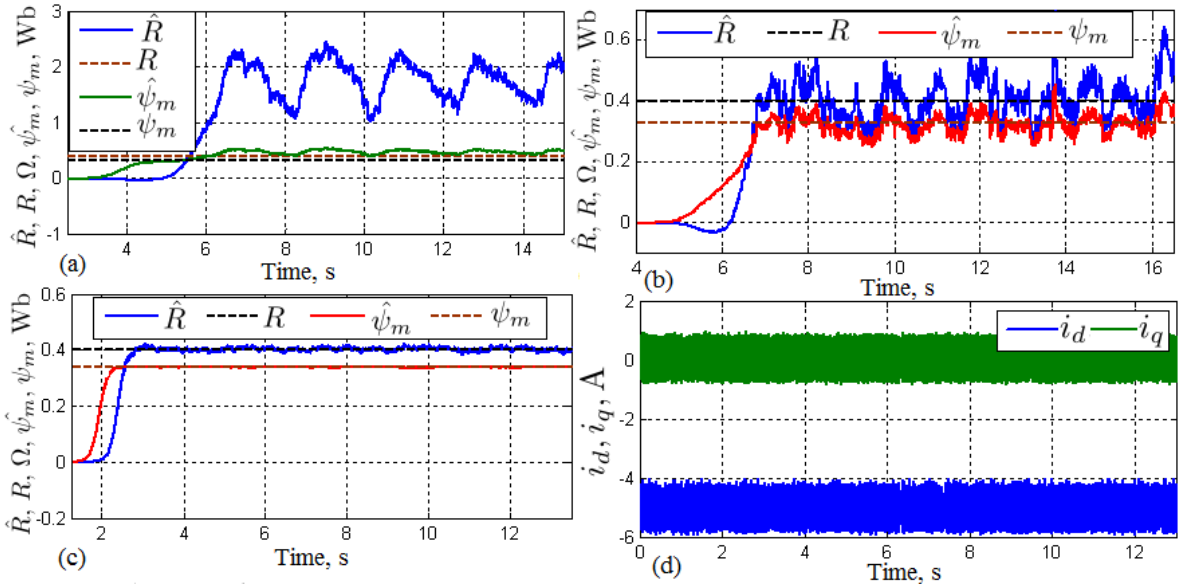

Figure 5.3: Experimental online estimation results for $\{\hat{R}, \hat{\psi}_m\}$: (a) for $i_q = 5A$, $i_d = 0A$ and 100rpm, (b) for $i_q = 5$ A, $i_d = 0$ A and 25rpm, (c) for $i_q = 0$ A, $i_d = -5$ A and 100rpm, (d) measured i_d and i_q corresponding to (c).

5.3.2 Decoupling Technique

A small variation in $\hat{\psi}_m$ creates a large variation in $\hat{R}$ as they are coupled. One way to overcome this coupling is to make the estimation of $\hat{\psi}_m$ insensitive to small variations by slowing down the convergence. It can be done by tuning the corresponding RLS forgetting factor. However, tuning for a reasonable estimation results in significantly longer convergence time.

The proposed decoupling technique in this thesis separates the estimation of $\hat{R}$ and $\hat{\psi}_m$ by two moderately fast RLSs (RLS1 and 2 respectively) as shown in Fig. 5.4 (a). The sampling rates of the two RLSs are kept high to avoid discretization error due to

low sampling rate (same as the main control algorithm, 10 kHz). The estimated value of $\hat{R}$ from RLS1 is fed to RLS2 at each sampling interval and hence establishes a direct link. On the other hand, the estimation of $\hat{\psi}_m$ by RLS2 is updated to RLS1 only when there is a considerable change in $\hat{\psi}_m$ (weak link). Consequently, the small error in $\hat{\psi}_m$ estimation does not pass to estimation of $\hat{R}$. Online experimental estimation results of $\{\hat{R}, \hat{\psi}_m\}$ is shown in Fig. 5.4 (b) with the proposed decoupling. The convergence of $\hat{\psi}_m$ is steady and accurate. There are still small oscillations in $\hat{R}$ however it can be further improved by tuning the RLS and by changing the band of $\hat{\psi}_m$ deciding whether to update the RLS1 or not.

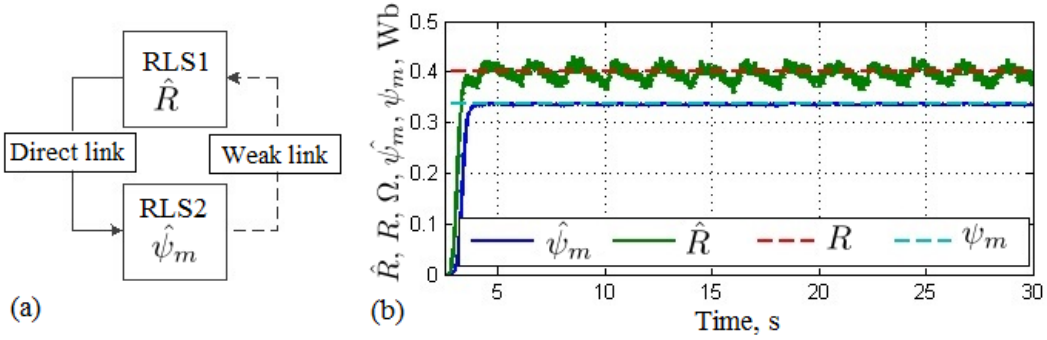

Figure 5.4: The decoupling technique for estimating $\{\hat{R}, \hat{\psi}_m\}$: (a) two RLSs based decoupling scheme (b) online experimental estimation results at $i_q = 5$ A and 100 rpm.

5.3.3 Estimation of Three Parameter Combinations

All the combinations belong three parameter sets ($\{\hat{L}_d, \hat{L}_q, \hat{\psi}_m\}$, $\{\hat{L}_d, \hat{L}_q, \hat{R}\}$, $\{\hat{L}_d, \hat{R}, \hat{\psi}_m\}$, and $\{\hat{L}_q, \hat{R}, \hat{\psi}_m\}$) are considered for online estimation. The parameter coupling between $\hat{R}$ and $\hat{\psi}_m$ is also a concern for estimating $\{\hat{L}_d, \hat{R}, \hat{\psi}_m\}$, and $\{\hat{L}_q, \hat{R}, \hat{\psi}_m\}$. The decoupling scheme with two RLSs is also implemented for these combinations similar to $\{\hat{R}, \hat{\psi}_m\}$ in section 5.3.2. The parameter $\hat{\psi}_m$ is estimated by one RLS and other

two parameters are estimated by a second RLS.

The parameters in all the three set combinations are not simultaneously identifiable at stead state without PE according to Table 4.4. The experimental results in Fig. 5.5 shows that all the three parameter combinations converge to the actual values with the help of PE by FCSMPC. The average value of i_d is zero for all the four test cases. There are small oscillations in $\hat{R}$ however this can be improved by tuning the RLS and the band of $\hat{\psi}_m$ deciding whether to update the RLS1 or not.

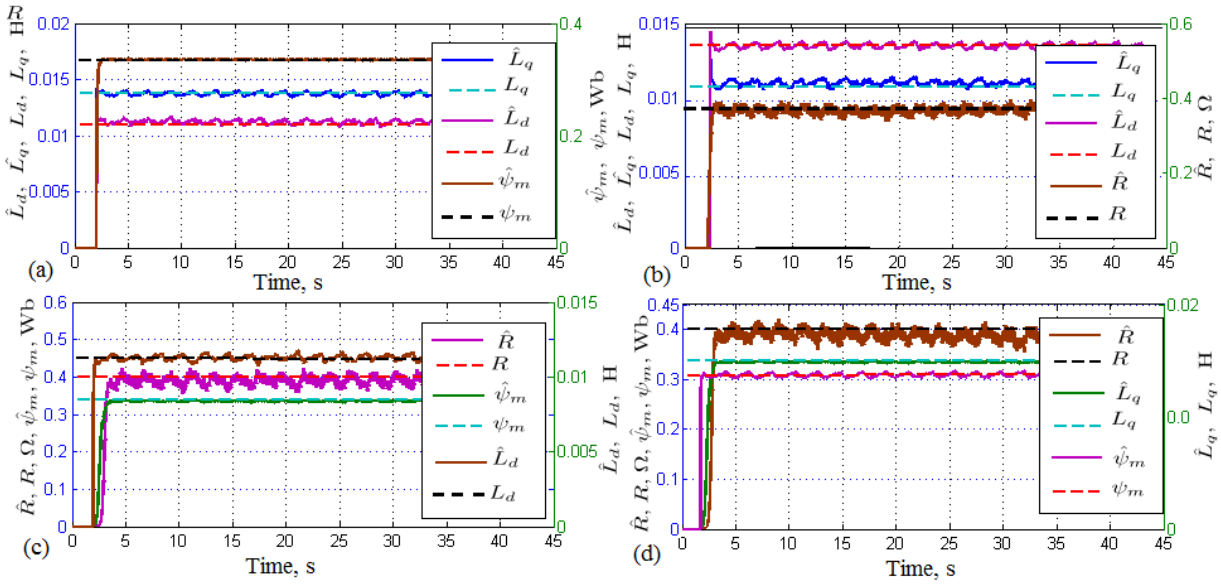

Figure 5.5: Experimental online estimation results at $i_q = 5$ A, $i_d = 0$ A, and 100 rpm : (a) for the combination $\{\hat{L_d}, \hat{L}_q, \hat{R}\}$ (b) for the combination $\{\hat{L_d}, \hat{L}_q, \hat{\psi}_m\}$, (c) for the combination $\{\hat{L_d}, \hat{R}, \hat{\psi}_m\}$, and (d) for the combination $\{\hat{L_q}, \hat{R}, \hat{\psi}_m\}$.

5.3.4 Estimation of Four Parameter Combination

The estimation of the combination with four parameters is realized by two RLSs. The first RLS estimates $\hat{\psi}_m$ and the second one estimates $\hat{L}_d$, $\hat{L}_q$ and $\hat{R}$ in order to establish the decoupling between $\hat{R}$ and $\hat{\psi}_m$. The experiments are carried out

at 50 rpm, 100 rpm, and 150 rpm. The i_q is varied from 5 A with a step of 2 A until 11 A while keeping $i_d = 0$ A. The estimation results are shown in Fig. 5.6. The estimation of parameter $\hat{\psi}_m$ is steady and does not change with the current and speed as expected. The parameter $\hat{L}_q$ decreases with increase in i_q due to saturation. The slight decrease in $\hat{L}_d$ is due to the cross-saturation.. Both $\hat{L}_d$ and $\hat{L}_q$ estimations follow the actual values. The parameter $\hat{R}$ is slightly over and under estimated at 50 rpm and 150 rpm respectively and becomes closer to the actual value at 100 rpm.

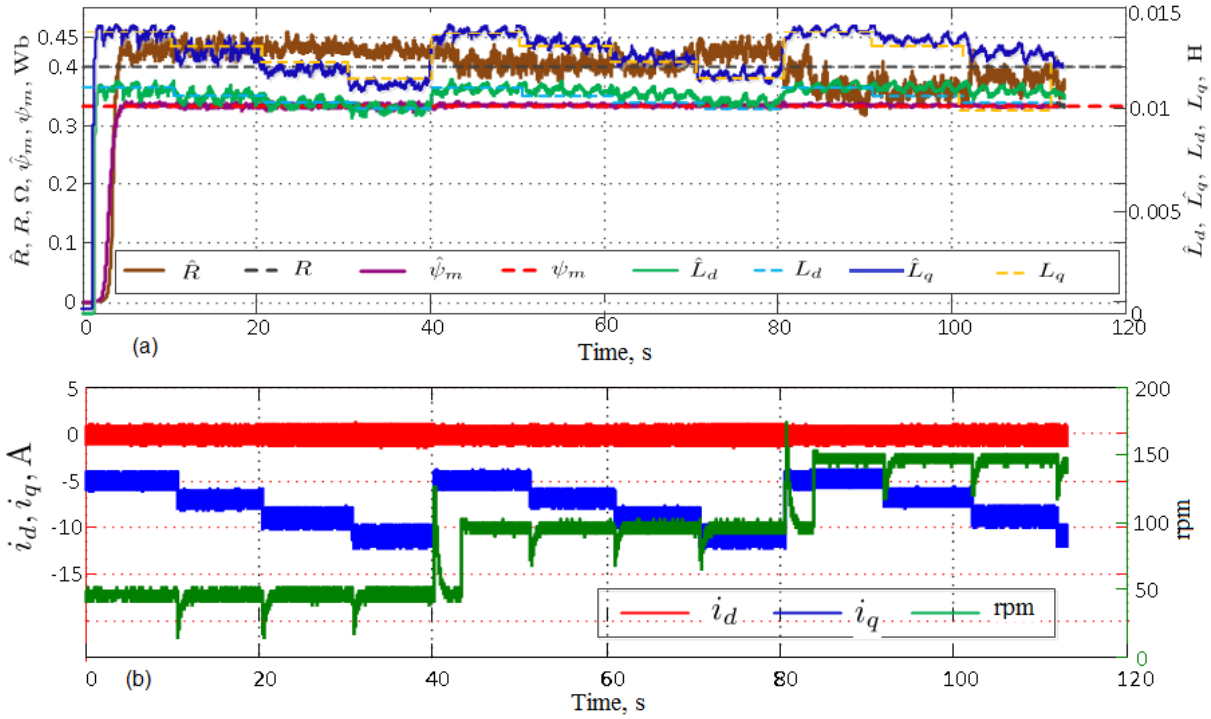

Figure 5.6: Experimental online estimation results: (a) for the combination $\{\hat{L}_d, \hat{L}_q, \hat{R}, \hat{\psi}_m)$, (b) the corresponding i_d, i_q and rpm.

5.4 Summary

This chapter presents a RLS based online adaptation scheme for estimating all the electrical parameters of the reference IPMSM. The parameter combinations which are not identifiable at steady state without persistent excitation are considered for the experimentation. The results show that the vector injection by FCSMPC establishes the persistent excitation which makes the system identifiable to all the parameters. Moreover, the results also show that the estimated parameters closely match with the actual parameters. The wrong estimations due to parameter coupling are also analyzed and showed that the proposed technique effectively decouples the parameters and improves the estimation.

Chapter 6

Online Estimation of Position and Speed

6.1 Introduction

This chapter presents online estimation of position and speed for the reference IPMSM with FCSMPC. The proposed online estimation scheme is based on nonlinear optimization as the standard position estimation techniques are not suitable for FCSMPC. A strong persistent excitation is always present with FCSMPC, and therefore the proposed method can estimate the position and speed over a wide speed range starting from standstill to the rated speed without a changeover or additional signal injection. This chapter also presents detailed convergence analysis and proposes a compensator for the standstill operation that prevents converging to saddle and symmetrical solutions. The performance of the proposed estimation scheme is experimentally verified for a wide range of operating conditions.

6.2 Position and Speed Estimations Scheme

The complete block diagram of the proposed position and speed estimations scheme for the reference IPMSM with FCSMPC is depicted in Fig. 6.1. The estimated position $\hat{\theta}$ and speed $\hat{\omega}$ are fed to FCSMPC. Therefore, the control is realized in $\delta\gamma$ frame and the cost function given in section 4.4 is adopted for FCSMPC. Moreover, the proposed scheme is essentially a position sensorless FCSMPC as the estimated position and speed are used in the control.

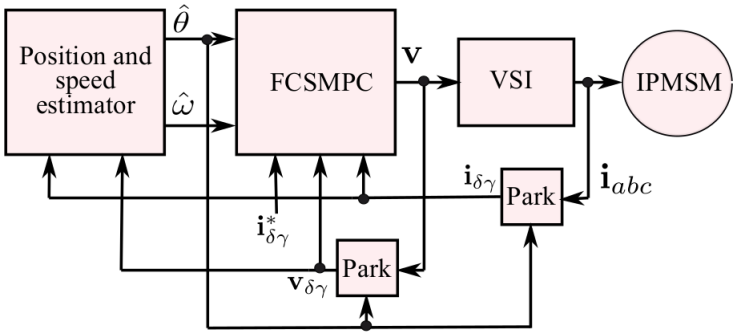

Figure 6.1: The complete block diagram of the sensorless FCSMPC.

The standard signal injection based position estimation techniques employed for low speed sensorless operation cannot be applied to FCMPC as it does not have any modulator to superimpose the injected signal with fundamental excitation. For conventional back emf (electromotive force) based high speed sensorless techniques, the low pass filters are required to eliminate the switching ripples components associated with FCSMPC. However, it is challenging to tune the filter coefficients as the frequency of the switching ripples widely varies with respect to the operating speed. Consequently, this thesis proposes a nonlinear optimization based scheme which simultaneously estimates the position and speed at every sampling interval.

6.3 Nonlinear Optimization Based Estimator

In nonlinear optimization methods, a nonlinear cost function is minimized with respect to the decision variables. For IPMSM in this thesis, the cost function is formulated in the estimated reference frame ($\delta\gamma$) which rotates with estimated velocity ($\hat{\omega}$) and displaced from the dq frame with an estimated angle difference $\hat{\vartheta}$. The mathematical model of IPMSM in $\delta\gamma$ (

This thesis employs Newton minimization along with golden-section line search as the optimization solver. Newton method guarantees quadratic convergence as long as the convergence trajectory is confined within the convex region, which can be achieved with a warm-start initialization and by incorporating a line search to ensure a descent direction for each iteration (Epelman, 2007). The iterative optimization algorithm is carried out within a sampling interval as

$$\begin{cases} \Delta \mathbf{x}_k^n = -\frac{\mathbf{J}(\mathbf{x}_k^{n-1})}{\mathbf{H}(\mathbf{x}_k^{n-1})} \\ \underset{\xi}{\text{minimize}} f(\mathbf{x}_k^{n-1} + \xi \Delta \mathbf{x}_k^n) \\ \mathbf{x}_k^n = \mathbf{x}_k^{n-1} + \xi \Delta \mathbf{x}_k^n \end{cases} \tag{6.1}$$

where $\mathbf{x}_k = [\hat{\vartheta}_k, \hat{\omega}_k]'$, $\Delta \mathbf{x}_k^n$ is Newton direction of the k^{th} sample and n^{th} Newton iteration, $\mathbf{H}$ is Hessian, and $\mathbf{J}$ is Jacobian. The line search step length (ξ) is found by the intermediate optimization (golden-section (Shefali, 2011)), which essentially finds ξ resulting from

$$f(\mathbf{x}_k^{n-1} + \xi \Delta \mathbf{x}_k^n) < f(\mathbf{x}_k^{n-1}).$$

The steps in (6.1) are repeated until $\mathbf{J}(\mathbf{x}_k) \leq \eta$ (an acceptable minimum). The

value of η is chosen to reduce the number of iterations without compromising on the accuracy of the solution. The number of iterations is further reduced in this application as there is always a warm initialization except for the initial sample. This is true from the fact that, the initialization for the k^{th} sample is the solution from $k-1^{th}$ sample, and the variations between these adjacent samples are marginal. It is also worthwhile to note that a compensator is proposed in this thesis for the initial sample at the start-up to avoid wrong convergence.

The nonlinear optimization of the cost function (**??**) finds the optimal position difference $\hat{\vartheta}_o$. The estimated position $\hat{\theta}$ is found by feeding $\hat{\vartheta}_o$ into a phase locked loop (PLL) as shown in Fig. 6.2. The compensator is executed only at the start-up from standstill and it is disconnected for the remaining operation. The estimated speed $\hat{\omega}$ is the output of the discrete filter.

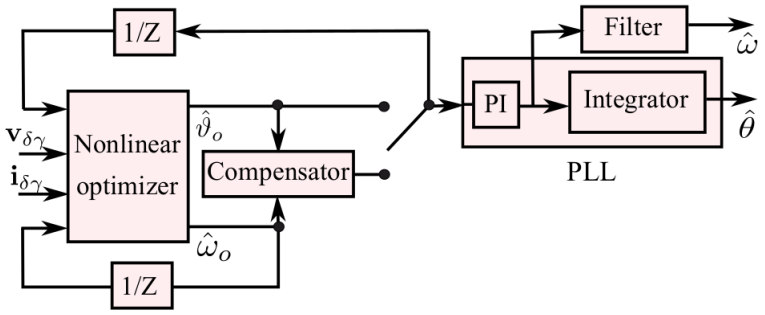

Figure 6.2: Nonlinear optimization based position and speed estimator.

6.4 Convergence Analysis

There is a global minimum if the cost function is convex, and the solution converges to this minimum as long as the convergence trajectory is confined within the convex

region. Therefore, analyzing the convex region is the fundamental part of the convergence analysis. One of the approaches to find the convex region of the cost function is with the help of the leading principal minors of its Hessian matrix (Erikson, 2010). This approach is convenient in developing analytical conditions for the convexity. The Hessian of the cost function (**??**) is

$$\mathbf{H} = \begin{bmatrix} 2\mathbf{h}'\mathbf{h}_{\hat{\vartheta}\hat{\vartheta}} + 2\mathbf{h}'_{\hat{\vartheta}}\mathbf{h}_{\hat{\vartheta}} + 2\kappa_1, & 2\mathbf{h}'\mathbf{h}_{\hat{\vartheta}\hat{\omega}} + 2\mathbf{h}'_{\hat{\vartheta}}\mathbf{h}_{\hat{\omega}} \\ 2\mathbf{h}'\mathbf{h}_{\hat{\vartheta}\hat{\omega}} + 2\mathbf{h}'_{\hat{\vartheta}}\mathbf{h}_{\hat{\omega}}, & 2\mathbf{h}'_{\hat{\omega}}\mathbf{h}_{\hat{\omega}} + 2\kappa_2 \end{bmatrix} \tag{6.2}$$

where $\mathbf{h}_{\hat{\vartheta}}$, $\mathbf{h}_{\hat{\vartheta}\hat{\vartheta}}$, $\mathbf{h}_{\hat{\omega}}$, and $\mathbf{h}_{\hat{\vartheta}\hat{\omega}}$ are the first and second order derivatives of $\mathbf{h}$ with respect to $\hat{\vartheta}$ and $\hat{\omega}$, and their expressions are

$$\begin{aligned} \mathbf{h}_{\hat{\vartheta}} &= 2L_{\Delta}\mathbf{T}(\tilde{\mathbf{P}}\dot{\mathbf{i}}_{\delta\gamma} + \mathbf{T}\tilde{\mathbf{P}}\hat{\omega}\mathbf{i}_{\delta\gamma}) + \psi\hat{\omega}\mathbf{T}\tilde{\mathbf{q}} \\ \mathbf{h}_{\hat{\vartheta}\hat{\vartheta}} &= 2\mathbf{T}\mathbf{h}_{\hat{\vartheta}} \\ \mathbf{h}_{\hat{\omega}} &= \mathbf{T}\mathbf{L}_{\delta\gamma}\mathbf{i}_{\delta\gamma} + \tilde{\mathbf{q}}\psi \\ \mathbf{h}_{\hat{\vartheta}\hat{\omega}} &= 2L_{\Delta}\mathbf{T}\mathbf{T}\tilde{\mathbf{P}}\mathbf{i}_{\delta\gamma} + \psi\mathbf{T}\tilde{\mathbf{q}} \end{aligned}$$

and the Jacobian is

$$\mathbf{J} = [2\mathbf{h}'\mathbf{h}_{\hat{\vartheta}} + 2\kappa_2(\hat{\vartheta} - \hat{\vartheta}_i), 2\mathbf{h}'\mathbf{h}_{\hat{\omega}} + 2\kappa_2(\hat{\omega} - \hat{\omega}_i)]' \tag{6.3}$$

where $\hat{\vartheta}_i$ and $\hat{\omega}_i$ are the initial values (from the preceding sample).

Hessian (6.2) has two leading principal minors

$$\begin{aligned} m_1 &= h_{11} \\ m_2 &= |\mathbf{H}| \end{aligned} \tag{6.4}$$

where h_{11} is the first element and $|\mathbf{H}|$ is the determinant of $\mathbf{H}$.

The required conditions for the convexity are (Erikson, 2010)

$$m_1 > 0 \text{ and } m_2 > 0 \tag{6.5}$$

The values of $\hat{\vartheta}$ and $\hat{\omega}$ at the boundary of the convexity region can be numerically found by solving $m_1 = 0$ and $m_2 = 0$. In addition to those actual values, this thesis presents the simplified analytical expressions for the leading principal minors in order to arrive the conditions for the convexity. The simplification is carried out only for the sake of convergence analysis, and the actual Hessian (6.2) and the cost function (**??**) are used for the optimization. The simplification is carried out by neglecting the less significant terms from the original expressions for low speed and high speed cases.

6.4.1 High Speed Convergence Analysis

The back emf is the major component in the original leading principal minors (6.4) at high speed and therefore the current terms ($\dot{\mathbf{i}}_{\delta\gamma}$, $\mathbf{i}_{\delta\gamma}$) are neglected to find the simplified expressions for analyzing the convex region. Thus, the first simplified principle minor is derived as

$$m_1^h = 2\psi\hat{\omega}|\mathbf{v}_{\delta\gamma}|\cos(\hat{\vartheta} + \tan^{-1}\frac{v_\delta}{v_\gamma}), \tag{6.6}$$

where superscript h indicates high speed, and the first convexity condition by applying $m_1^h > 0$ is

$$\tan^{-1}\frac{v_\delta}{v_\gamma} - \frac{\pi}{2} < \tan^{-1}\frac{v_\delta}{v_\gamma} - \frac{\pi}{2} > \hat{\vartheta} \begin{cases} < \tan^{-1}\frac{v_\delta}{v_\gamma} + \frac{\pi}{2} & \text{for } \hat{\omega} > 0 \\ > \tan^{-1}\frac{v_\delta}{v_\gamma} + \frac{\pi}{2} & \text{for } \hat{\omega} < 0 \end{cases} \tag{6.7}$$

Similarly the second principle minor is derived as

$$m_2^h = 4\psi^2 \left[\frac{m_1}{2} - |\mathbf{v}_{\delta\gamma}|^2 \sin(\hat{\vartheta} + \tan^{-1}\frac{v_\delta}{v_\gamma})^2 \right] \tag{6.8}$$

and the second convexity condition by applying $m_2^h > 0$ is

$$\omega \begin{cases} > \frac{|\mathbf{v}_{\delta\gamma}| \sin(\hat{\vartheta} + \tan^{-1}\frac{v_\delta}{v_\gamma})^2}{2\psi \cos(\hat{\vartheta} + \tan^{-1}\frac{v_\delta}{v_\gamma})}, & \text{for } d^h > 0 \\ < \frac{|\mathbf{v}_{\delta\gamma}| \sin(\hat{\vartheta} + \tan^{-1}\frac{v_\delta}{v_\gamma})^2}{2\psi \cos(\hat{\vartheta} + \tan^{-1}\frac{v_\delta}{v_\gamma})}, & \text{for } d^h < 0, \end{cases} \tag{6.9}$$

where d^h is the denominator $2\psi \cos(\hat{\vartheta} + \tan^{-1}\frac{v_\delta}{v_\gamma})$ in (6.9).

The convex region at high speed is plotted based on the approximated (6.13, 6.9) and the original conditions (6.4) for the reference IPMSM machine (see Appendix B for the machine details) along with its cost function at 314 rad/s (600 rpm), $i_q = 2$ A, $i_d = 0$ A, and $\dot{i}_d = \dot{i}_q = 0$ A in Fig. 6.3. It is shown that the difference between the original and the approximated convex regions is negligible. Moreover, the cost function is odd symmetric and has four equilibrium solutions

$$\begin{vmatrix} s_1 : (\hat{\vartheta}_o, \hat{\omega}_o) & s_3 : (\hat{\vartheta}_o + \frac{\pi}{2}, 0) \\ s_2 : (\hat{\vartheta}_o - \pi, -\hat{\omega}_o) & s_4 : (\hat{\vartheta}_o - \frac{\pi}{2}, 0). \end{vmatrix}$$

The solution s_1 is the optimal solution and $\hat{\vartheta}_o$ and $\hat{\omega}_o$ are the optimal values of $\hat{\vartheta}$ and $\hat{\omega}$. The solutions s_3 and s_4 at $\hat{\omega} = 0$ are saddle solutions. The symmetrical solution s_2 is shifted by π rad from the optimal solution. The non-convex region in Fig. 6.3 is not concave ($m_1 < 0,$ and $m_2 > 0$) [24] and therefore it is a saddle region where neither minimum nor maximum exists.

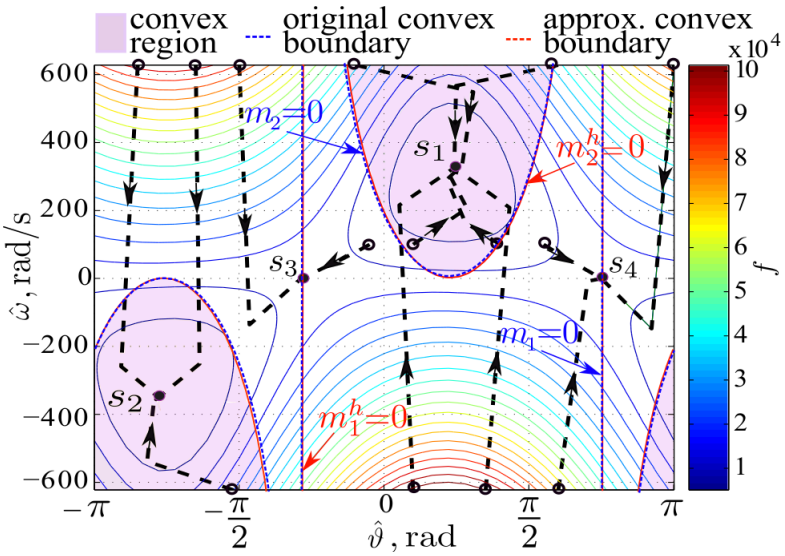

Figure 6.3: The contour plot of the cost function (f), convex region, and the convergence trajectories for the high speed case.

Fig. 6.3 also shows the convergence trajectories of Newton iterations starting from different initial conditions. The intermediate trajectories by line search is omitted in the plot. The trajectories with their starting points in the convex region are converged to the optimal solution. The iterations with initial $\hat{\omega}$ having the opposite sign as compared to $\hat{\omega}_o$ also converge to the optimal solution as long as the initial $\hat{\vartheta}$ is close to $\hat{\vartheta}_o$. Otherwise, the iterations converge to either symmetrical or a saddle solution (s_3/s_4) depending on the location of the initial condition. All the trajectories in Fig. 6.3 are converged within three Newton and six line search iterations.

6.4.2 Low Speed Convergence Analysis

The current derivative term is the major component in the original leading principle minors (6.4) at low speed because its value is kept high (by signal injection or by voltage vectors) to provide persistent excitation to meet the well known observability condition for IPMSMs (see section 4.1). Thus, it enables to neglect the terms with $\mathbf{i}_{\delta\gamma}$ from the original leading principal minors to find the simplified expressions for analyzing the convex region. The first simplified leading principle minor for the low speed case is

$$m_1^l = 2\psi\hat{\omega}(a+b) - 8L_2(c - L_\Sigma d), \tag{6.10}$$

where,

$$\begin{aligned}
a &= |\mathbf{v}_{\delta\gamma}|\cos(\hat{\vartheta} + \tan^{-1}\frac{v_\delta}{v_\gamma}) \\
b &= |\dddot{\mathbf{i}}_{\delta\gamma}|\cos(\hat{\vartheta} + \tan^{-1}\frac{\dddot{i}_\delta}{\dddot{i}_\gamma})(L_\Delta - L_\Sigma) \\
c &= |\dddot{\mathbf{i}}_{\delta\gamma}||\mathbf{v}_{\delta\gamma}|\cos(\hat{\vartheta} + \tan^{-1}\frac{v_\delta}{v_\gamma} + \tan^{-1}\frac{\dddot{i}_\delta}{\dddot{i}_\gamma}) \\
d &= |\dddot{\mathbf{i}}_{\delta\gamma}|\cos(2\hat{\vartheta} + 2\tan^{-1}\frac{\dddot{i}_\delta}{\dddot{i}_\gamma})
\end{aligned}$$

where superscript l indicates low speed, and the first convexity condition by applying $m_1^l > 0$ is

$$\omega \begin{cases} > \frac{8L_\Delta(c - L_\Sigma d)}{2\psi(a+b)}, & \text{for } d^l > 0 \\ < \frac{8L_\Delta(c - L_\Sigma d)}{2\psi(a+b)}, & \text{for } d^l < 0, \end{cases} \tag{6.11}$$

where d^l is the denominator $2\psi(a+b)$ in (6.11). Similarly the simplified expression for the second leading principle minor for the low speed case is

$$m_2^l = 2\psi^2 \left[m_1 - 2(a+b)^2 \right], \tag{6.12}$$

and the second convexity condition by applying $m_2^l > 0$ is

$$\omega \begin{cases} > \frac{8L_\Delta(c - L_\Sigma d) + 2(a+b)^2}{2\psi(a+b)}, & \text{for } d^l > 0 \\ < \frac{8L_\Delta(c - L_\Sigma d)2 + (a+b)^2}{2\psi(a+b)}, & \text{for } d^l < 0 \end{cases} \tag{6.13}$$

According to the conditions (6.11) and (6.13), the cost function for the surface permanent magnet machines is not convex at $\hat{\omega} = 0$ as $L_\Delta = 0$. For IPMSMs, at least one current derivative must be nonzero to maintain the convexity.

The convex region at low speed with the help of approximated (6.11, 6.13) and the original (6.4) conditions along with the cost function for the reference IPMSM at 0 rad/s, $\dot{i}_\gamma = 10000$A/s, $\dot{i}_\gamma = 1000$ A/s, $i_\delta = 0$ A, and $i_\gamma = 2$ A are plotted in Fig. 6.4. The difference between the approximated and the original convex regions is negligible. Moreover, the convex boundaries by two approximated conditions (6.11) and (6.13) are overlapped. The cost function is odd symmetric and has four equilibrium solutions

$$\begin{vmatrix} s_1 : (\hat{\vartheta}_o, \hat{\omega}_o) & s_3 : (\hat{\vartheta}_o + \frac{\pi}{2}, \hat{\omega}_s) \\ s_2 : (\hat{\vartheta}_o - \pi, -\hat{\omega}_o) & s_4 : (\hat{\vartheta}_o - \frac{\pi}{2}, -\hat{\omega}_s), \end{vmatrix}$$

where $\hat{\omega}_s$ is the angular speed at the saddle solutions s_3 and s_4. The solution s_1 is the optimal solution and s_2 is the symmterical solution shifted by π rad from $\hat{\vartheta}_o$.

Fig. 6.4 also shows Newton trajectories without intermediate solutions by line

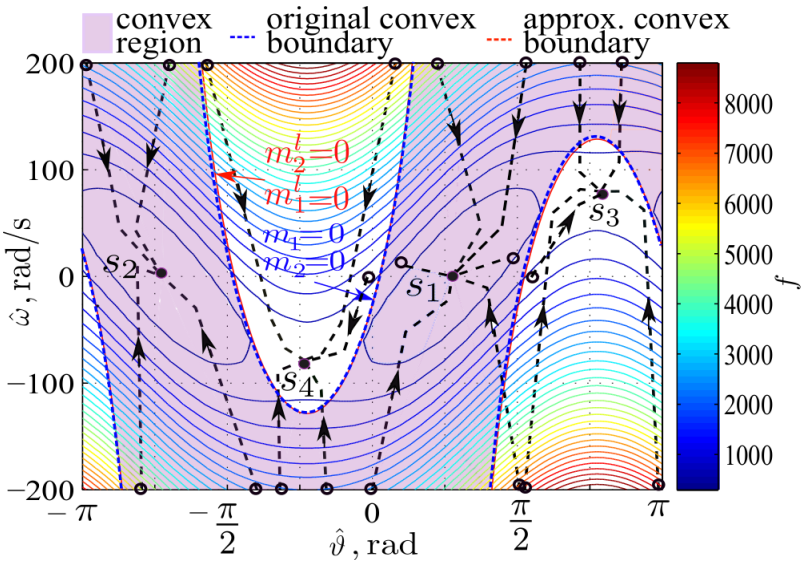

Figure 6.4: The contour plot of the cost function (f), convex region, and the convergence trajectories for the low speed case.

search. All the trajectories started within the convex region are converged to the optimal solution except those near the saddle or symmetrical points as shown in Fig. 6.4. Similar to the high speed case all the trajectories are converged within three Newton and six line search iterations, and the non-convex region is not concave but the saddle region.

6.5 Compensator Design

The position error solution by nonlinear optimization is more susceptible to saddle and symmetrical convergence at the start-up of the operation as the initial conditions are unknown. If the initial speed is kept as zero, which is true at the start-up, the narrow convex region at $\hat{\omega} = 0$ also increases the possibility of wrong convergence as in Fig. 6.4. Therefore, this thesis focuses on designing a compensator only for

the start-up from standstill. Once the correct standstill position is known, then the compensator is removed for the further operation. The compensation for the symmetrical solution is essentially the compensation for the opposite magnetic polarity and therefore the proposed compensator is also an integrated polarity detector.

If the solution has converged to saddle points at standstill, then the speed solution is nonzero according to Fig. 6.4. If the speed solution is zero then the solution is either optimal or symmetrical. The angular distances from the symmetrical and the saddle solutions to the optimal solution are π and $\frac{\pi}{2}$ respectively. The compensator is designed based on these convergence characteristics. The proposed compensator, as illustrated in Fig. 6.5 (a) detects whether the speed solution is zero, positive or negative. If the speed is positive/negative then the algorithm chooses path-2/path-3 and subtracts/adds $\frac{\pi}{2}$ to correct the saddle solution to the optimal solution. The algorithm chooses path-1 if the speed is zero then adds $\frac{\pi}{2}$ to force the solution to a saddle point and runs the algorithm once again to move the saddle solution to the optimal solution.

6.6 Experimental Validation

The proposed position estimation technique was experimentally validated for the reference IPMSM with the details given Appendix B. The tests were conducted in the motor dyno (see Appendix B for details) which consists of an induction motor with the Yaskawa drive. The motor control and position estimator algorithms for the reference IPMSM are implemented in MicroAutobox II. The controllers are configured to run the IM in speed control and the IPMSM in current control. The sampling frequency is kept at 10kHz.

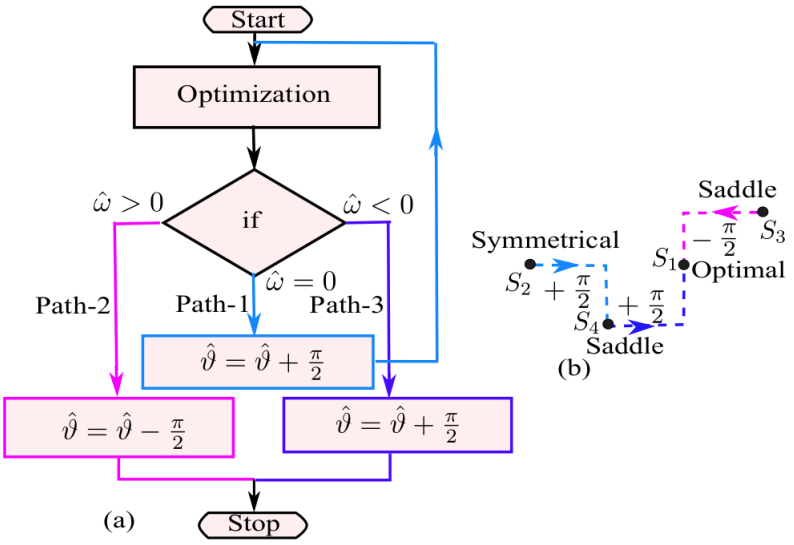

Figure 6.5: (a) Compensation flow chart, and (b) compensation trajectory.

6.6.1 Standstill Performance

The FCSMPC injects null voltage vector at standstill when the reference currents (i_δ^* and i_γ^*) are zero and essentially stops persistent excitation as mentioned in section 4.5. In this situation the position becomes not observable according to section 4.1. In order to overcome this situation, a negative reference current (-1 A) is applied in δ axis. The position estimation at standstill with $i_\delta^* = -1$ A and $i_\gamma^* = 0$ A is shown in Fig. 6.6. The position error ($\hat{\vartheta}_o$) is 1.5 rad at the open loop and the estimated position ($\hat{\theta}$) is zero as the PLL is not in action. At the closed loop, the PLL takes the position error to zero irrespective of whether it is an optimal, saddle or symmetrical solutions however the wrong convergence can be reflected in the estimated position $\hat{\theta}$. In Fig. 6.6 (a), the solution is a symmetrical solution as there is a π shift from the actual position (θ_{act}). At 4 s, the compensator comes into action as shown in

Fig. 6.6 (b) and the estimated position converges to the actual position. The time 4 s to start the compensation is chosen only for the demonstration however in the actual sensorless operation, the compensation begins at the start-up.

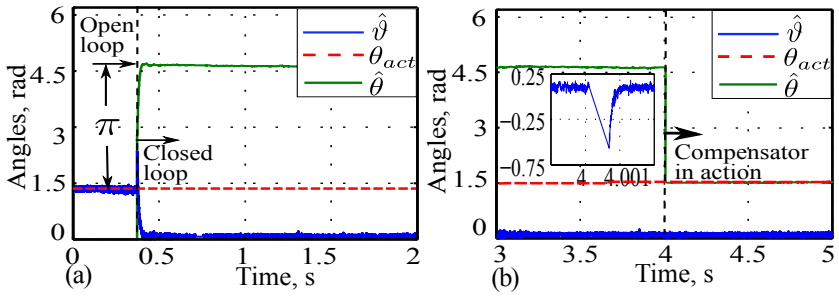

Figure 6.6: Position estimation at standstill with $i_\delta^* = -1$ A and $i_\gamma^* = 0$ A: (a) open loop till 0.4 s and then closed loop (b) the compensator in action at 4 s.

6.6.2 Speed Transient Performance

The speed transient performance of the proposed nonlinear optimization based sensorless FCSMPC is validated by conducting the speed reversal and sweep tests. The performance of the speed reversal tests at 50 rpm with no load and 50% rated load are shown in Fig. 6.7. The steady state position error for the case of no load is 0.03 rad and that for the half rated load is 0.14 rad. The increased error with loading attributes to the deviation from the nominal inductances by saturation. The steady state position error values from both the tests are close to the nonlinear optimization based sensorless vector control presented in (Sun *et al.*, 2017). The transient performance at no load case is also comparable with (Sun *et al.*, 2017) however the position error at half the rated load decreases at the transition period. This is due to the fact that the estimated position while generating in Fig. 6.7(e-h) is below the actual position, and when the machine transitions to motoring, the estimated position moves close to

the actual as the estimation response is slower than the system. The same test at 50 rpm and half the rated load is repeated for the transition from motoring to generating with a positive load current as shown in Fig. 6.8(a-b). For this case, the magnitude of the steady state position error is as same as in Fig. 6.7(e) however the estimated position is higher than the actual. Therefore, when the machine slows down at the transition to generation the actual position falls further below the estimated position causing higher position error at the transient. In both the cases the nonlinear optimizer estimates the position error promptly and PLL takes the estimated position back to its steady state value.

The steady state position error at higher loads for the nonlinear optimization based sensorless vector control reduces considerably with increase in the speed as the back emf component becomes dominant (Sun *et al.*, 2017). The steady state position error at 100 rpm and half the rated load for the nonlinear optimization based sensorless vector control is 0.08 rad (see Fig. 6.8(f)) which is 0.05 rad smaller as compared to the sensorless FCSMPC at the same operating condition (Fig. 6.9(b)). The current dynamic component is prominent as compared to the back emf term for the case of FCSMPC at 100 rpm due to the presence of high frequency switching ripples, and therefore the steady state error due to the core saturation appears. On the other hand, the switching ripples with FCSMPC helps to improve the transient performance at the speed reversals by maintaining the observability at lower speed as compared to the sensorless vector control as shown in Fig. 6.8(f) and Fig. 6.9(b). The back emf term becomes dominant over the current dynamic component at 200 rpm for the FCSMPC and therefore the position error decreases by 0.06 rad as shown in Fig. 6.9(f) as compared to 100 rpm in Fig. 6.9(b). The position error is smooth at

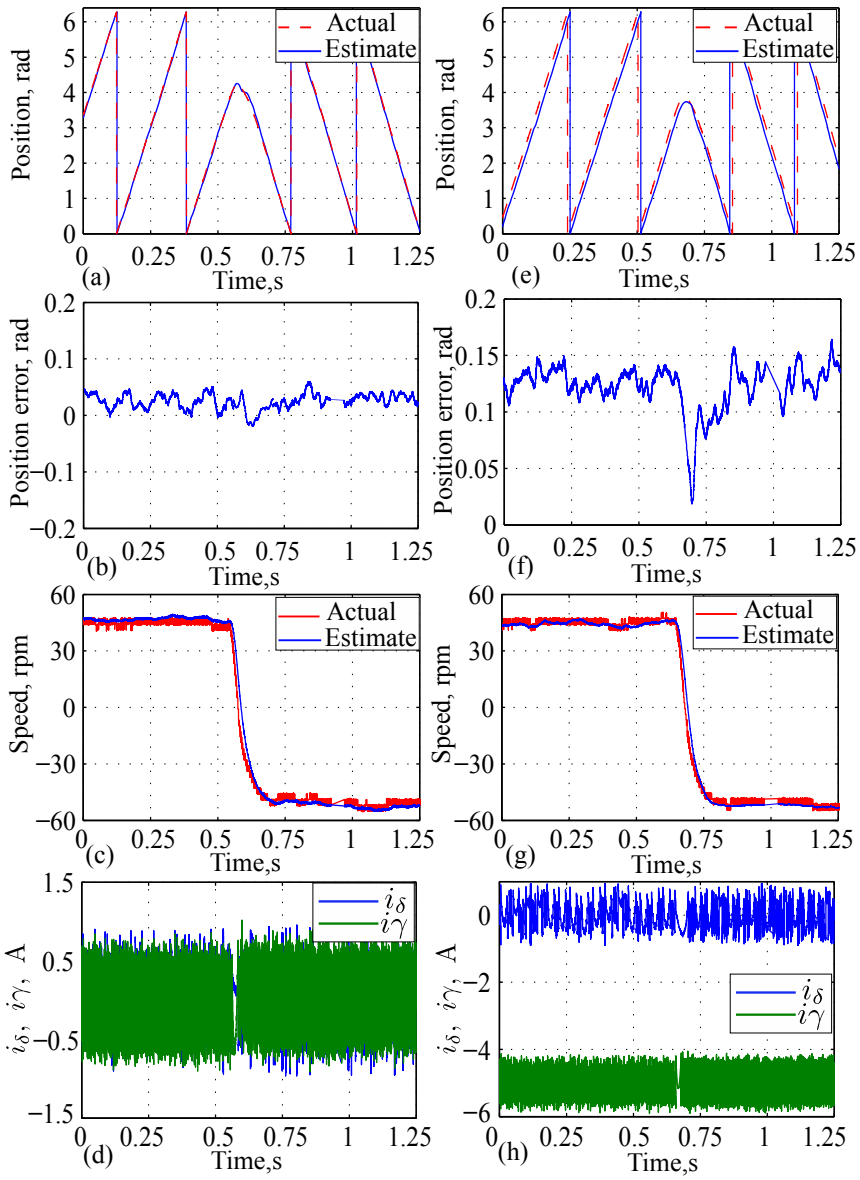

Figure 6.7: Experimental speed reversal performance of sensorless FCSMPC at 50 rpm: (a)-(d) at no load, and (e)-(h) at 50% rated load.

200 rpm as compared to the lower speeds as the effects of current measurement noise reduces with increase in the back emf. Moreover, the current is steady at the speed transition for the case of FCSMPS as it has inherently fast response as compared to

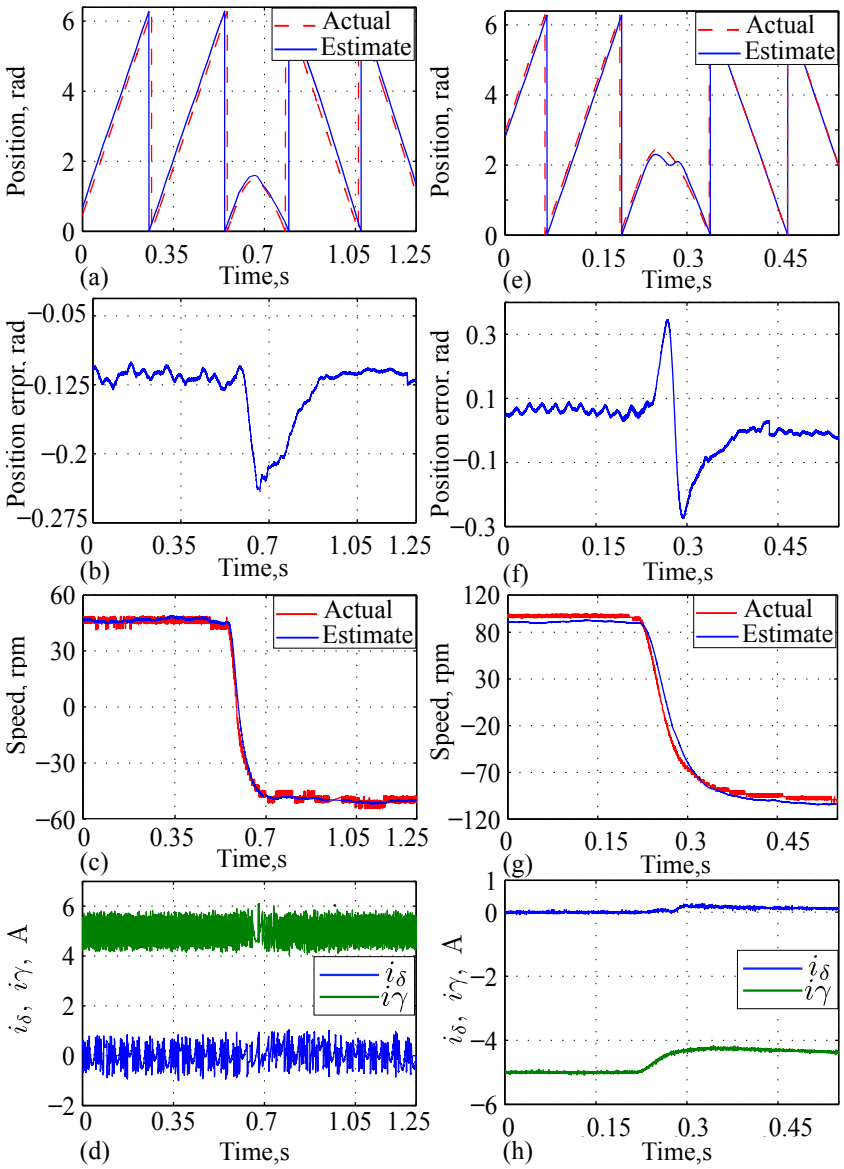

Figure 6.8: Experimental speed reversal performance at 50% rated load: (a)-(d) for sensorless FCSMPC with transition from motoring to generation at 50 rpm, and (e)-(h) for sensorless vector control at 100 rpm.

the vector control.

The steady state position error at the full rated load is increased by 0.105 rad as shown in Fig. 6.10 (a-b) as compared to the half rated load. However, that for the full

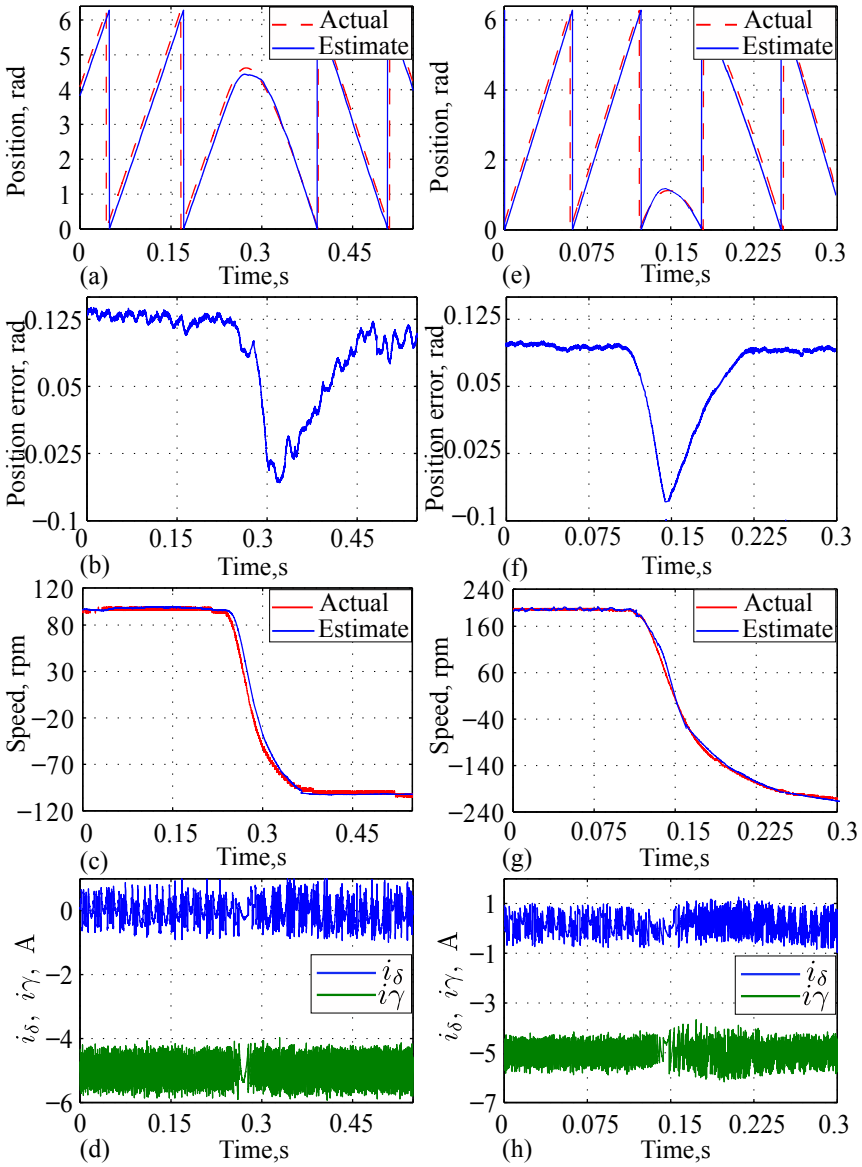

Figure 6.9: Experimental speed reversal performance of sensorless FCSMPC at 50% rated load: (a)-(d) at 100 rpm, and (e)-(h) at 200 rpm.

load to 150% rated load, it is increased by only 0.05 rad as shown in Fig. 6.10(e-f). This shows that at 150% rated load the core is close to the complete saturation and the sensorless FCSMPC is stable with a large variations in the inductance.

The speed sweep from standstill to half the rated speed (350 rpm) and back within 150 ms are conducted to validate the performance of the nonlinear optimization based sensorless FCSMPC subjected to large speed transients. The results with 25% rated load are presented in Fig. 6.11 (a-d) for the FCSMPS and in (e-f) for the vector control. The reference δ axis current to produce the persistent excitation at standstill as mentioned in section VI A is not required for this case as the γ axis reference current is set at -2.5 A to produce the torque. On the other hand, a 500 Hz and 70 V sinusoidal injection is applied for the vector control till 50 rpm. The position error at the standstill for FCSMPC is 0.03 rad which is same as the no load case and that means that the core is not saturated at 25% rated load. The standstill position error for the vector control is 0.075 rad which is close to the value presented in (Sun *et al.*, 2017). The low standstill position error for the FCSMPC attributes to the large switching ripples. The position errors at the transient state for both the control methods are close except 0.05 rad reduction in the peak value when the speed rises for the FCSMPC as compared to the vector control.

The experimental validation of proposed sensorless scheme at very high speed (say >10000 rpm) is limited by the speed rating (700 rpm) of the reference machine. However, the proposed scheme can also be applied to high speed machine by retuning the parameters. High value of the regularization constants (κ_1 and κ_2) deteriorates the estimation at very high speed and therefore the values need to be retuned. The speed dependent machine parameters viz., winding resistance and core loss also influence the estimation performance at very high speed. The variation of the winding resistance has less significance on the estimation accuracy as discussed in section VI D, and the influence of the core loss is kept out of the scope from the present thesis as it requires

an elaborate treatment of the IPMSM model.

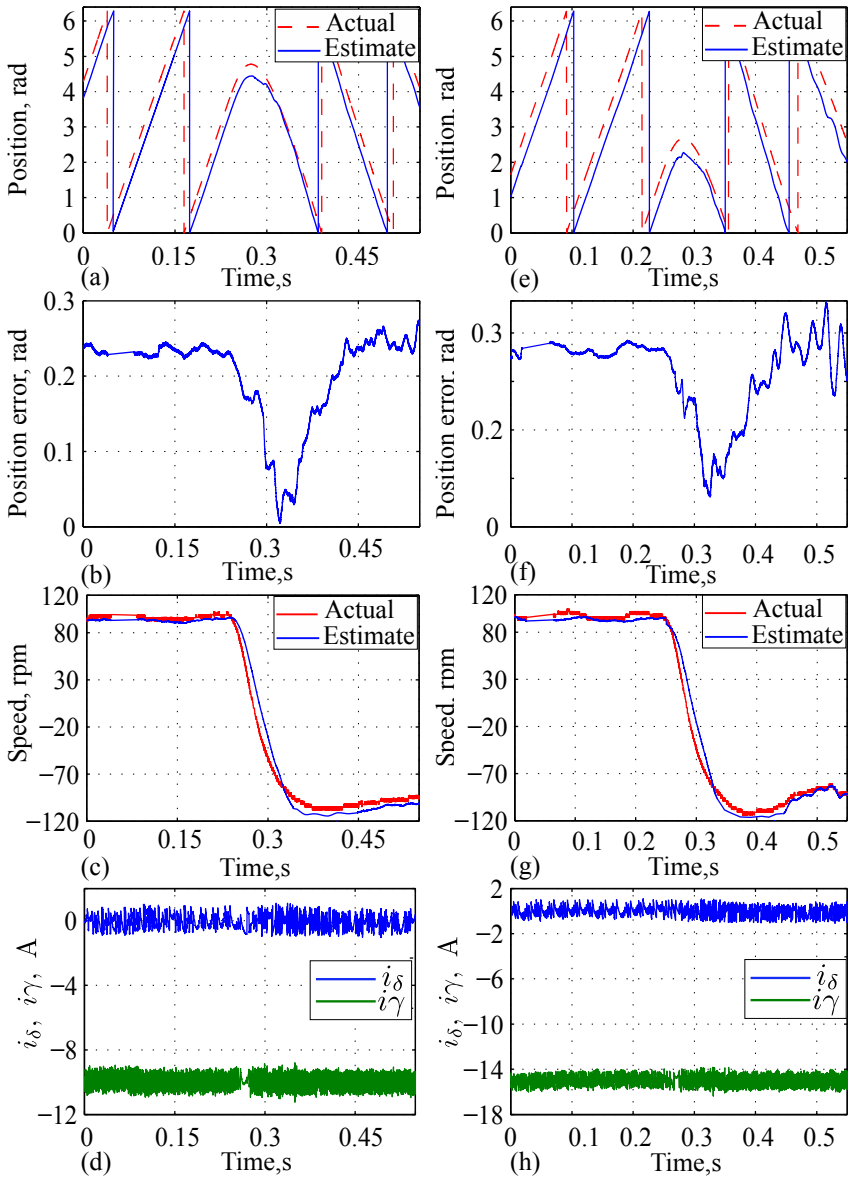

Figure 6.10: Experimental speed reversal performance of sensorless FCSMPC at 100 rpm: (a)-(d) at the full rated load, and (e)-(h) at 150% of the rated load.

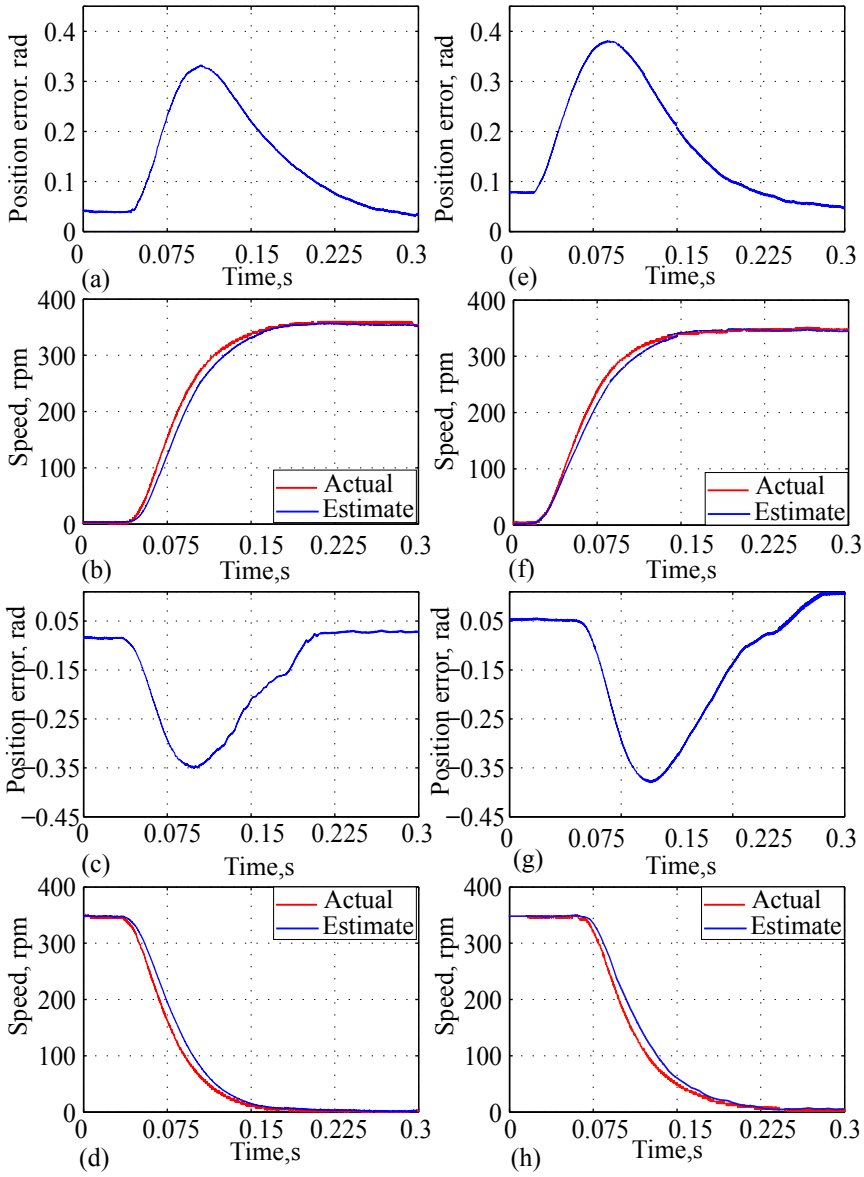

Figure 6.11: Experimental speed sweep performance from 0 rpm to half the rated speed (350 rpm) and back at 25% rated load: (a)-(d) for sensorless FCSMPC, and (e)-(h) for sensorless vector control.

6.6.3 Torque Transient Performance

The torque reversal tests are conducted to validate the transient performance of the nonlinear optimization based sensorless FCSMPC for the large torque variations. The tests results at 100 rpm and the full rated load for the FCSMPC are compared with the vector control in Fig. 6.12. The steady state position error for the FCSMPC is close to the vector control. The reduction in position error due to high back emf for the vector control at the half rated load as shown in Fig. 6.8 (f) is not observed for the full load. The high current associated with the full rated load surpasses the influence of high back emf. The position errors at the transient state for the FCSMPC and the vector control are also very close except 0.05 rad reduction in peak value for the FCSMPC.

The summary of the important experimental results are provided in Table II for both nonlinear optimization based FCSMPC and vector control.

Table 6.1: Summary of Experimental Results

Operating conditions	Steady state position error (rad)		Maximum transient state position error (rad)		Response time (s)	
	FCSMPC	Vector	FCSMPC	Vector	FCSMPC	Vector
No load[1]	0.03	0.075	-	-	-	-
Speed reversal[2]	0.125	0.08	0.25	0.32	0.18	0.18
Speed sweep[3]	0.03	0.075	0.32	0.38	0.24	0.27
Torque reversal[4]	0.23	0.23	0.25	0.25	0.36	0.45

1: 50 rpm, 2: 100 rpm and 50% rated load, 3: 0 rpm to 350 rpm at 25% rated load, 4: 100 rpm with rated load.

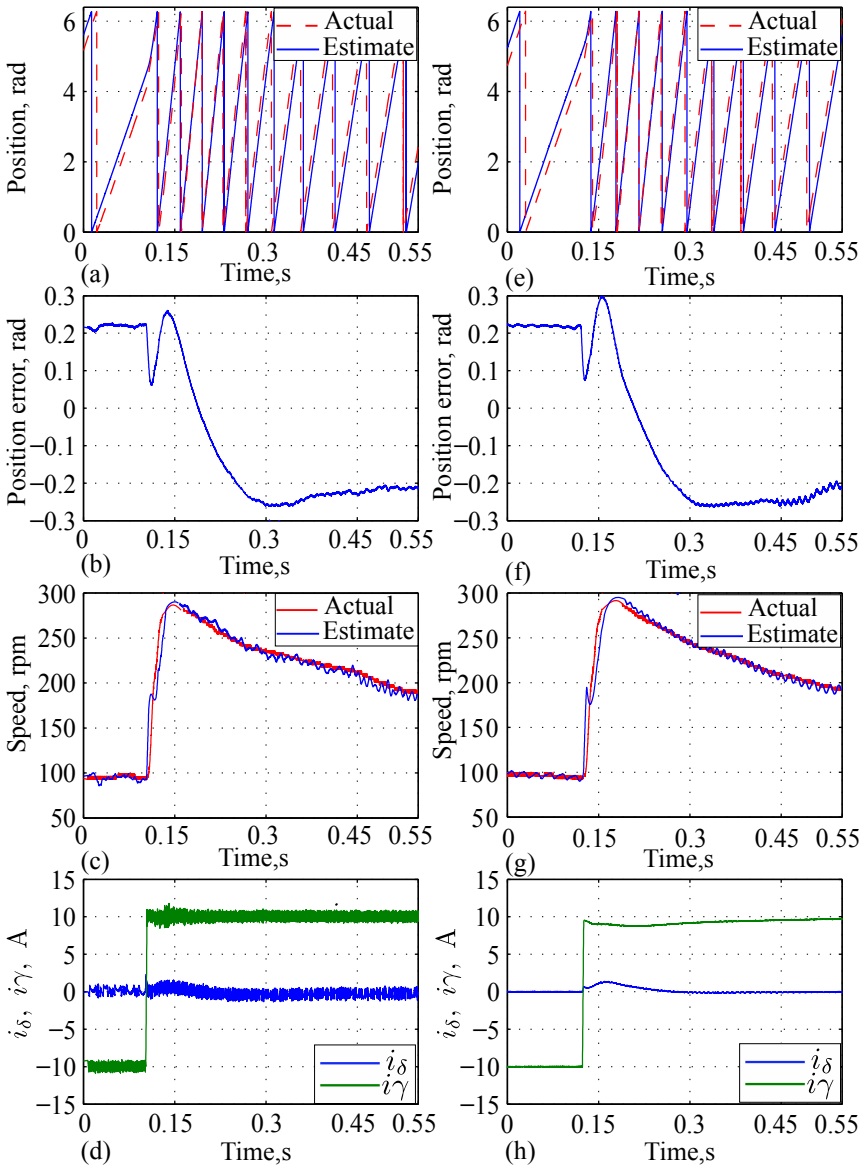

Figure 6.12: Experimental torque reversal performance at the full rated torque and 100 rpm: (a)-(d) for sensorless FCSMPC, and (e)-(h) for sensorless vector control.

6.6.4 Parameter Sensitivity Analysis

The nominal motor parameter values (see Table I) are supplied to this nonlinear optimization based sensorless scheme. Therefore, the variation of the physical parameters

from the nominal values can affect the accuracy of the estimated position and speed. Only the sign of the optimal speed ($\hat{\omega}_o$) is required in this sensorless scheme (to perform the compensation at standstill) and hence its accuracy with respect to the parameter variations is not presented here. The position error with respect to the variations in the parameters is presented in Fig. 6.13 for 100 rpm with torque reversal at half the rated load. These variations are made on the nominal values supplied to the cost function to mimic the difference between the model and physical values with the actual parameter variations. The variations from the nominal values in resistance and permanent magnet flux linkage by $\pm$ 50% and $\pm$ 25% respectively do not have any significant effects on the position error as shown in Fig. 6.13 (a) and (c) respectively. The effect of a decrease in d axis inductance by 25% is negligible whereas an increase by 25% rises the position error by 0.025 rad with respect to the nominal case as shown in Fig. 6.13 (b). The decrease by 25% in q axis inductance increases the position error by 0.05 rad from the nominal case while the increase by 25% results in large oscillations apart from 0.025 rad decrease from the nominal case as shown in Fig. 6.13 (d). The variation in q axis inductance has the most considerable impacts on the position error as compared to other parameters. However, the position estimation by nonlinear optimization shows robustness with these large parameter variations.

6.7 Summary

This chapter presents the nonlinear optimization based position and speed estimation scheme for IPMSM drive with FCSMPC. It shows that the proposed method is an ideal solution for the drives with arbitrary signal injection- a case for FCMPC. The compensator is proposed based on the characteristics of the cost function to correct

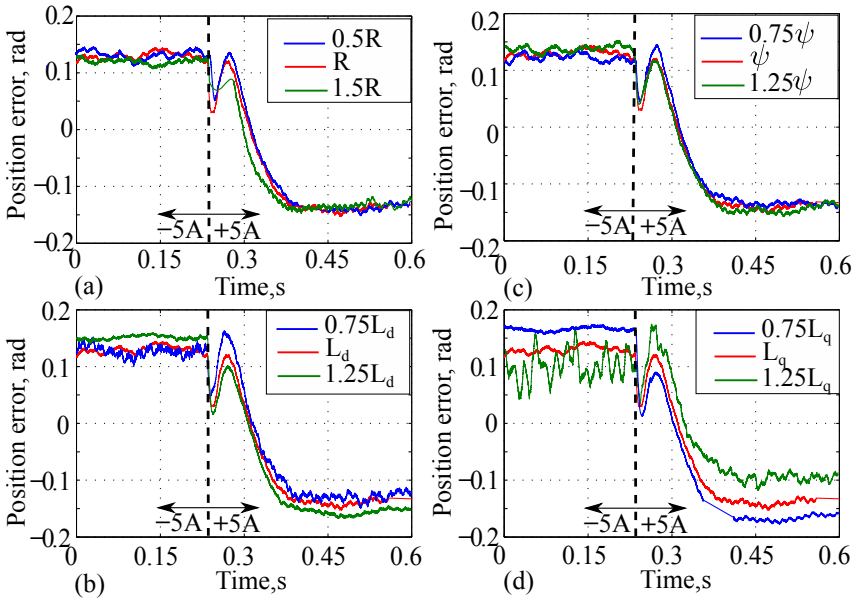

Figure 6.13: Position error with respect to parameter variations: (a) ±50% variation in resistance, (b) ±25% variation in d axis inductance, (c) ±25% variation in permanent magnet flux linkage, and (d) ±25% variation in q axis inductance.

the wrong convergences to the saddle and symmetrical solutions. The experimental results are promising and those are in par with the vector control with the same sensorless scheme. There is an improvement in steady state position error (by 0.045 rad) at standstill as compared to the vector control attributed to the strong switching ripples associated with FCSMPC. However, the performance of the sensorless FCSMPC deteriorates at medium speed with load (0.06 rad rise in position error) as the high switching ripples intensify the effect of inductance variation by saturation. Moreover, the proposed sensorless scheme for FCSMP performs superior as compared to other model based techniques in literature for model predictive controls. The proposed scheme has very low steady state position oscillations about ±0.025 rad and the position error is 0.03 rad at no load and 0.225 rad at the full rated load.

Chapter 7

Co-estimation of Position and Parameters for Robust Sensorless Control

7.1 Introduction

This chapter presents a single nonlinear optimization based observer which simultaneously estimates both position, and d and q inductances at every sampling interval to realize robust sensorless FCSMPC for the reference IPMSM. The voltage vector injections by FCSMPC establish persistent excitation and enable simultaneous identification at wide operating region, however, it limits employing standard techniques for position estimation. The proposed method is suitable for any type of signal injection and hence an ideal candidate for FCSMPC. This chapter also presents detailed robustness and convergence analyzes. Finally, the performance of the proposed robust sensorless control scheme is verified experimentally at different operating conditions.

7.2 Robust Sensorless FCSMPC Scheme

In robust sensorless FSCMPC scheme, position and machine parameters are simultaneously estimated so that the effect of the corresponding parameter variations can be effectively eliminated in the estimation of the position. Moreover, the vector injection by FCSMPC establishes PE that helps in simultaneous identification of both position and parameters at wide operating region. The complete block diagram of the robust sensorless FCSMPC scheme is depicted in Fig. 7.1. The scheme consists of the nonlinear optimization based estimator which provides estimated position ($\hat{\theta}$) and the estimated inductances $\hat{L}_d$ and $\hat{L}_q$ to FCSMPC. The inductances $\hat{L}_d$ and $\hat{L}_q$ are the most influencing parameters on the accuracy of the position estimation according to the experimental results in section 6.6.4 and the robustness analysis in section 7.3. The estimated position is the output of the standard PLL which has the input $\hat{\vartheta}$ (angle difference between $\delta\gamma$ and dq frames) from the nonlinear optimizer as shown in Fig. 7.2. The estimated speed $\hat{\omega}$ is the output of the filter. The FCSMPC in section 4.4 is employed for robust sensorless FSCMPC scheme presented in this section.

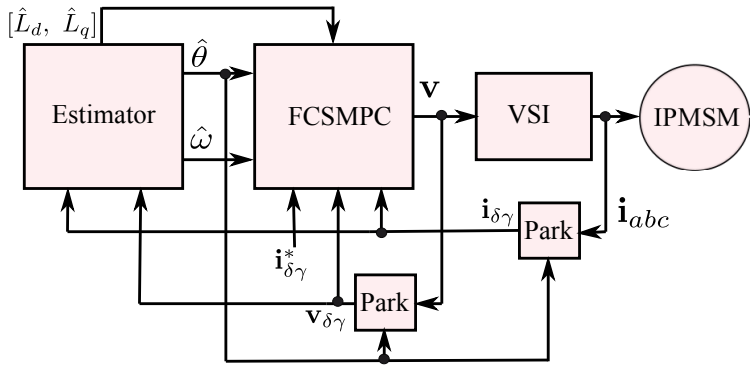

Figure 7.1: The block diagram of the robust sensorless FCSMPC scheme.

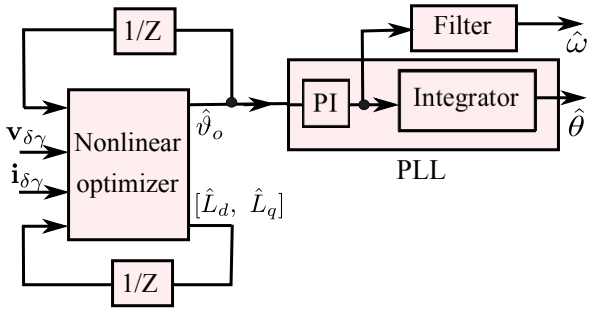

Figure 7.2: Nonlinear optimization based robust position and parameter estimation.

7.3 Robustness Analysis

The equation (2.13) is expressed as the function of unknown vector $\mathbf{x} \in \mathbb{R}^n$ where n is the length of $\mathbf{x}$, and $\mathbf{x}$ consists of states ($\hat{\vartheta}$ and/or $\hat{\omega}$)

$$\mathbf{h}(\mathbf{x}) = \tilde{\mathbf{v}}_{\delta\gamma} - \mathbf{L}_{\delta\gamma}\dot{\mathbf{i}}_{\delta\gamma} - \mathbf{T}_r\mathbf{L}_{\delta\gamma}\hat{\omega}\mathbf{i}_{\delta\gamma} - \hat{\omega}\psi_m\tilde{\mathbf{q}}. \tag{7.1}$$

The cost function for the nonlinear optimization is defined as the square of the two norm of (7.1).

$$f(\mathbf{x}) = \|\mathbf{h}(\mathbf{x})\|^2 \tag{7.2}$$

In the optimization process, the function (7.2) is minimized with respect to the unknown vector $\mathbf{x}$.

$$\underset{\mathbf{x}}{\text{minimize}} f(\mathbf{x}).$$

The parameters in (7.1) are expressed as the nominal and Δ variations from the nominal as

$$\begin{cases} L_d = \bar{L}_d + \Delta_{\bar{L}_d} \quad L_q = \bar{L}_q + \Delta_{\bar{L}_q} \\ R = \bar{R} + \Delta_{\bar{R}} \quad \psi_m = \bar{\psi_m} + \Delta_{\bar{\psi_m}} \end{cases} \tag{7.3}$$

where $^-$ stands for the nominal. By substituting (7.3) into (7.1), the function corresponding to the nominal parameters and for their variations can be separated as

$$\mathbf{h}(\mathbf{x}) = \bar{\mathbf{h}}(\mathbf{x}) + \Delta_{\bar{\mathbf{h}}(\mathbf{x})} \tag{7.4}$$

where $\bar{\mathbf{h}}(\mathbf{x})$ and $\Delta_{\bar{\mathbf{h}}(\mathbf{x})}$ are the functions of the nominal parameters and Δ variations from the nominal parameters respectively, and

$$\begin{cases} \bar{\mathbf{h}}(\mathbf{x}) = \bar{\mathbf{v}}_{\delta\gamma} - \bar{\mathbf{L}}_{\delta\gamma}\dot{\mathbf{i}}_{\delta\gamma} - \mathbf{T}\bar{\mathbf{L}}_{\delta\gamma}\hat{\omega}\mathbf{i}_{\delta\gamma} - \hat{\omega}\bar{\psi_m}\tilde{\mathbf{q}} \\ \Delta_{\bar{\mathbf{h}}(\mathbf{x})} = \Delta_{\bar{\mathbf{v}}_{\delta\gamma}} - \Delta_{\mathbf{L}_{\delta\gamma}}\dot{\mathbf{i}}_{\delta\gamma} - \mathbf{T}\Delta_{\mathbf{L}_{\delta\gamma}}\hat{\omega}\mathbf{i}_{\delta\gamma} - \hat{\omega}\Delta_{\bar{\psi_m}}\tilde{\mathbf{q}} \end{cases}$$

where $\bar{\mathbf{v}}_{\delta\gamma} = \mathbf{v}_{\delta\gamma} - \bar{R}\mathbf{i}_{\delta\gamma}$, $\Delta_{\bar{\mathbf{v}}_{\delta\gamma}} = -\Delta_{\bar{R}}\mathbf{i}_{\delta\gamma}$, $\mathbf{L}_{\delta\gamma} = \tilde{\mathbf{P}}\bar{L}_\Delta + \bar{L}_\Sigma\mathbf{I}$, $\bar{L}_\Delta = \frac{\bar{L}_d - \bar{L}_q}{2}$, $\bar{L}_\Sigma = \frac{\bar{L}_d + \bar{L}_q}{2}$, $\Delta_{\mathbf{L}_{\delta\gamma}} = \tilde{\mathbf{P}}\Delta_{\bar{L}_\Delta} + \Delta_{\bar{L}_\Sigma}\mathbf{I}$, $\Delta_{\bar{L}_\Delta} = \frac{\Delta_{\bar{L}_d} - \Delta_{\bar{L}_q}}{2}$, and $\Delta_{\bar{L}_\Sigma} = \frac{\Delta_{\bar{L}_d} + \Delta_{\bar{L}_q}}{2}$. Similarly, the cost function (7.2) is also decomposed for the nominal parameters and their variations as

$$f(\mathbf{x}) = \|\bar{\mathbf{h}}(\mathbf{x})\|^2 + 2\Delta'_{\bar{\mathbf{h}}(\mathbf{x})}\bar{\mathbf{h}}(\mathbf{x}) + \|\Delta_{\bar{\mathbf{h}}(\mathbf{x})}\|^2 \tag{7.5}$$

The optimization of the cost function (7.5) results in the correct optimal solution $\mathbf{x}_o$ as it considers the parameter variations. If only nominal parameters are considered, then the cost function (7.5) becomes

$$\bar{f}(\mathbf{x}) = \|\bar{\mathbf{h}}(\mathbf{x})\|^2 \tag{7.6}$$

and therefore the optimization of (7.6) produces error in the solution

$$\Delta_{\mathbf{x_o}} = \mathbf{x}_o - \bar{\mathbf{x}}_o \tag{7.7}$$

where $\bar{\mathbf{x}}_o$ is the solution of (7.6). At $\mathbf{x} = \bar{\mathbf{x}}_o$,

$$f(\bar{\mathbf{x}}_o) = \|\Delta_{\bar{\mathbf{h}}(\bar{\mathbf{x}}_\mathbf{o})}\|^2 \text{ as } \bar{\mathbf{h}}(\bar{\mathbf{x}}_o) = 0$$

Therefore, the region of confidence $\mathscr{D}$ is defined as

$$\mathscr{D} = \{\mathbf{x} \in \mathbb{R}^n \mid f(\mathbf{x}) \leq \|\Delta_{\bar{\mathbf{h}}(\bar{\mathbf{x}}_o)}\|^2\} \tag{7.8}$$

where the correct optimal solution $\mathbf{x_o}$ exists with an assumption that $\mathscr{D}$ is convex. The solution without considering the parameter variations $\bar{\mathbf{x}}_\mathbf{o}$ lies in the border of $\mathscr{D}$. Therefore, it can be inferred that if $\mathscr{D}$ is bounded then the position error is also bounded.

The region $\mathscr{D}$ is analyzed graphically for the two cases $\mathbf{x} = [\hat{\vartheta}, \hat{\omega}]'$ and $\mathbf{x} = \hat{\vartheta}$ in Fig. 7.3 for the extreme parameter variations: $\Delta_{\bar{L}_d} = \pm 0.25\bar{L}_d$, $\Delta_{\bar{L}_q} = \pm 0.25\bar{L}_q$, $\Delta_{\bar{R}} = \pm 0.5\bar{R}$, and $\Delta_{\bar{\psi}} = \pm 0.25\bar{\psi}$ for the reference machine. The details of the reference machine, the nominal parameters and the inductance profile are provided in Appendix B. For $\mathbf{x} = [\hat{\vartheta}, \hat{\omega}]'$, $\mathscr{D}$ is an ellipse, and for $\mathbf{x} = \hat{\vartheta}$, it is a straight line. Fig. 7.3 also shows the trajectories of the solution moving from $\bar{\mathbf{x}}_\mathbf{o}$ to $\mathbf{x_o}$ by adding the parameter variations to the cost function (7.5) in the steps of 2.5%. It should be noted that trajectories are bounded inside the region $\mathscr{D}$.

For $\mathbf{x} = [\hat{\vartheta},\ \hat{\omega}]'$, $\pm 25\%$ variations in ψ show significant error in the solution for both $\hat{\omega}$ and $\hat{\vartheta}$ at the rated speed (366 rad/s), the rated current ($\mathbf{i}_{\delta\gamma} = [-10\text{A},\ 10A]'$), and with rate of change of current $\dot{\mathbf{i}}_{\delta\gamma} = [10^4\text{A/s}, 10^4\text{A/s}]'$ as shown in Fig. 7.3 (a). It should be noted that for FCSMPC, it is always true that $\dot{\mathbf{i}}_{\delta\gamma} \neq 0$ due to the voltage vector injection. The error is {134 rad/s, -116 rad/s} and {-0.9 rad, 0.22 rad}

respectively for $\hat{\omega}$ and $\hat{\vartheta}$. For $\mathbf{x} = \hat{\vartheta}$, the error in solution of $\hat{\vartheta}$ is substantially reduced to $\{-0.024$ rad, 0.019 rad$\}$ at the same condition as shown in Fig. 7.3 (c). This is due to the fact that, $\hat{\vartheta}$ is affected by both estimation error in $\hat{\omega}$ and parameter variation in ψ for $\mathbf{x} = [\hat{\vartheta},\ \hat{\omega}]'$ case whereas only the latter influences $\mathbf{x} = \hat{\vartheta}$. The variations in L_d by $\pm 25\%$ result in the solution error of $\{49$ rad/s, -41 rad/s$\}$ and $\{-0.06$ rad, 0.05 rad$\}$ for $\mathbf{x} = [\hat{\vartheta},\ \hat{\omega}]'$ as shown in Fig. 7.3 (a) whereas the error in $\hat{\vartheta}$ is within 0.01 rad for $\mathbf{x} = \hat{\vartheta}$ (not shown in the Fig. 7.3 (c) as the value is small). The variations in L_q by $\pm 25\%$ result in similar errors in $\hat{\vartheta}$ for both $\mathbf{x} = [\hat{\vartheta},\ \hat{\omega}]'$ and $\mathbf{x} = \hat{\vartheta}$ cases ($\{-0.09$ rad, 0.08 rad$\}$). The variations in resistance by $\pm 50\%$ is least significant for both $\mathbf{x} = [\hat{\vartheta},\ \hat{\omega}]$ and $\mathbf{x} = \hat{\vartheta}$, and the error in $\hat{\vartheta}$ is within 0.01 rad (not shown in Fig. 7.3 (c)). The strong back emf at 366 rad/s and $\dot{\mathbf{i}}_{\delta\gamma} = [10^4\text{A/s}, 10^4\text{A/s}]'$ reduce the effects by variations in resistance.

At zero speed, $\mathbf{i}_{\delta\gamma} = [-10\text{A},\ 10A]'$, and $\dot{\mathbf{i}}_{\delta\gamma} = [10^4\text{A/s}, 10^4\text{A/s}]'$, the error in solution by $\pm 25\%$ variations in L_d for $\mathbf{x} = [\hat{\vartheta},\ \hat{\omega}]'$ is $\{-10$ rad/s, 90 rad/s$\}$ and $\{-0.69$ rad, 0.48 rad$\}$ as shown in Fig. 7.3 (b). On the other hand, the error in $\hat{\vartheta}$ is reduced (0.2 rad) for $\mathbf{x} = \hat{\vartheta}$ for -25% variation as shown in Fig. 7.3 (d) whereas, for $+25\%$, the error is as same as the case of $\mathbf{x} = [\hat{\vartheta},\ \hat{\omega}]'$. Similarly, for the variation in L_q by $\pm 25\%$, the error in $\hat{\vartheta}$ is reduced from 1 rad to 0.8 rad for the case of $\mathbf{x} = \hat{\vartheta}$ as compared to $\mathbf{x} = [\hat{\vartheta},\ \hat{\omega}]'$. The variation in ψ does not have effects in the solution as speed is zero for both $\mathbf{x} = [\hat{\vartheta},\ \hat{\omega}]'$ and $\mathbf{x} = \hat{\vartheta}$ cases. The variations in resistance by $\pm 50\%$ result error in $\hat{\vartheta}$ as low as 0.005 rad (not shown in Fig. 7.3(b) and (d)) as there is a strong current derivative term $\dot{\mathbf{i}}_{\delta\gamma} = [10^4\text{A/s}, 10^4\text{A/s}]'$.

From the robustness analysis presented in this section, it is found that the case $\mathbf{x} = \hat{\vartheta}$ is more robust towards the parameter variations as compared to $\mathbf{x} = [\hat{\vartheta},\ \hat{\omega}]'$.

Moreover, the main influencing parameters are only L_d and L_q for $\mathbf{x} = \hat{\vartheta}$. The inverter voltage drop by dead-time varies with switching frequency and it is not considered in this thesis as the switching frequency of FCSMPC is much lower as compared to the fixed switching frequency (about 10 kHz) of a typical vector control. The switching frequency of the FCSMPC implemented in this thesis varies from 15Hz to 500Hz respectively from standstill to the rated speed operations. The explicit treatment of the cross-saturation by mutual inductances in position estimation showed some benefits in literature (Zhu *et al.*, 2007), however implicit treatment considering only self inductances is preferred in this thesis as the reference machine has low saliency ($L_q/L_d = 1.3$), and also to reduce the complexity in the structure of the observer. Consequently, this thesis proposes nonlinear optimization based scheme for estimating $\hat{\vartheta}$ along with L_d and L_q to realize robust sensorless FCSMPC.

7.4 Convergence Analysis

This thesis proposes the estimation of unknown vector $\mathbf{x} = [\hat{\vartheta},\ \hat{L}_d,\ \hat{L}_q]$ where $\hat{}$ represents the estimated value, and the corresponding updated cost function is

$$f(\mathbf{x}) = \|\mathbf{h}(\mathbf{x})\|^2 + [\mathbf{x} - \mathbf{x}_i]' \mathbf{I}_\kappa [\mathbf{x} - \mathbf{x}_i]. \tag{7.9}$$

where $\mathbf{I}_\kappa = [[\kappa_1, 0, 0]', [0, \kappa_2, 0]', [0, 0, \kappa_3]']$, κ_1, κ_2 and κ_3 are the regularization constants, and $\mathbf{x}_i = [\hat{\vartheta}_i, \hat{L}_{di}, \hat{L}_{qi}]'$, is the initial value or the solutions from $(k-1)^{th}$ sample. In (7.9), h(x) is given by (7.1) where $\mathbf{i}_{\delta\gamma}$ is from current sensor measurement, $\mathbf{v}_{\delta\gamma}$ is the reference value, $\dot{\mathbf{i}}_{\delta\gamma} = (\mathbf{i}_{\delta\gamma k} - \mathbf{i}_{\delta\gamma k-1})/T_s$, where k is sampling index and T_s is the sampling interval, R and ψ_m are the nominal values, $\hat{\omega}$ is from PLL output,

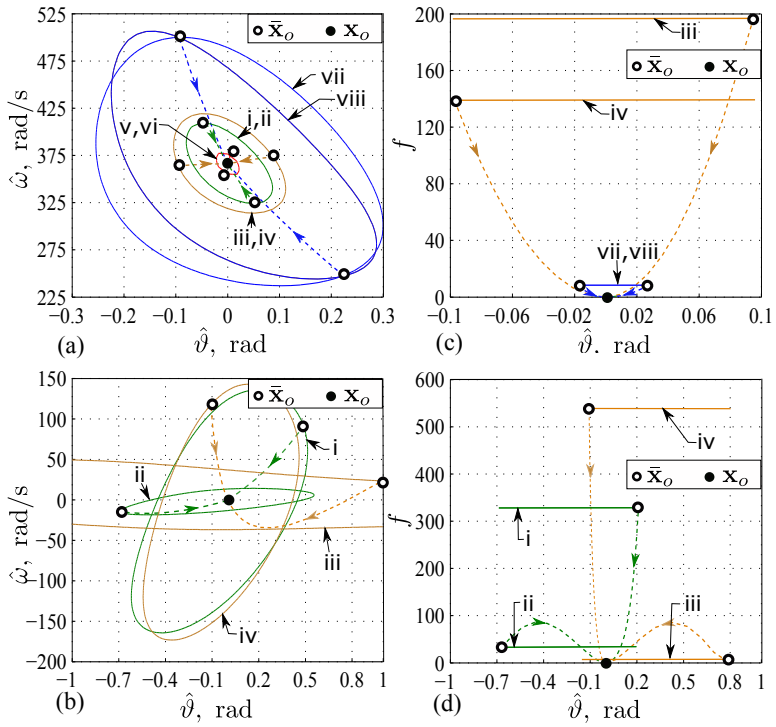

Figure 7.3: The region $\mathscr{D}$ (i, ii, iii, iv, v, vi, vii, and viii for $\mp 0.25\bar{L}_d$, $\mp 0.25\bar{L}_q$, $\mp 0.5\bar{R}$, and $\mp 0.25\bar{\psi}$ respectively), and the trajectories of $\bar{x}_o$ moving into x_o: at rated speed, $\mathbf{i}_{\delta\gamma} = [-10\text{A}, 10\text{A}]'$, and $\dot{\mathbf{i}}_{\delta\gamma} = [10^4\text{A/s}, 10^4\text{A/s}]'$ (a) for $\mathbf{x} = [\hat{\vartheta}, \hat{\omega}]'$ and (c) for $\mathbf{x} = \hat{\vartheta}$, and at zero speed, $i_{\delta\gamma} = [-10\text{A}, 10\text{A}]'$ and $\dot{\mathbf{i}}_{\delta\gamma} = [10^4\text{A/s}, 10^4\text{A/s}]'$ (b) for $\mathbf{x} = [\hat{\vartheta}, \hat{\omega}]'$ and (d) for $\mathbf{x} = \hat{\vartheta}$ ($\bar{\mathbf{x}}_o$ on RHS and LHS of $\hat{\vartheta} = 0$ axis corresponds to decrement and increment in parameter variations respectively).

and $\hat{\vartheta}$, $\hat{L}_d$, $\hat{L}_q$ are the estimation.

The regularization terms are added to reduce the ripples in the estimation due to noise and delays in the current measurement, and also to stabilize the cost function from near singularity. Without regularization terms especially for $\hat{L}_d$ and $\hat{L}_q$, the Hessian of $\|\mathbf{h}(\mathbf{x})\|^2$ becomes close to singular as the second order derivatives with respect to L_d and L_q are 10^3 times more than that of $\hat{\vartheta}$. Moreover, the cost function also becomes singular due to nonobservability for a short time period at the transient operation as mentioned in section 4.5. The large values of κ_2 and κ_3 can result in

wrong $\hat{\vartheta}$ as it decouples with $\hat{L}_d$ and $\hat{L}_q$ estimation, and therefore their values are tuned between stable and robust position estimation.

The cost function f at rated speed, $\mathbf{i}_{\delta\gamma} = [-10\text{A}, 10\text{A}]'$ and $\dot{\mathbf{i}}_{\delta\gamma} = [10^4\text{A/s}, 10^4\text{A/s}]'$, and at zero speed, $\mathbf{i}_{\delta\gamma} = [-10\text{A}, 10\text{A}]'$ and $\dot{\mathbf{i}}_{\delta\gamma} = [10^4\text{A/s}, 10^4\text{A/s}]'$ are shown in Fig. 7.4 (a)-(c) and (b)-(d) respectively. In (a) and (b), $\mathbf{x} = \hat{\vartheta}$ is varied by keeping $\hat{L}_d$ and $\hat{L}_q$ as constants (nominal values), and in (c) and (d), $\mathbf{x} = [\hat{L}_d,\ \hat{L}_q]'$ is varied by keeping the actual value of $\hat{\vartheta}$ (0 rad). It is shown that value of the cost is zero at the actual value $\mathbf{x}_o$ (optimal solution). In (b), there are two minimums as compared to (a) as the effect of rotor saliency dominates at zero (and at low) speed.

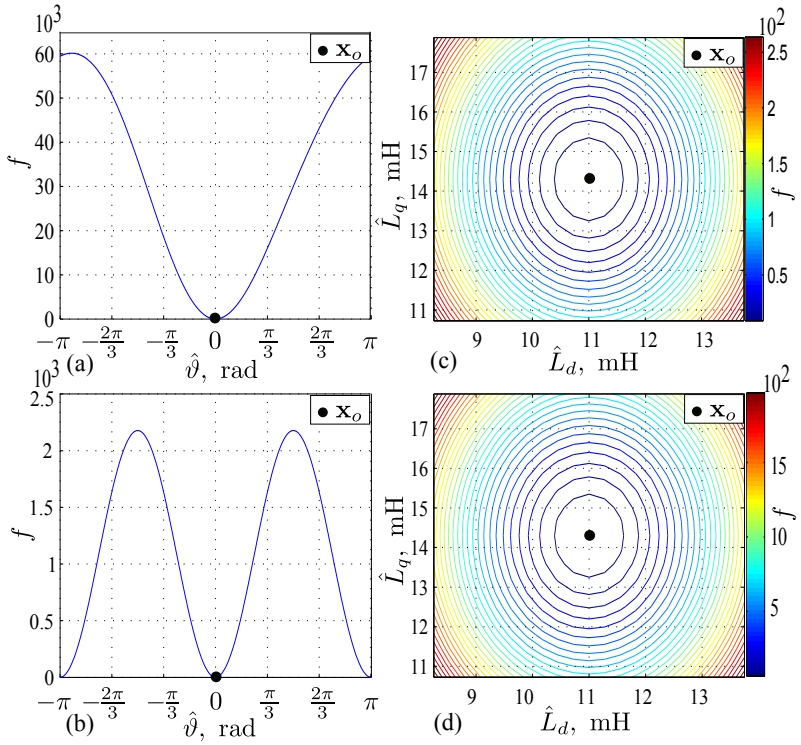

Figure 7.4: The cost function at rated speed, $\mathbf{i}_{\delta\gamma} = [-10\text{A}, 10\text{A}]'$, and $\dot{\mathbf{i}}_{\delta\gamma} = [10^4\text{A/s}, 10^4\text{A/s}]'$ (a) with respect to $\hat{\vartheta}$ keeping $\hat{L}_d = \bar{L}_d$ and $\hat{L}_q = \bar{L}_q$, and (c) with respect to $\hat{L}_d$ and $\hat{L}_q$ keeping $\hat{\vartheta} = 0$ rad, and similarly at zero speed, $\mathbf{i}_{\delta\gamma} = [-10\text{A}, 10\text{A}]'$ and $\dot{\mathbf{i}}_{\delta\gamma} = [10^4\text{A/s}, 10^4\text{A/s}]'$ in (b) and (d) respectively.

There exists a global minimum if the cost function is convex and the solution converges to this minimum as long as the convergence trajectory is confined within the convex region (Epelman, 2007). Therefore, analyzing the convex region is the fundamental part of the convergence analysis. One of the approaches to find the convex region of the cost function is with the help of the leading principal minors of its Hessian matrix (Erikson, 2010). The Hessian of the cost function (7.9) is

$$\mathbf{H} = 2\begin{bmatrix} \mathbf{h}'\mathbf{h}_{\hat{\vartheta}\hat{\vartheta}} + \|\mathbf{h}_{\hat{\vartheta}}\|^2 + \kappa_1, & \mathbf{h}'\mathbf{h}_{\hat{\vartheta}\hat{L}_d} + \mathbf{h}'_{\hat{\vartheta}}\mathbf{h}_{\hat{L}_d}, & \mathbf{h}'\mathbf{h}_{\hat{\vartheta}\hat{L}_q} + \mathbf{h}'_{\hat{\vartheta}}\mathbf{h}_{\hat{L}_q} \\ \mathbf{h}'\mathbf{h}_{\hat{\vartheta}\hat{L}_d} + \mathbf{h}'_{\hat{\vartheta}}\mathbf{h}_{\hat{L}_d}, & \|\mathbf{h}_{\hat{L}_d}\|^2 + \kappa_2, & \mathbf{h}'_{\hat{L}_d}\mathbf{h}'_{\hat{L}_q} \\ \mathbf{h}'\mathbf{h}_{\hat{\vartheta}\hat{L}_q} + \mathbf{h}'_{\hat{\vartheta}}\mathbf{h}_{\hat{L}_q}, & \mathbf{h}'_{\hat{L}_d}\mathbf{h}'_{\hat{L}_q}, & \|\mathbf{h}_{\hat{L}_q}\|^2 + \kappa_3 \end{bmatrix} \tag{7.10}$$

where single and double subscripts of $\mathbf{h}$ indicates the first and second order derivatives respectively and their expressions are

$$\begin{aligned}
\mathbf{h}_{\hat{\vartheta}} &= 2L_{\Delta}\mathbf{T}(\tilde{\mathbf{P}}\dot{\mathbf{i}}_{\delta\gamma} + \mathbf{T}\tilde{\mathbf{P}}\hat{\omega}\mathbf{i}_{\delta\gamma}) + \psi_m\hat{\omega}\mathbf{T}\tilde{\mathbf{q}} \\
\mathbf{h}_{\hat{\vartheta}\hat{\vartheta}} &= 2\mathbf{T}\mathbf{h}_{\hat{\vartheta}} \\
\mathbf{h}_{\hat{L}_d} &= 1/2((\mathbf{I} + \tilde{\mathbf{P}})\dot{\mathbf{i}}_{\delta\gamma} + \mathbf{T}(\mathbf{I} + \tilde{\mathbf{P}})\hat{\omega}\mathbf{i}_{\delta\gamma}) \\
\mathbf{h}_{\hat{L}_q} &= 1/2((\mathbf{I} - \tilde{\mathbf{P}})\dot{\mathbf{i}}_{\delta\gamma} + \mathbf{T}(\mathbf{I} - \tilde{\mathbf{P}})\hat{\omega}\mathbf{i}_{\delta\gamma}) \\
\mathbf{h}_{\hat{\vartheta}\hat{L}_d} &= \mathbf{T}\tilde{\mathbf{P}}\dot{\mathbf{i}}_{\delta\gamma} + \mathbf{T}\mathbf{T}\tilde{\mathbf{P}}\hat{\omega}\mathbf{i}_{\delta\gamma} \\
\mathbf{h}_{\hat{\vartheta}\hat{L}_q} &= -\mathbf{T}\tilde{\mathbf{P}}\dot{\mathbf{i}}_{\delta\gamma} - \mathbf{T}\mathbf{T}\tilde{\mathbf{P}}\hat{\omega}\mathbf{i}_{\delta\gamma}
\end{aligned}$$

and the Jacobian is

$$\mathbf{J} = 2\mathbf{h}'[\mathbf{h}_{\hat{\vartheta}}, \mathbf{h}_{\hat{L}_d}, \mathbf{h}_{\hat{L}_q}] + 2[\mathbf{x} - \mathbf{x}_i]'\mathbf{I}_{\kappa} \tag{7.11}$$

The Hessian (7.10) has three leading principle minors

$$\mathbf{m} = [H(1,1), |H([1,2],[1,2])|, |H|]' \tag{7.12}$$

and the conditions for the convexity are (Erikson, 2010)

$$\mathbf{m} > [0,0,0]' \tag{7.13}$$

It is challenging to derive analytical expressions for these conditions. Therefore, the convex boundaries are found by solving the function $\|\mathbf{m}\|^2 = 0$ with the help of Matlab's numerical solver 'fsolve'. The results for the rated speed, $\mathbf{i}_{\delta\gamma} = [-10\text{A}, 10\text{A}]'$ and $\dot{\mathbf{i}}_{\delta\gamma} = [10^4\text{A/s}, 10^4\text{A/s}]'$, and for zero speed, $\mathbf{i}_{\delta\gamma} = [-10\text{A}, 10\text{A}]'$ and $\dot{\mathbf{i}}_{\delta\gamma} = [10^4\text{A/s}, 10^4\text{A/s}]'$ are shown in Fig. **??** (a) and (b) respectively. The region satisfying $\mathbf{m} > [0,0,0]'$ within the boundary is essentially the convex region.

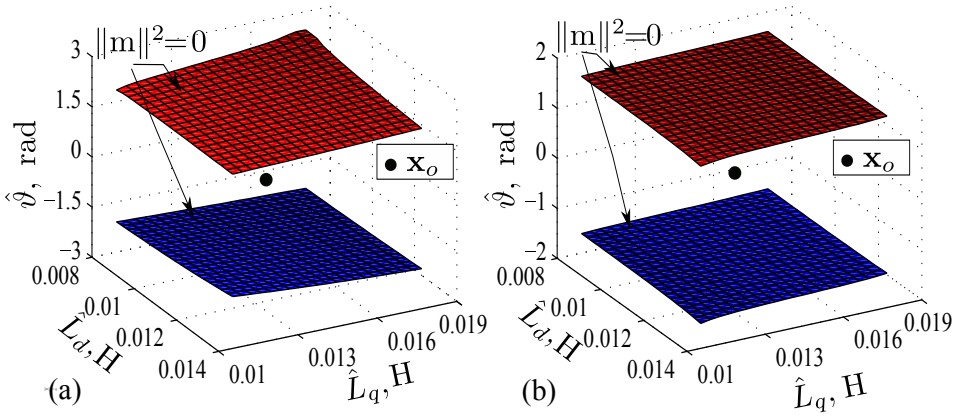

Figure 7.5: The convex region within the boundaries of $\|\mathbf{m}\|^2 = 0$ for (a) the rated speed, $\mathbf{i}_{\delta\gamma} = [-10\text{A}, 10\text{A}]'$ and $\dot{\mathbf{i}}_{\delta\gamma} = [10^4\text{A/s}, 10^4\text{A/s}]'$, and (b) zero speed, $\mathbf{i}_{\delta\gamma} = [-10\text{A}, 10\text{A}]'$ and $\dot{\mathbf{i}}_{\delta\gamma} = [10^4\text{A/s}, 10^4\text{A/s}]'$.

This thesis employs Newton minimization along with golden-section line search

to optimize the cost function (7.9) with respect to $\mathbf{x} = [\hat{\vartheta}, \hat{L}_d, \hat{L}_q]'$. The details of the Newton method is provided in section 6.2. The trajectories of $\mathbf{x} = [\hat{\vartheta}, \hat{L}_d, \hat{L}_q]'$ and $\|\mathbf{J}\|$ with respect to Newton iterations for the rated speed, $\mathbf{i}_{\delta\gamma} = [-10\text{A}, 10\text{A}]'$ and $\dot{\mathbf{i}}_{\delta\gamma} = [10^4\text{A/s}, 10^4\text{A/s}]'$, and for zero speed, $\mathbf{i}_{\delta\gamma} = [-10\text{A}, 10\text{A}]'$ and $\dot{\mathbf{i}}_{\delta\gamma} = [10^4\text{A/s}, 10^4\text{A/s}]'$ are shown in Fig. 7.6 (a)-(b) and (c)-(d) respectively. The intermediate iterations by line search is omitted from showing in the figure. The iterations converge within 6 iterations for both the cases.

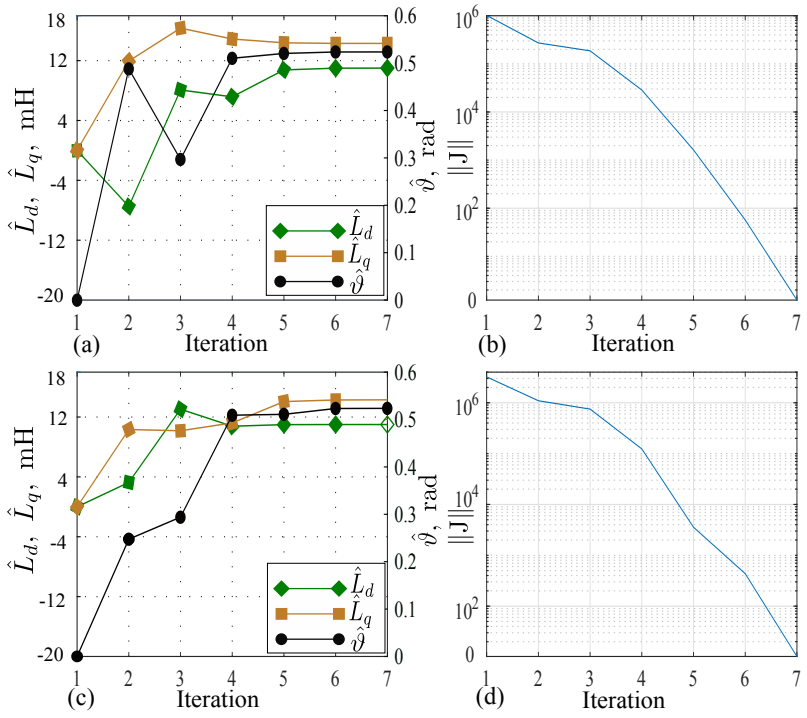

Figure 7.6: Nonlinear optimization trajectories of $\mathbf{x} = [\hat{\vartheta},\ \hat{L}_d,\ \hat{L}_q]'$ and error $\|\mathbf{J}\|$ for (a)-(b) the rated speed, $\mathbf{i}_{\delta\gamma} = [-10\text{A}, 10\text{A}]'$ and $\dot{\mathbf{i}}_{\delta\gamma} = [10^4\text{A/s}, 10^4\text{A/s}]'$, and for (c)-(d) zero speed, $\mathbf{i}_{\delta\gamma} = [-10\text{A}, 10\text{A}]'$ and $\dot{\mathbf{i}}_{\delta\gamma} = [10^4\text{A/s}, 10^4\text{A/s}]'$ (The actual value $\mathbf{x}_o = [\pi/6\text{ rad},\ 11\text{ mH},\ 14.3\text{ mH}]'$).

7.5 Experimental Validation

The proposed robust position estimation technique was experimentally validated for the reference IPMSM (see Table I for the details). The experiments were conducted in the motor dyno (see Appendix B for details). The dyno consists of an induction motor (IM) with the Yaskawa drive. FCSMPC and estimation algorithms for the reference IPMSM are implemented in MicroAutobox II. The controllers are configured to run the IM in speed control and the IPMSM in current control. The sampling frequency is kept at 10 kHz.

7.5.1 Speed Transient Performance

The speed reversal and speed sweep tests are carried out to validate the speed transient performance of the robust sensorless FCSMPC with parameter estimation ($\mathbf{x} = [\hat{\vartheta}, \hat{L}_d, \hat{L}_q]'$). The similar tests are also conducted for sensorless FCSMPC without parameter estimation ($\mathbf{x} = \hat{\vartheta}$) to compare the performance. The settings and control parameters are kept same for both sensorless scheme implementations.

Fig. 7.7 (a)-(e) and Fig. 7.8 (a)-(d) show the experimental results of the speed reversal tests at 100 rpm and at half the rated torque for the cases of $\mathbf{x} = [\hat{\vartheta}, \hat{L}_d, \hat{L}_q]'$ and $\mathbf{x} = \hat{\vartheta}$ respectively. The steady state position error for the former case is improved substantially and it is close to zero whereas for the latter case it is close to 0.125 rad. For the former case, as the inductances ($\hat{L}_d$ and $\hat{L}_q$) are estimated together with $\hat{\vartheta}$, the position estimation becomes independent of the variations in L_d and L_q. The nominal inductances are used for the latter case and therefore causes significant error in the position estimation. Similarly, for the speed reversal test at 100 rpm and at the full rated torque, the position estimation for the case of $\mathbf{x} = [\hat{\vartheta}, \hat{L}_d, \hat{L}_q]'$ is much

lower (0.04 rad) than the case of $\mathbf{x} = \hat{\vartheta}$ (0.225 rad) as shown in Fig. 7.7 (f)-(j) and Fig. 7.8 (e)-(h) respectively. The transient position error at the speed reversal is also improved for the case of $\mathbf{x} = [\hat{\vartheta}, \hat{L}_d, \hat{L}_q]'$ (Fig. 7.7 (a)-(j)) as the correct information of the inductances is available in optimization. Moreover, the estimated values of the inductances are close to the offline measurement given in Appendix B.

The results of the experimental speed sweep tests from standstill to half the rated speed (350 rpm) and back within 150 ms at 25% rated torque for the case of $\mathbf{x} = [\hat{\vartheta}, \hat{L}_d, \hat{L}_q]'$ and $\mathbf{x} = \hat{\vartheta}$ are shown in Fig. 7.9 (a)-(f) and Fig. 7.10 (a)-(d) respectively. The speed sweep test at higher loads is unable to conduct in the experimental setup as the dyno motor current reaches its limit. The estimated inductances are close to the nominal values as there is no core saturation at this torque. There is no significant difference in position error between the case of $\mathbf{x} = [\hat{\vartheta}, \hat{L}_d, \hat{L}_q]'$ and $\mathbf{x} = \hat{\vartheta}$ as the values of the inductances are not varied at this test. The maximum transient state position error is within $+0.3$ rad and -0.35 rad for both the cases.

The proposed robust sensorless scheme is able to estimate the position at standstill (as shown in Fig. 7.9) provided there is enough persistent excitation from the switching ripples. The persistent excitation stops for FCSMPC at no load standstill as it applies null vector however a small negative δ axis current would overcome this limitation as mentioned in section 4.5. Moreover, the proposed scheme does not compensate for magnetic polarity and saddle solutions at standstill. However, the nonlinear optimization based compensation techniques presented in section 6.5 can be integrated to the proposed technique at the start-up.

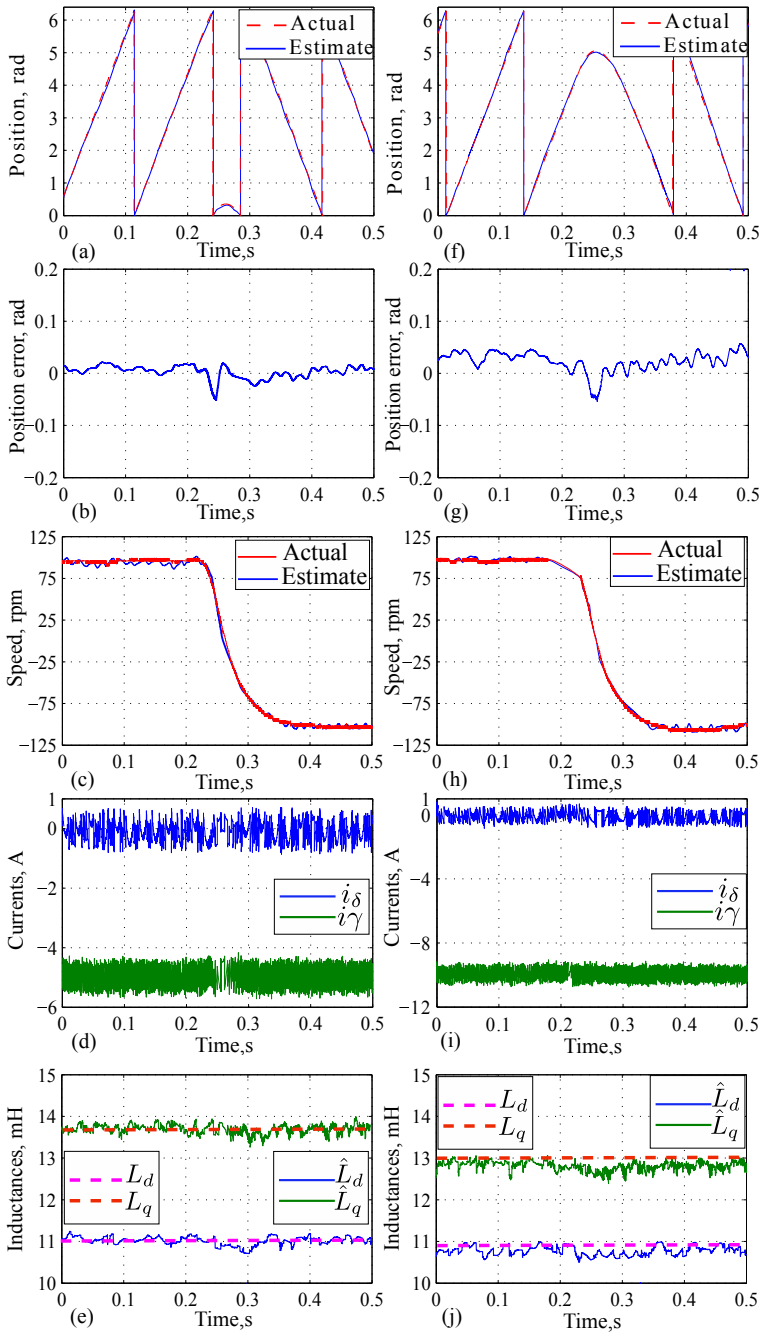

Figure 7.7: Robust sensorless FCSMPC ($\mathbf{x} = [\hat{\vartheta}, \hat{L}_d, \hat{L}_q]'$) scheme- the experimental speed reversal test results at 100rpm (a)-(d) at half the rated torque and (e)-(f) at the rated torque.

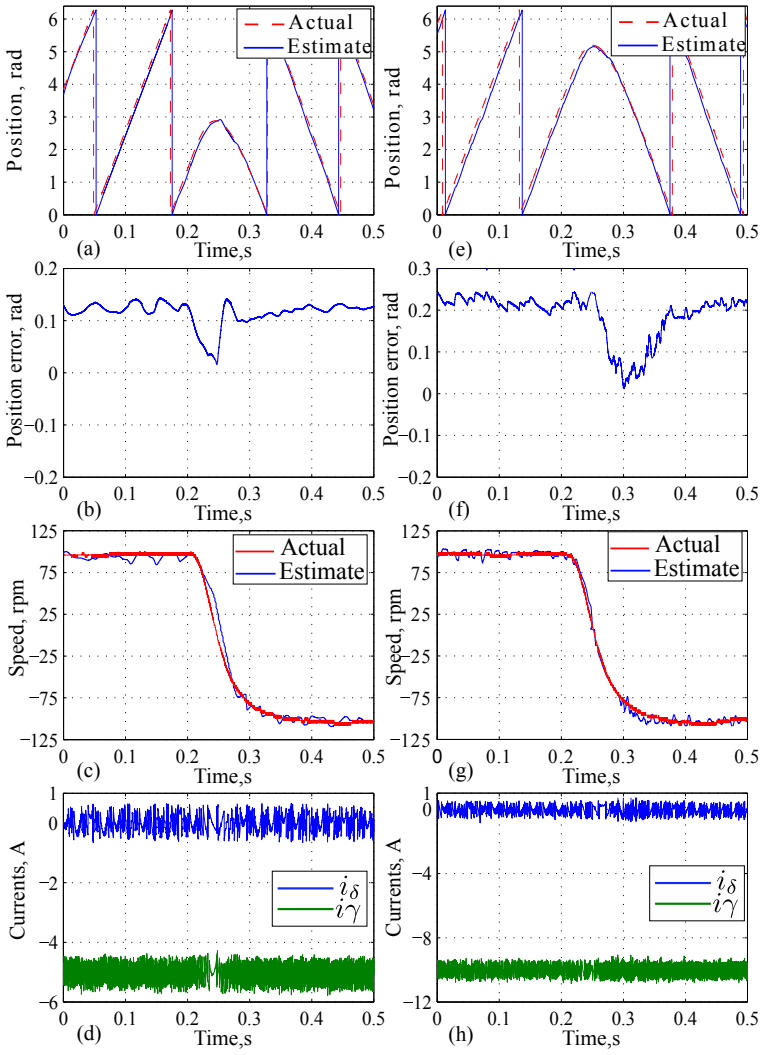

Figure 7.8: Non-robust sensorless FCSMPC ($\mathbf{x} = \hat{\vartheta}$) scheme- the experimental speed reversal test results at 100rpm (a)-(d) at half the rated torque and (e)-(f) at the rated torque.

7.5.2 Torque Transient Performance

The torque transient performance of the proposed robust sensorless FCSMPC ($\mathbf{x} = [\hat{\vartheta}, \hat{L}_d, \hat{L}_q]'$) is experimentally verified by conducting the torque reversal and the torque step tests. The similar tests are also conducted for the sensorless FCMPC without

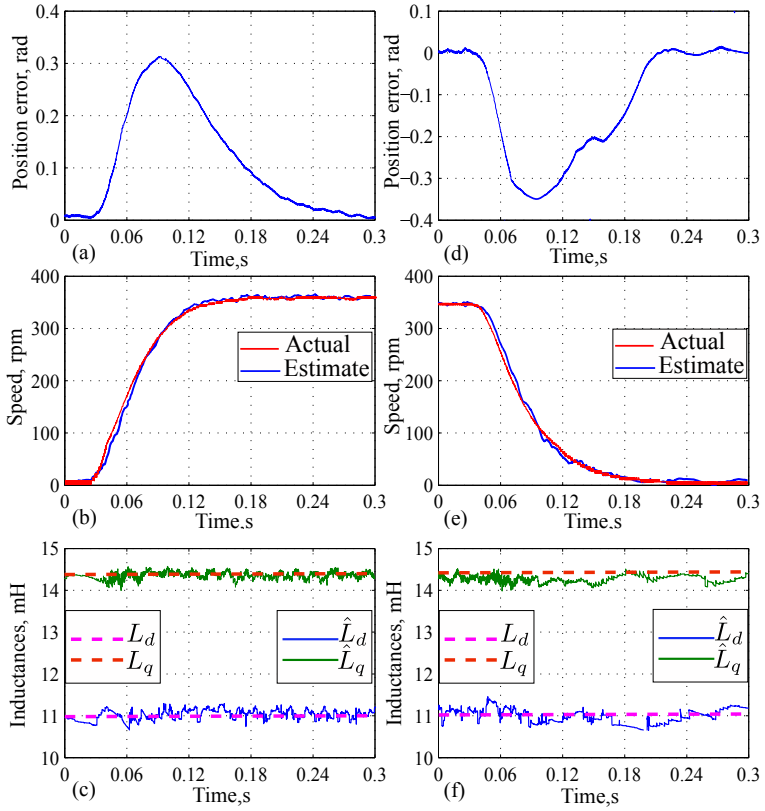

Figure 7.9: Robust sensorless FCSMPC ($\mathbf{x} = [\hat{\vartheta}, \hat{L}_d, \hat{L}_q]'$) scheme- the experimental speed sweep test results from 0 rpm to half the rated speed (350rpm) and back at 25% rated torque.

inductance estimation ($\mathbf{x} = \hat{\vartheta}$) for the sake of comparison. The results of the torque reversal tests at the rated load and at 100 rpm is shown in Fig. 7.11 (a)-(e) and Fig. 7.12 (a)-(d) for the case of $\mathbf{x} = [\hat{\vartheta}, \hat{L}_d, \hat{L}_q]'$ and $\mathbf{x} = \hat{\vartheta}$ respectively. The steady state position error is substantially improved for the case of $\mathbf{x} = [\hat{\vartheta}, \hat{L}_d, \hat{L}_q]'$ (within ± 0.04 rad) as compared to $\mathbf{x} = \hat{\vartheta}$ (0.225 rad). Similar to the steady state case of the speed transient performance, this improvement is attributed to the estimation of the inductances. The transient position error is also improved significantly for the case of $\mathbf{x} = [\hat{\vartheta}, \hat{L}_d, \hat{L}_q]'$ (by 0.28 rad) as there is always the correct estimation

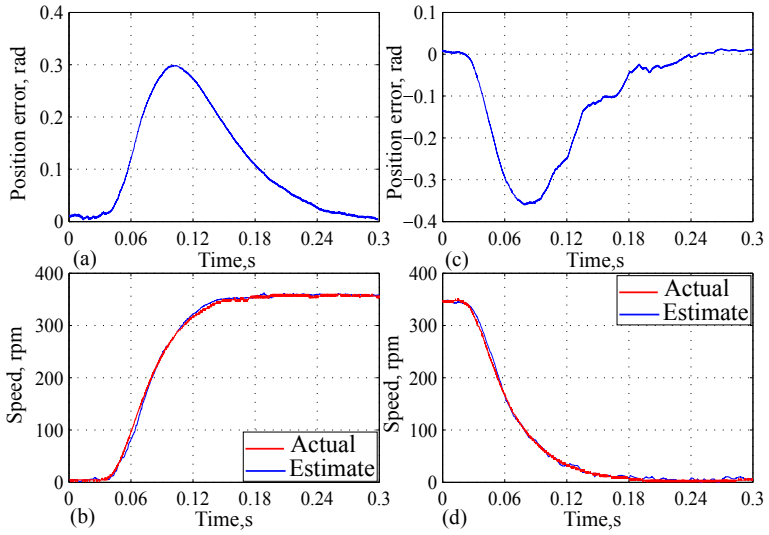

Figure 7.10: Non-robust sensorless FCSMPC ($\mathbf{x} = \hat{\vartheta}$) scheme- the experimental speed sweep test results from 0 rpm to half the rated speed (350rpm) and back at 25% rated torque.

of the inductances. The value of $\hat{L}_q$ changes from saturated value (12.8 mH) to the nominal value (14.3 mH) as i_γ moves from -10A to 0 A as shown in Fig. 7.11 (c). The reduction in $\hat{L}_d$ (10.8 mH) as shown in Fig. 7.11 (c) from the nominal value (11 mH) is due to the cross saturation.

The experimental results of torque step tests from no load to the rated torque for the proposed robust sensorless FCSMPC ($\mathbf{x} = [\hat{\vartheta}, \hat{L}_d, \hat{L}_q]'$) and for the sensorless FCMPC without inductance estimation ($\mathbf{x} = \hat{\vartheta}$) are shown in Fig. 7.11 (f)-(j) and Fig. 7.12 (e)-(h) respectively. The estimated value of $\hat{L}_q$ changes from the nominal value (14.3 mH) to the saturated value (12.8 mH) as i_γ steps from 0 A to -10 A. Similar to the torque reversal test, the transient position error is improved substantially for the case of $\mathbf{x} = [\hat{\vartheta}, \hat{L}_d, \hat{L}_q]'$ (by 0.25 rad) as there is always correct estimation of the inductances as compared to $\mathbf{x} = \hat{\vartheta}$. The steady state position error is also improved for $\mathbf{x} = [\hat{\vartheta}, \hat{L}_d, \hat{L}_q]'$ by 0.175 rad. The additional experimental test results at different

i_δ and i_γ to validate the estimation of $\hat{L}_d$ and $\hat{L}_q$ are are performed, but not included in this thesis as it focuses on the performance of the sensorless FCSMPC with estimation of the inductances.

The switching current ripples is slightly increasesd at the time of the torque transients for the case of FCSMPC with nominal inductances (see Fig. 7.12 (e) and (h)) whereas by providing the estimated inductances this behavior is not observed (see Fig. 7.11 (e) and (j)). This is due to the fact that the prediction of the voltage vectors is accurate with the estimated inductances and hence no increase in the switching ripples. There are no other improvements in FCSMPC with estimated inductances as found from the tests conducted for the reference IPMSM machine.

The summary of the experimental results is provided in Table II. The transient position error is defined as the difference between the steady state and the maximum transient errors. The response time is defined as the time from a torque or speed steps happened to the steady state of the position error.

Table 7.1: Summary of Experimental Results

Operating conditions	Steady state position error (rad)		Maximum transient state position error (rad)		Response time (s)	
Schemes	Robust	Non-robust	Robust	Non-robust	Robust	Non-robust
Speed reversal[1]	0	0.125	0.05	0.1	0.03	0.08
Speed reversal[2]	0.04	0.225	0.05	0.215	0.03	0.1
Speed sweep[3]	0	0.01	0.31	0.3	0.26	0.26
Torque reversal[4]	0.04	0.225	0.05	0.075	0.15	0.225
Torque step[5]	0.04	0.225	0.04	0.225	0.06	0.14

1: 100 rpm and 50% rated load, 2: 100 rpm and 100% rated load, 3: 0 rpm to 350 rpm at 25% rated load,

4: 100 rpm with rated load, and 5: 0 Nm to 100% rated load at 100rpm.

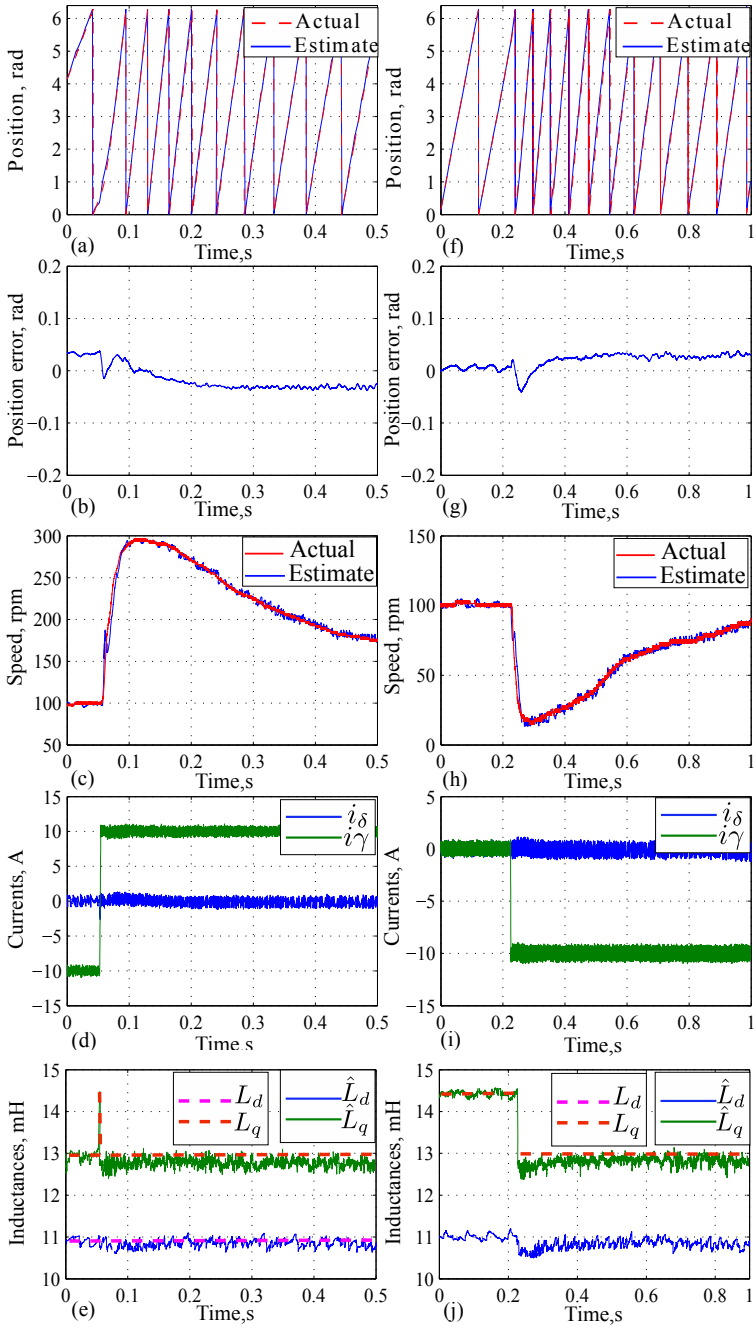

Figure 7.11: Robust sensorless FCSMPC ($\mathbf{x} = [\hat{\vartheta}, \hat{L}_d, \hat{L}_q]'$) scheme- the experimental torque transient tests at 100 rpm (a)-(e) torque reversal at the rated load, and (f)-(j) torque step from no load to the rated load.

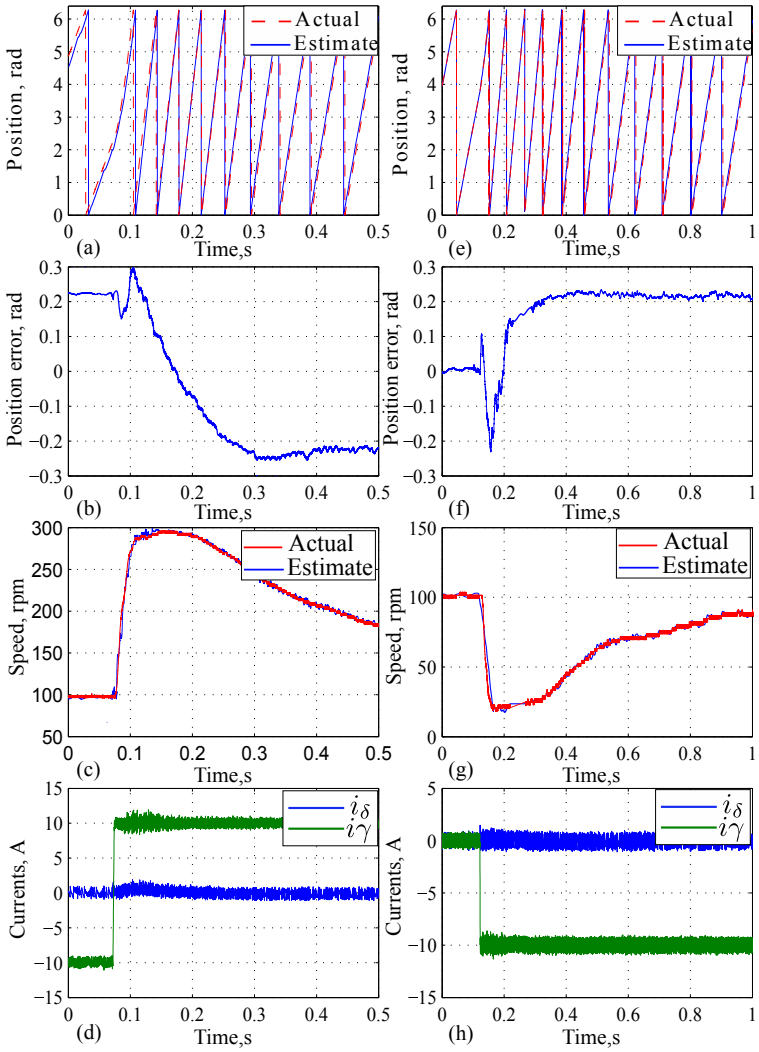

Figure 7.12: Non-robust sensorless FCSMPC ($\mathbf{x} = \hat{\vartheta}$) scheme- the experimental torque transient tests at 100 rpm (a)-(e) torque reversal at the rated load, and (f)-(j) torque step from no load to the rated load.

7.6 Summary

This chapter presents simulataneous estimation of position and parameters based on nonlinear optimization to realize robust sensorless FCSMPC for IPMSM. The

proposed sensorless FCSMPC scheme is capable of estimating the position and parameters from standstill to the rated speed without any changeover or additional signal injection. The detailed robustness analysis carried out in this chapter shows that d and q axis inductances are the major influencing parameters on the accuracy of the position estimation. The experimental results of different speed and torque transients tests verify that the co-estimation of d and q inductances with position improves both steady and transient states performances. For an instance, the position error is reduced to 0.04 rad from 0.225 rad at both steady and transient states, and response time is improved by 57%, for a torque step from no load to the rated load with co-estimation of parameters.

Chapter 8

Conclusions and Future Work

This thesis presents the significance of persistent voltage vector excitations towards the simultaneous estimation of machine parameters, position and speed for IPSMS drives, and also shows that nonlinear optimization based technique is an ideal candidate for robust sensorless FCSMPC.

Not all the combinations of the machine parameters, position and speed are observable at steady state without persistent excitation in the system. This thesis identifies all the non-observable combinations and determines the persistent excitation requirements to meet the observability. The online estimations of the parameters are realized with the help of recursive least square adaptation algorithm and experimentally shows that the voltage vector injections by FCSMPC establish persistent excitation and overcome the observability issues at steady state. Moreover, the wrong convergence in the estimation of the coupled parameters is analyzed and a decoupling technique is proposed .

The standard position estimation techniques cannot be applied for FCSMPC as it applies finite voltage vectors without a modulator and generates arbitrary switching

ripples with widely varying frequency. This thesis proposes a nonlinear optimization based scheme for sensorless FCSMPC valid at entire operating range including no-load standstill without any additional signal injection and switchover. This thesis also proposes a compensator to avoid wrong convergences to the saddle and symmetrical (π ambiguity) solutions. The experimental results from the speed and torque transient tests are promising and those are in par with the results from the tests conducted for the vector control with the same sensorless scheme. There is an improvement in steady state position error (by 0.045 rad) at standstill as compared to the vector control attributed to the strong switching ripples associated with FCSMPC. However, the performance of the sensorless FCSMPC deteriorates at medium speed with load (0.06 rad rise in position error) as the high switching ripples intensify the effect of inductance variation by saturation. Moreover, the proposed sensorless scheme performs superior as compared to other model based techniques in literature for FCSMP. The proposed scheme has very low steady state position oscillations about ± 0.025 rad and the position error is 0.03 rad at no load and 0.225 rad at the full rated load.

A state of the art single observer based on nonlinear optimization for estimating both position and parameters is proposed in this thesis to realize the robust sensorless FCSMPC. The detailed robustness analysis shows that d and q axis inductances are the major influencing parameters on the accuracy of the position estimation. The experimental results of different speed and torque transients tests verify that the co-estimation of d and q inductances with position improves both steady and transient states performances. For an instance, the position error is reduced to 0.04 rad from 0.225 rad at both steady and transient states, and response time is improved by 57%, for a torque step from no load to the rated load with the co-estimation of parameters.

8.1 Future Work

This thesis investigates and experimentally validates the importance of voltage vector injections by FCSMPC to establish PE to simultaneously observe both the position and parameters. The voltage vectors by FCSMPC should produce nonzero first and second order derivatives of the currents in order be a PE input. The strong switching ripples produced by voltage vector injections are able to meet these requirements. However, the switching ripple is not a desirable performance for a motor drive, and there are ongoing research on FCSMPC focused on its reduction. The work conducted in this thesis should be extended to investigate the simultaneous observability at different levels of switching ripples. Moreover, it should be also interesting to investigate the performance of other signal injections e.g. sinusoidal and square wave related to conventional control schemes like vector control.

The experimental validations are conducted in this thesis to show that all the machine parameter combinations which are not observable at steady state without PE become observable with voltage vector injections by FCSMPC. However, all the non-observable combinations with position and parameters are not validated in this thesis as it is challenging to implement higher order observers in real time. Therefore, the investigations for different observers which are light in computation and for high performance dedicated real time hardware platforms would be the next logical step in this research. Moreover, the proposed observers in this thesis are implemented in dSPACE MicroAutobox II DS1401/1513 which comes with microprocessor IBM PPC 750GL and runs at 900 MHz clock cycle. However, in practical perspective, the observers should be implemented and tested in microcontrollers which are generally run below 200 MHz clock cycles.

In the robust sensorless position estimation scheme proposed in this thesis, the apparent self inductances which implicitly account for the saturation and cross-saturation effects are estimated simultaneously with the position. Although, the experimental results for the reference IPMSM show that position estimation is accurate with this treatment, it has been reported in the literature that the explicit treatment of the incremental self and mutual inductances can further improve the estimation accuracy. Therefore, it is beneficial to investigate the effects of mutual inductance on the position estimation with the proposed estimation technique for other IPMSMs. The permanent magnet flux linkage and the winding resistance are not the major influencing parameters on the position estimation for reference IPMSM however it should be verified for other IPMSMs.

The inverter to drive the reference IPSMS used in this thesis employs silicon carbide power MOSFETs from CREE C2M0025120D (800V, 30A) which has turn-on resistance about eight times (25 mΩ) lesser than the similar rated silicon based MOSFETs. Therefore, the turn-on resistance does not play a significant role in the estimation of the parameters and position and hence not considered in this thesis. It should be also noted the phase resistance of the reference IPMSM is 0.4 Ω which is much higher than the device turn-on resistance. However, the impact of turn-on resistance should be investigated if the standard switching devices are used. The effects of other inverter nonlinearities like dead time, parasitic capacitance and unsymmetrical turn-on/off delays should be also explored.

The experimental results prove that the proposed robust position estimation technique is a promising scheme for sensorless IPMSM drives with FCSMPC. Therefore, it is worthwhile to apply it for other control techniques and machine topologies.

8.2 Publications

8.2.1 Journals

S. Nalakath, M. Preindl, N. M. Babak and A. Emadi, "Robust Sensorless Model Predictive Control for IPMSM Drives with Estimation of Parameters," submitted to *IEEE Transactions on Industrial Electronics*.

S. Nalakath, Y. Sun, M. Preindl and A. Emadi, "Optimization-based Position Sensorless Finite Control Set Model Predictive Control for IPMSMs," in *IEEE Transactions on Power Electronics*, vol. PP, no. 99, pp. 1-1, to be published.

S. Nalakath, M. Preindl and A. Emadi, "Online multi-parameter estimation of interior permanent magnet motor drives with finite control set model predictive control, " in *IET Electric Power Applications*, vol. 11, no. 5, pp. 944-951, 2017.

Y. Yang, B. Bilgin, M. Kasprzak, **S. Nalakath**, H. Sadek, M. Preindl, J. Cotton, N. Schofield and A. Emadi, "Thermal management of electric machines," *IET Electrical Systems in Transportation*, vol. 7, pp. 104-106, 2017.

S. Nalakath, L. N. Srivatchan, D. Luedtke, B. Bilgin, M. Preindl, "The Magnetic Circuit based Core Loss Model of IPMSM for Online Estimation," *IEEE Transactions on Vehicular Technology* (To be submitted).

8.2.2 Conferences

S Nalakath, M Preindl, B Bilgin, A Emadi, C Bing, L Y Joo, "Modeling and Analysis of AC Resistance of a Permanent Magnet Machine for Online Estimation Purposes," *IEEE Energy Conversion Congress and Exposition (ECCE)*, Montreal, QC, 2015, pp.

314-319.

S. Nalakath, M. Preindl, Y. Yang, B. Bilgin, B. Cheng and A. Emadi, "Modeling and analysis of core losses of an IPM machine for online estimation purposes," *Annual Conference of the IEEE Industrial Electronics Society (IECON)*, Yokohama, 2015, pp. 004104-004109.

S. Nalakath, M. Preindl, N. M. Babak and A. Emadi, "Low speed position estimation scheme for model predictive control with finite control set," *Annual Conference of the IEEE Industrial Electronics Society, IECON*, Florence, 2016, pp. 2839-2844.

A. Callegaro, **S. Nalakath**, L. N. Srivatchan, D. Luedtke, B. Bilgin, M. Preindl, "Optimization-Based Position Sensorless for Induction Machines," *IEEE Transportation Electrification Conference and Expo (ITEC)*, Long Beach, 2018 (Accepted for presentation).

L. Sun, **S. Nalakath**, H. B. Polli, D. Luedtke, M. Preindl, "IPMSM Sensorless Control with Accounting for Inverter and Motor Nonlinearities in 48V Hybrid System," *IEEE Transportation Electrification Conference and Expo (ITEC)*, Long Beach,2018 (Accepted for presentation).

Appendix A

Clarke and Park Transformation

The transformation from one reference frame to other is performed to simplify the modeling, analysis, and control of electric machinery and systems. The popular transformations are the Clarke or $\alpha\beta$ and the Park or dq.

A.1 Full Tranformation

In Clark, the variables corresponding to three stationary axes (abc) sperated by $2\pi/3$ rad are transformed into two stationary quadrature axes ($\alpha\beta$) with the help of geometrical relationships between those axes. A general three phase variable vector $\mathbf{x}_{abc} \in \mathbb{R}^3$ is transformed from abc to $\alpha\beta$ to obtain $\mathbf{x}_{\alpha\beta} \in \mathbb{R}^3$ is

$$\mathbf{x}_{\alpha\beta} = \mathbf{T}_{\alpha\beta}\mathbf{x}_{abc} \tag{A.1}$$

where $\mathbf{T}_{\alpha\beta}$ is the transformation matrix

$$\mathbf{T}_{\alpha\beta} = \frac{2}{3}\begin{bmatrix} 1 & -\frac{1}{2} & -\frac{1}{2} \\ 0 & \frac{\sqrt{3}}{2} & -\frac{\sqrt{3}}{2} \\ \frac{1}{2} & \frac{1}{2} & \frac{1}{2} \end{bmatrix} \tag{A.2}$$

The variable vector $\mathbf{x}_{\alpha\beta}$ is transformed into the reference frame dq to yield $\mathbf{x}_{dq} \in \mathbb{R}^3$ which rotates with a speed ω and displaced from $\alpha\beta$ with corresponding rotational angle θ as

$$\mathbf{x}_{dq} = \mathbf{T}_{dq}\mathbf{x}_{\alpha\beta} \tag{A.3}$$

where $\mathbf{T}_{dq}$ is the corresponding transformation matrix

$$\mathbf{T}_{dq} = \begin{bmatrix} \cos\theta & \sin\theta & 0 \\ -\sin\theta & \cos\theta & 0 \\ 0 & 0 & 1 \end{bmatrix} \tag{A.4}$$

Both $\mathbf{T}_{\alpha\beta}$ and $\mathbf{T}_{dq}$ are invertible and corresponding to power-variant approach.

A.2 Partial Transformation

The zero sequences components do not exist for a balanced three phase systems and for the system with isolated neutral point. Therefore, the partial transformations of (A.1) and A.3) are often preferred for modeling and control. The corresponding

transformation matrices are

$$\mathbf{T}_{\alpha\beta} = \frac{2}{3}\begin{bmatrix} 1 & -\frac{1}{2} & -\frac{1}{2} \\ 0 & \frac{\sqrt{3}}{2} & -\frac{\sqrt{3}}{2} \end{bmatrix} \tag{A.5}$$

and

$$\mathbf{T}_{dq} = \begin{bmatrix} \cos\theta & \sin\theta & 0 \\ -\sin\theta & \cos\theta & 0 \end{bmatrix} \tag{A.6}$$

A.3 Transforming Derivatives

The transformation matrix $\mathbf{T}_{\alpha\beta}$ is a constant and hence transformation of $\dot{\mathbf{x}}_{abc}$ into $\alpha\beta$ is found as

$$\dot{\mathbf{x}}_{\alpha\beta} = \mathbf{T}_{\alpha\beta}\dot{\mathbf{x}}_{abc} \tag{A.7}$$

As θ is continuously varying with respect time, the transformation of $\dot{\mathbf{x}}_{\alpha\beta}$ into dq is found as

$$\dot{\mathbf{x}}_{dq} = \mathbf{T}_{dq}\dot{\mathbf{x}}_{\alpha\beta} + \mathbf{T}_r\mathbf{T}_{dq}\mathbf{x}_{\alpha\beta} \tag{A.8}$$

where $\dot{\mathbf{T}}_{dq} = \mathbf{T}_r\mathbf{T}_{dq}$, and $\mathbf{T}_r$ is a rotational matrix

$$\mathbf{T}_r = \begin{bmatrix} 0 & -1 & 0 \\ 1 & 0 & 0 \\ 0 & 0 & 0 \end{bmatrix}, \quad \text{and} \quad \mathbf{T}_r = \begin{bmatrix} 0 & -1 \\ 1 & 0 \end{bmatrix} \tag{A.9}$$

for partial tranformation.

Appendix B

Experimental Setup

The photograph of the experimental setup is depicted in Fig. B.1. It consists of a 5 kW induction motor with the Yaskawa A-1000 drive as the dyno, and the reference IPMSM driven by silicon carbide inverter with dSPACE MicroAutobox II DS1401/1513. The motor control and estimation algorithms for the reference IPMSM are implemented in MicroAutobox II . The silicon carbide power MOSFETs are from CREE C2M0025120D (800V, 30A). The details of the reference machine is provided in Table B.1. The controllers are configured to run the IM in speed control and the IPMSM in current control and the sampling and switching frequencies are kept at 10kHz for all the experiments. The inductance profile of the reference IPMSM machine measured offline is provided in Fig. B.2. The inductance is measured by conducting tests at steady state with a speed close to the rated speed and by varying i_d and i_q.

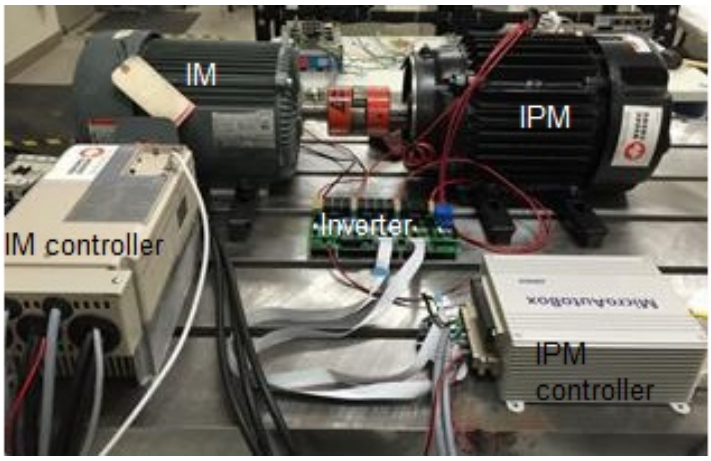

Figure B.1: Motor dyno setup.

Table B.1: The Details of the Reference IPMSM

Details	Values
Number of poles	10
Rated current	9.4 A
Rated torque	29.7 Nm
Rated speed	700 rpm
Nominal d inductance	11 mH
Nominal q inductance	14.3 mH
Nominal PM flux linkage	333.3 mWb
Nominal stator resistance	400 mΩ
DC link voltage	300 V

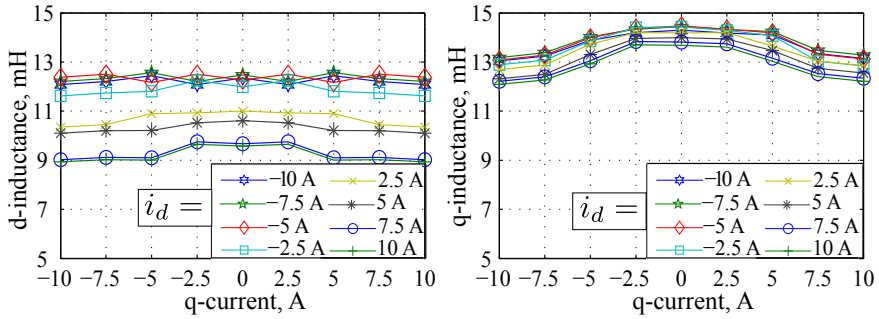

Figure B.2: The measured apparent inductances (a) for d axis, and (b) for q axis.

References

A. Domahidi, A. Zgraggen, M. Z. M. M. and Jones, C. (2012). Efficient interior point methods for multistage problems arising in receding horizon control. *IEEE Conference on Decision and Control (CDC)*, pages 668–674.

Basic, D., Malrait, F., and Rouchon, P. (2010). Euler-lagrange models with complex currents of three-phase electrical machines and observability issues. *IEEE Transactions on Automatic Control*, **55**(1), 212–217.

Bemporad, A., Morari, M., Dua, V., and Pistikopoulos, E. (2000). The explicit solution of model predictive control via multiparametric quadratic programming. *American Control Conference*, **2**(2), 872–876.

Bemporad, A., Morari, M., Dua, V., and Pistikopoulos, E. N. (2002). The explicit linear quadratic regulator for constrained systems. *Automatica*, **38**(1), 3–20.

Besselmann, T. J., Van De Moortel, S., Almer, S., Jorg, P., and Ferreau, H. J. (2016). Model Predictive Control in the Multi-Megawatt Range. *IEEE Transactions on Industrial Electronics*, **63**(7), 4641–4648.

Bhotto, M. Z. A. and Antoniou, A. (2013). New Improved Recursive Least-Squares

Adaptive-Filtering Algorithms. *IEEE Transactions on Circuits and Systems I: Regular Papers*, **60**(6), 1548–1558.

Bianchi, N., Bolognani, S., Pre, M. D., and Grezzani, G. (2006). Design considerations for fractional-slot winding configurations of synchronous machines. *IEEE Transactions on Industry Applications*, **42**(4), 997–1006.

Boileau, T., Leboeuf, N., Nahid-Mobarakeh, B., and Meibody-Tabar, F. (2011). Online Identification of PMSM Parameters: Parameter Identifiability and Estimator Comparative Study. *IEEE Transactions on Industry Applications*, **47**(4), 1944–1957.

Bolognani, S., Bolognani, S., Peretti, L., and Zigliotto, M. (2008). Combined speed and current model predictive control with inherent field-weakening features for PMSM drives. *Proceedings of the Mediterranean Electrotechnical Conference - MELECON*, (1), 472–478.

Bolognani, S., Bolognani, S., Peretti, L., and Zigliotto, M. (2009). Design and Implementation of Model Predictive Control for Electrical Motor Drives. *IEEE Transactions on Industrial Electronics*, **56**(6), 1925–1936.

Bose, B. K. (2002). *Modern Power Electronics and AC Drives*. Prentice Hall PTR, Upper Saddle River, NJ.

Bose, B. K. (2009). Power electronics and motor drives recent progress and perspective. *IEEE Transactions on Industrial Electronics*, **56**(2), 581–588.

Camacho, Eduardo F., B. A. and Carlos (2007). *Model Predictive Control*. Springer, London.

Chang, S. C. and Yeh, S. N. (1996). Current sensorless field-oriented control of induction motors. *IEE Proceedings - Electric Power Applications*, **143**(6), 492–500.

Cimini, G., Bernardini, D., Bemporad, A., and Levijoki, S. (2015). Online model predictive torque control for Permanent Magnet Synchronous Motors. *2015 IEEE International Conference on Industrial Technology (ICIT)*, pages 2308–2313.

Cooper, L. and Steinberg, D. (1970). *Introduction to methods of optimization*. W. B. Saunders, Philadelphia, PA.

Corley, M. J. and Lorenz, R. D. (1998). Rotor position and velocity estimation for a salient-pole permanent magnet synchronous machine at standstill and high speeds. *IEEE Transactions on Industrial Electronics*, **34**(4), 784–789.

Dang, D. Q., R. M. S. C. H. H. J. J. W. (2016). Online parameter estimation technique for adaptive control applications of interior pm synchronous motor drives. *IEEE Transactions on Industry Applications*, **63**(3), 1438–1449.

De Doncker, Rik, P. D. W. V. A. (2002). *Advanced Electrical Drives-Analysis, Modeling, Control*. Springer, Netherlands.

DOE/GO-102014-4356 (2014). Improving motor and drive system performance. Technical report.

Dutta, R., Chong, L., and Rahman, M. F. (2013). Design and experimental verification of an 18-slot/14-pole fractional-slot concentrated winding interior permanent magnet machine. *IEEE Transactions on Energy Conversion*, **28**(1), 181–190.

EL-Refaie, A. M. (2010). Fractional-slot concentrated-windings synchronous permanent magnet machines: Opportunities and challenges. *IEEE Transactions on Industrial Electronics*, **57**(1), 107–121.

El-Refaie, A. M., Jahns, T. M., and Novotny, D. W. (2006). Analysis of surface permanent magnet machines with fractional-slot concentrated windings. *IEEE Transactions on Energy Conversion*, **21**(1), 34–43.

Emadi, A. (2015). *Advanced Electric Drive Vehicles*. CRC Press, Boca Raton.

Epelman, M. (2007). Continuous optimization methods.

Erikson, E. (2010). Principal minors and the hessian.

Foo, G. and Xinan, Z. (2015). Sensorless stator flux observer for direct torque controlled interior permanent magnet synchronous motor drives using the current derivative approach. *IECON 41st Annu. Conf.IEEE Industrial Electronics Society*, pages 001843–001848.

Frison, G., Sokoler, L. E., and J??rgensen, J. B. (2014a). A family of high-performance solvers for linear model predictive control. *IFAC Proceedings Volumes (IFAC-PapersOnline)*, **19**, 3074–3079.

Frison, G., Sokoler, L. E., and J??rgensen, J. B. (2014b). A family of high-performance solvers for linear model predictive control. *IFAC Proceedings Volumes (IFAC-PapersOnline)*, **19**, 3074–3079.

Frison, G., Srensen, H. H. B., Dammann, B., and Jrgensen, J. B. (2014c). High-performance small-scale solvers for linear model predictive control. *2014 European Control Conference (ECC)*, pages 128–133.

Fuentes, E. and Kennel, R. (2011). Sensorless-predictive torque control of the pmsm using a reduced order extended kalman filter. In *2011 Symposium on Sensorless Control for Electrical Drives*, pages 123–128.

Gabriel, R., Leonhard, W., and Nordby, C. J. (1980). Field-oriented control of a standard ac motor using microprocessors. *IEEE Transactions on Industry Applications*, **IA-16**(2), 186–192.

Ge, H., Miao, Y., Bilgin, B., Nahid-Mobarakeh, B., and Emadi, A. (2017). Speed range extended maximum torque per ampere control for pm drives considering inverter and motor nonlinearities. *IEEE Transactions on Power Electronics*, **32**(9), 7151–7159.

Geyer, T. (2009). Generalized model predictive direct torque control: Long prediction horizons and minimization of switching losses. *Proceedings of the IEEE Conference on Decision and Control*, pages 6799–6804.

Geyer, T. (2011). Model predictive direct torque control: Derivation and analysis of the explicit control law. *Energy Convers. Congr. Expo. (ECCE), 2011 IEEE*, pages 355–362.

Geyer, T., Papafotiou, G., and Morari, M. (2009). Model Predictive Direct Torque Control Part I : Concept , Algorithm , and Analysis. **56**(6), 1894–1905.

Geyer, T., Beccuti, G. a., Papafotiou, G., and Morari, M. (2010). Model Predictive Direct Torque Control of permanent magnet synchronous motors. *Energy Convers. Congr. Expo. (ECCE), 2010 IEEE*, pages 199–206.

Gong, L. (2012). *Carrier signal injection based sensorless control of permanent magnet brushless AC machines*. Ph.D. thesis, The University of Sheffield.

Gong, L. M. and Zhu, Z. Q. (2012). Robust initial rotor position estimation of permanent-magnet brushless ac machines with carrier-signal-injection-based sensorless control. *IEEE Transactions on Industry Applications*, **49**(6), 2602–2609.

Goss, J., Staton, D., Wrobel, R., and Mellor, P. (2013). Brushless ac interior-permanent magnet motor design: Comparison of slot/pole combinations and distributed vs. concentrated windings. pages 1213–1219.

Guerra, A. D. L., Maya-Ortiz, P., and Espinosa-Prez, G. (2015). Global observability analysis of the sr motor under sensorless operation. In *2015 54th IEEE Conference on Decision and Control (CDC)*, pages 1799–1804.

Hadley, G. (1964). *Nonlinear and Dynamic Programming*. Addison-Wesley, Reading, MA.

Hamidizadeh, S. (2016). *Study of Magnetic Properties and Demagnetization Models of Permanent Magnets for Electric Vehicles Application*. Ph.D. thesis, McGill University.

Hayes, M. H. (1996). *Statistical Digital Signal Processing and Modeling*. Wiley, New York.

Hermann, R. and Krener, A. (1977). Nonlinear controllability and observability. *IEEE Transactions on Automatic Control*, **22**(5), 728–740.

Ichikawa, S., Tomita, M., Doki, S., and Okuma, S. (2006). Sensorless control of permanent-magnet synchronous motors using online parameter identification based

on system identification theory. *IEEE Transactions on Industrial Electronics*, **53**(2), 363–372.

Inoue, T., Inoue, Y., Morimoto, S., and Sanada, M. (2016). Maximum torque per ampere control of a direct torque-controlled pmsm in a stator flux linkage synchronous frame. *IEEE Transactions on Industry Applications*, **52**(3), 2360–2367.

Jahns, T. M., Kliman, G. B., and Neumann, T. W. (1986). Interior Permanent-Magnet Synchronous Motors for Adjustable-Speed Drives. *IEEE Transactions on Industry Applications*, **IA-22**(4), 738–747.

Jung, L. L. (1971). Report on characterization of the concept of 'persistently exciting' in the frequency domain.

Kim, S., Yoon, Y. D., Sul, S. K., and Ide, K. (2013). Maximum torque per ampere (mtpa) control of an ipm machine based on signal injection considering inductance saturation. *IEEE Transactions on Power Electronics*, **28**(1), 488–497.

Kouvaritakis, B. and Cannon, M. (2016). *Model Predictive Control- Classical, Robust and Stochastic*. Springer, Switzerland.

Landsmann, P. and Kennel, R. (2012). Saliency-based sensorless predictive torque control with reduced torque ripple. *IEEE Transactions on Power Electronics*, **27**(10), 4311–4320.

Laroche, E., Sedda, E., and Durieu, C. (2008). Methodological insights for online estimation of induction motor parameters. *IEEE Transactions on Control Systems Technology*, **16**(5), 1021–1028.

Lee, J. H. (2011). Model predictive control: Review of the three decades of development. *International Journal of Control, Automation and Systems*, **9**(3), 415–424.

Leidhold, R. (2011). Position sensorless control of pm synchronous motors based on zero-sequence carrier injection. *IEEE Transactions on Industrial Electronics*, **58**(12), 5371–5379.

Li, M., C. J. B. M. T. L. (2005). Observability of speed in an induction motor from stator currents and voltages. *IEEE Conference on Decision and Control*, pages 3438–3443.

Linder, A. and Kennel, R. (2005a). Direct model predictive control - a new direct predictive control strategy for electrical drives. *2005 European Conference on Power Electronics and Applications*, pages 10 pp.–P.10.

Linder, A. and Kennel, R. (2005b). Model Predictive Control for Electrical Drives. *Power Electron. Spec. Conf. 2005. PESC '05. IEEE 36th*, pages 1793–1799.

Liu, Q., H. K. (2015). A fast online full parameter estimation of a pmsm with sinusoidal signal injection. *IEEE Energy Conversion Congress and Exposition (ECCE)*, pages 4091–4096.

Liu, J. M. and Zhu, Z. Q. (2014). Sensorless Control Strategy by Square-Waveform High-Frequency Pulsating Signal Injection Into Stationary Reference Frame. *Emerging and Selected Topics in Power Electronics, IEEE Journal of*, **2**(2), 171–180.

Maciejowski, J. M. (2002). *Predictive Control With Constraints*. Prentice-Hall, Englewood Cliffs, NJ.

Mariethoz, S., Domahidi, A., and Morari, M. (2012). High-Bandwidth Explicit Model Predictive Control of Electrical Drives. **48**(6), 1980–1992.

Morimoto, S., Tong, Y., Takeda, Y., and Hirasa, T. (1994). Loss minimization control of permanent magnet synchronous motor drives. *IEEE Transactions on Industrial Electronics*, **41**(5), 511–517.

Morimoto, S., Sanada, M., and Takeda, Y. (2006). Mechanical sensorless drives of ipmsm with online parameter identification. *IEEE Transactions on Industry Applications*, **42**(5), 1241–1248.

Muzikova, V., Glasberger, T., Smidl, V., and Peroutka, Z. (2015). Finite control set mpc with high frequency injections for sensorless position and speed estimation of a pmsm. In *2015 IEEE International Symposium on Predictive Control of Electrical Drives and Power Electronics (PRECEDE)*, pages 9–14.

Nalakath, S., Preindl, M., Bilgin, B., Cheng, B., and Emadi, A. (2015). Modeling and analysis of ac resistance of a permanent magnet machine for online estimation purposes. In *2015 IEEE Energy Conversion Congress and Exposition (ECCE)*, pages 314–319.

Nalakath, S., Preindl, M., Babak, N. M., and Emadi, A. (2016). Low speed position estimation scheme for model predictive control with finite control set. In *IECON 2016 - 42nd Annual Conference of the IEEE Industrial Electronics Society*, pages 2839–2844.

Nalakath, S., Sun, Y., Preindl, M., and Emadi, A. (2017). Optimization-based position sensorless finite control set model predictive control for ipmsms. *IEEE Transactions on Power Electronics*, **PP**(99), 1–1.

Nordvall, A. (2011). *Multilevel inverter topology survey*. Master's thesis. 78.

Ohnishi, K., Matsui, N., and Hori, Y. (1994). Estimation, identification, and sensorless control in motion control system. *Proceedings of the IEEE*, **82**(8), 1253–1265.

Pan, C. T. and Sue, S. M. (2005). A linear maximum torque per ampere control for IPMSM drives over full-speed range. *IEEE Transactions on Energy Conversion*, **20**(2), 359–366.

Paul C. Krause, Oleg Wasynczuk, S. D. S. (2002). *Analysis of Electric Machinery and Drive Systems*. John Wiley S ons, New York.

Pelckmans, K. (2010). Lecture notes in system identification,.

Preindl, M. and Bolognani, S. (2013a). Comparison of direct and PWM model predictive control for power electronic and drive systems. *2013 Twenty-Eighth Annual IEEE Applied Power Electronics Conference and Exposition (APEC)*, pages 2526–2533.

Preindl, M. and Bolognani, S. (2013b). Model Predictive Direct Speed Control with Finite Control Set of PMSM Drive Systems. *IEEE Transactions on Power Electronics*, **28**(2), 1007–1015.

Preindl, M. and Bolognani, S. (2013c). Model predictive direct torque control with finite control set for PMSM drive systems, Part 1: Maximum torque per ampere operation. *IEEE Transactions on Industrial Informatics*, **9**(4), 1912–1921.

Preindl, M. and Schaltz, E. (2011). Sensorless model predictive direct current control using novel second-order pll observer for pmsm drive systems. *IEEE Transactions on Industrial Electronics*, **58**(9), 4087–4095.

Preindl, M., Bolognani, S., and Danielson, C. (2013). Model Predictive Torque Control with PWM using fast gradient method. *2013 Twenty-Eighth Annual IEEE Applied Power Electronics Conference and Exposition (APEC)*, pages 2590–2597.

Qin, S. and Badgwell, T. A. (2003a). A survey of industrial model predictive control technology. *Control Engineering Practice*, **11**(7), 733–764.

Qin, S. J. and Badgwell, T. A. (2003b). An overview of industrial model predictive control technology. *Control Engineering Practice*, **11**(7), 733–764.

Rafaq, M. S., Mwasilu, F., Kim, J., Choi, H. H., and Jung, J. W. (2017). Online parameter identification for model-based sensorless control of interior permanent magnet synchronous machine. *IEEE Transactions on Power Electronics*, **32**(6), 4631–4643.

Rovere, L., Formentini, A., Gaeta, A., Zanchetta, P., and Marchesoni, M. (2016). Sensorless finite-control set model predictive control for ipmsm drives. *IEEE Transactions on Industrial Electronics*, **63**(9), 5921–5931.

Rusnak, I., Guez, A., and Bar-Kana, I. (1993). Simultaneous state observability and parameters identifiability of discrete stochastic linear systems. In *1993 American Control Conference*, pages 1231–1235.

Saeidi, S. and Kennel, R. (2013). Continuous set nonlinear model predictive control

for an induction motor. *2013 15th European Conference on Power Electronics and Applications (EPE)*, pages 1–10.

Salt, D. E., Drury, D., Holliday, D., Griffo, A., Sangha, P., and Dinu, A. (2011). Compensation of inverter nonlinear distortion effects for signal-injection-based sensorless control. *IEEE Transactions on Industry Applications*, **47**(5), 2084–2092.

Shefali, K. T. (2011). Line search methods.

Shinohara, A., Inoue, Y., Morimoto, S., and Sanada, M. (2016). Maximum torque per ampere control in stator flux linkage synchronous frame for dtc-based pmsm drives without using q-axis inductance. In *2016 IEEE Energy Conversion Congress and Exposition (ECCE)*, pages 1–7.

Soong, W. L., Han, S., and Jahns, T. M. (2007). Design of interior pm machines for field-weakening applications. In *2007 International Conference on Electrical Machines and Systems (ICEMS)*, pages 654–664.

Srinivasan, J., Selvaraj, K., Chitrarasu, J., and Resmi, R. (2016). Design and analysis of squirrel cage induction motor in short pitch and full pitch winding configurations using fea. *2016 International Conference on Emerging Technological Trends (ICETT)*, pages 1–10.

Sun, T., Wang, J., Koc, M., and Chen, X. (2016). Self-learning mtpa control of interior permanent-magnet synchronous machine drives based on virtual signal injection. *IEEE Transactions on Industry Applications*, **52**(4), 3062–3070.

Sun, Y., Preindl, M., Sirouspour, S., and Emadi, A. (2017). Unified wide-speed sensorless scheme using nonlinear optimization for ipmsm drives. *IEEE Transactions on Power Electronics*, **32**(8), 6308–6322.

Underwood, S. J., H. I. (2010). Online parameter estimation and adaptive control of permanent-magnet synchronous machines. *IEEE Transactions on Industrial Electronics*, **57**(7), 2435–2443.

Vaclavek, P., Blaha, P., and Herman, I. (2013). AC Drive Observability Analysis. *Industrial Electronics, IEEE Transactions on*, **60**(8), 3047–3059.

Vas, P., Hallenius, K. E., and Brown, J. E. (1986). Cross-saturation in smooth-air-gap electrical machines. *IEEE Transactions on Energy Conversion*, **EC-1**(1), 103–112.

Wang, F., Mei, X., Rodriguez, J., and Kennel, R. (2017). Model Predictive Control for Electrical Drive Systems-An Overview. *Ces Transactions on Electrical Machines and Systems*, **1**(3), 219–230.

Wang, Y. and Boyd, S. (2010). Fast Model Predictive Control Using Online Optimization. *Control Systems Technology, IEEE Transactions on*, **18**(2), 267–278.

Xu, W., L. R. D. (2014). High-frequency injection-based stator flux linkage and torque estimation for db-dtfc implementation on ipmsms considering cross-saturation effects. *IEEE Transactions on Industry Applications*, **50**(6), 3805–3815.

Xu, J., W. F. X. F. X. J. F. J. (2004). A new control method for permanent magnet synchronous machines with observer. *Power Electronics Specialists Conference, PESC*, pages 1404–1408.

Yang, Y., Bilgin, B., Kasprzak, M., Nalakath, S., Sadek, H., Preindl, M., Cotton, J., Schofield, N., and Emadi, A. (2017). Thermal management of electric machines. *IET Electrical Systems in Transportation*, **7**(2), 104–116.

Zaltni D.a Abdelkrim, M. G. M. B. J., Zaltni, D., Abdelkrim, M. N., Ghanes, M., and Barbot, J. P. (2009). Observability analysis of PMSM. *2009 3rd International Conference on Signals, Circuits and Systems (SCS)*, pages 1–6.

Zhu, Z. Q., Li, Y., Howe, D., Bingham, C. M., and Stone, D. (2007). Influence of machine topology and cross-coupling magnetic saturation on rotor position estimation accuracy in extended back-emf based sensorless pm brushless ac drives. pages 2378–2385.